INVESTIGATION OF AERODYNAMICS OF BIOINSPIRED FLAPPING WINGS

G.G.L. De Silva

198121T

Master of Philosophy

Department of Mechanical Engineering
Faculty of Engineering

University of Moratuwa
Sri Lanka

April 2025

INVESTIGATION OF AERODYNAMICS OF BIOINSPIRED FLAPPING WINGS

G.G.L. De Silva

198121T

Dissertation submitted in partial fulfillment of the requirements for the degree
Master of Philosophy

Department of Mechanical Engineering
Faculty of Engineering

University of Moratuwa
Sri Lanka

April 2025

DECLARATION

I declare that this is my own work and this Dissertation does not incorporate without acknowledgement any material previously submitted for a Degree or Diploma in any other University or Institute of higher learning and to the best of my knowledge and belief it does not contain any material previously published or written by another person except where the acknowledgement is made in the text. I retain the right to use this content in whole or part in future works (such as articles or books).

Signature: Date: 2025/04/07

The supervisors should certify the Dissertation with the following declaration.

The above candidate has carried out research for the Master of Philosophy Dissertation under our supervision. We confirm that the declaration made above by the student is true and correct.

Name of Supervisor: Dr. K.K.N.M.P. Samaraweera

Signature of the Supervisor: Date: 07/04/2025

Name of Supervisor: Prof. N.D. Jayaweera

Signature of the Supervisor: Date: 07/04/2025

Name of Supervisor: Dr. A.G.T. Sugathapala

Signature of the Supervisor: Date: 07/04/2025

DEDICATION

To free education,
To fellow Sri Lankans whose generosity facilitates it,
And,
To the heroes whose sacrifices keep it alive.

ACKNOWLEDGEMENT

I would like to express my deepest gratitude to my supervisors, Dr. Nalaka Samaraweera, Prof. Nirosh Jayaweera, and Dr. Thusitha Sugathapala, for providing their support, encouragement, and patience throughout this research. They understood my capabilities and provided the guidance and advice I needed, which ultimately led to the success of this research. I am very grateful for dedicating their valuable time to me.

Then I would like to express my sincere gratitude to my loving wife Geemanthi and my family and friends for their continued belief in me and their support. I would also like to thank Mr. Lihini Thennakoon, Mr. Rawisha Serasinghe, and Mr. Dhanushka Pieris for their constant assistance and encouragement as fellow postgraduate students throughout the research.

All the academic and non-academic staff in laboratories and workshops in the Department of Mechanical Engineering, University of Moratuwa deserve my gratitude for providing their service whenever required without any hesitation. I extend my sincere gratitude to Dr. Dulini Mudunkotuwa and the dedicated staff members of the Department of Mechanical Engineering, University of Sri Jayawardhanapure, for their invaluable assistance in conducting the experimental investigations for this research.

This research was funded by the Senate Research Council of the University of Moratuwa, Sri Lanka Grant No SRC/LT/2020/16 and I would like to express my gratitude towards them for providing all the required funding which makes this research a reality.

The wind tunnel facilities at the Department of Mechanical Engineering, University of Sri Jayawardhanapure which were used in the experimental investigation, are provided as part of the Science and Technology Human Resource Development Project, Ministry of Education, Sri Lanka, funded by the Asian Development Band under the Grant No: CRG/R3/SJ18.

ABSTRACT

In the quest to develop bioinspired micro air vehicles capable of efficient operation in dynamic environments, transient measurements of aerodynamic forces on pitching and plunging wings are essential. While previous investigations have measured these forces, there remain gaps in knowledge that impede further development of bioinspired micro air vehicles. Overarching characteristics of lift and thrust performances of pitching and plunging wings in varying kinematic scenarios have not been the subject of extensive research. The majority of previous research has concentrated on assessing the performance of custom-developed wing platforms tailored for specific flapping wing micro air vehicle applications. In cases where a standard airfoil shape is employed, investigations have been limited to a few wing flapping frequencies or free-stream velocities. In this research, unsteady aerodynamic forces of pitching and plunging wings in a range of frequencies and free stream velocities inspired by birds are investigated both experimentally and computationally.

The experimental investigation encompasses fourteen different kinematic scenarios spanning Reynolds numbers from 20,000 to 100,000 and Strouhal numbers from 0.02 to 0.1. Complementing this, the computational investigation provides additional insights through time series variations in aerodynamic forces, velocity, and pressure contour for twenty-five kinematic scenarios, including those examined experimentally. The range of Reynolds and Strouhal numbers is derived from measurements taken from birds in forward flapping flight. An experimental apparatus, purposefully designed and developed for this investigation, is used in subjecting a wing with a uniform cross-section of the NACA 0012 airfoil to controlled pitch and plunge motions while simultaneously measuring the aerodynamic forces acting on the wing. The measurements taken using a force sensor are post-processed to compute the time-history variation of lift and thrust coefficients in varying kinematic scenarios. Characteristics of resultant lift and thrust coefficient variations and average values are discussed with existing findings in flapping wing aerodynamics. Gradual decrements of extremum values in transient lift and thrust coefficient variations are observed with increasing Reynolds number and receding Strouhal number values. The mean values of lift and thrust coefficients increase by an average of 35% and 83% respectively with increasing Strouhal number in Reynolds number values of 20 000 and 40 000. But the mean lift coefficient values decrease by an average of 46% with rising Reynolds number while Strouhal number is 0.02 and 0.04. Results indicate that flapping wing micro air vehicles perform efficiently in Reynolds numbers below 40 000 with stability in forward accelerations and altitude changes increasing with rising Reynolds number values.

The computational investigation was done using Ansys fluent computational fluid dynamics simulation software. After establishing an optimized simulation methodology, a series of simulations were carried out. Aerodynamic force values are exported and postprocessed to develop velocity and pressure contour plots as images and animations to further supplement the experimental and computational results. The characteristic trends observed in the experimental results were confirmed by the computational results. The mean lift coefficient values exhibit an average increase of 31% with rising Strouhal number values, while they decrease by an average of 54% with increasing Reynolds number values. On the other hand, the mean thrust coefficient values demonstrate an average increase of 32% with increasing St values and a rise of 11% on average with increasing Reynolds number values. The comparison between experimental and computational results reveals a favorable agreement in the time-history variations of lift and thrust coefficients. The percentile deviation between the mean lift and thrust coefficients of the experimental and computational results is calculated at 12.15%, indicating a reasonably close correlation.

Keywords: Experimental Aerodynamics, Computational Fluid Dynamics, Bioinspired Wings, Micro Air Vehicles, Flapping Wings

TABLE OF CONTENTS

LIST OF FIGURES

LIST OF APPENDICES

NOMENCLATURE

δ	Measurement uncertainty
$\dot{q}$	Energy generation per unit volume
μ	Dynamic viscosity
μ_k	Turbulent eddy viscosity
ν	Kinematic viscosity
$\boldsymbol{V}$	Velocity vector field
ρ	Air density
σ	Percentile uncertainty
σ_k	Turbulent Prandtl number
τ	Shear stress
c	Chord length
C_D	Drag coefficient
C_L	Lift coefficient
e	Specific internal energy
f	Body force per unit mass
F_D	Drag force
F_L	Lift force
f_x	External force
$F_{P/C}$	Force measurement perpendicular/ parallel to the wing chord
g	Gravitational acceleration
I	Identity matrix
K	Reduced frequency
k_T	Thermal conductivity

l	Span length
m, n	Calibration coefficients
P	Fluid pressure
Re	Reynolds number
St	Strouhal number
T	Temperature
T_n	Normalized periodic time
U, V, W	Fluid velocity
$V_{P/C}$	Voltage measurement perpendicular/ parallel to the wing chord

LIST OF ABBREVIATIONS

UAV	Unmanned Aerial Vehicle
BAV	Bioinspired Aerial Vehicle
MAV	Micro Aerial Vehicle
FWBAV	Flapping Wing Bioinspired Aerial Vehicle
FWBMAV	Flapping Wing Bioinspired Micro Aerial Vehicle
CFD	Computational Fluid Dynamics
PIV	Particle Image Velocimetry
UPM	Unsteady Panel Method
FVM	Finite Volume Method
LES	Large Eddy Simulation
NACA	National Advisory Committee for Aeronautics
NASA	National Aeronautics and Space Administration
CNC	Computer Numerical Control
AIAA	American Institute of Aeronautics and Astronautics
AGARD	Advisory Group for Aerospace Research and Development
NATO	North Atlantic Treaty Organization
AoA	Angle of attack
LEV	Leading Edge Vortex
TEV	Trailing Edge Vortex

LIST OF PUBLICATIONS

1. Lakshitha De Silva et al. “A Computational Study of the Aerodynamics of Plunging and Pitching Motions of Airfoils”. In: 2022 Moratuwa Engineering Research Conference (MERCon). IEEE, July 2022. DOI: 10.1109/MERCon55799.2022.9906181

2. Lakshitha De Silva et al. “Should We Care about how Birds Fly?” In: Bolgoda Plains 3.1 (Aug. 2023), pp. 15–18. ISSN: 2815-0082.
DOI: 10.31705/BPRM.v3(1).2023.3

3. Lakshitha De Silva et al. "An Experimental and Computational Investigation of Aerodynamics of Bioinspired Pitching and Plunging Wings". In: Advances in Aerodynamics. (Under Review)

4. Lakshitha De Silva et al. "A Framework for Wind Tunnel Testing of Scale Models in Low Subsonic Conditions". In: Australian Journal of Mechanical Engineering. (Under Review)

5. Lakshitha De Silva et al. "Aerodynamics of Flapping Wing Bioinspired Aerial Vehicles: From Theory to Application". For: International Journal of Micro Air Vehicles. (Under development)

CHAPTER 1

INTRODUCTION

The ability of animals to generate lift and propulsion by flapping their wings has been a subject of fascination and scientific inquiry for centuries. Researchers in different fields have provided insight into the mechanisms of flight of insects, mammals, and birds. Bioinspired aerodynamics has been important in engineering research for the development of flapping wing air vehicles, morphing wing aircraft [1], and bioinspired wind turbine technologies [2, 3]. Advanced materials are used in morphing wing designs to change the shape of the wings inspired by the morphing wings of large birds. [4]. This could eliminate the rudder, aileron, and flap mechanisms of aircraft in the future. Reduction in the number of mechanical components and weight would improve the reliability of the aircraft and reduce the cost of air travel. Bio-inspired wind energy harvesting is being developed to increase the efficiency of energy extraction from renewable sources like wind, waves, and tides [5]. Flapping wing air vehicles have been the first type of apparatus developed by humans in their attempt to conquer the skies. However, after numerous failures to mimic the flight of birds and with the realization of separating the lift and thrust generation mechanisms for air vehicles, the development has solely been focused on fixed and rotary wing air vehicles. But, encouraged by the recent advancements in electronics, material, and mechanical engineering fields and the pursuit of improved energy efficiency in air vehicles, research interest in flapping wing unmanned aerial vehicles has increased significantly in recent years [6]. Harnessing unique flight characteristics of birds like maneuverability, endurance, and efficiency is the primary objective of such developments [2, 7]. Rotary and fixed-wing UAVs have yet to demonstrate the efficiency and adaptability observed in birds [8, 9]. In the quest for the advancement of more efficient and maneuverable Unmanned Air Vehicle (UAV) development, the logical trajectory is to replicate birds to the extent that technology allows. However, due to current technological limitations, achieving a perfect replication of bird wing motion remains elusive for Flapping Wing Bioinspired Aerial Vehicles (FWBAVs). Instead, simplified wing motions that closely mimic certain aspects of bird wing motion are commonly used [10–16].

This research focuses on understanding the aerodynamic mechanisms of pitching and plunging wings in varying kinematic scenarios. The Reynolds number (Re) and Strouhal number (St) values, which govern the wing's mechanics, draw inspiration from the flight dynamics observed in forward-flying birds. Increased interest in Flapping Wing Bioinspired Aerial Vehicle (FWBAV) developments has highlighted gaps in the existing knowledge. Although experimentally obtained force characteristics of pitching and plunging wings have been published by previous studies, the majority of them focus on custom wing designs tailored for specific FWBAVs applications.

[17–21]. Moreover, existing investigations frequently prioritize particular combinations of Re and St , relating to both flight speed and wing motion mechanics [22–25]. Therefore, they are limited in understanding the overarching characteristics of flapping wings in the large range of motion showcased by birds of flight. This investigation aims to provide experimental measurements and computational results that would assist in identifying and understanding such overarching characteristics of aerodynamic force generation in pitching and plunging wings with varying Re and St values.

The experimental investigation incorporates a custom developed apparatus capable of both wing motion control and aerodynamic force measurement simultaneously. The apparatus is highly customizable, allowing for independent adjustment of the amplitude and frequency of both pitch and plunge motions. In addition, it offers flexibility in varying the geometry of the wings as well as the positions of pitch and plunge axes. The upper and lower limits of the motion parameters are set by mechanical and spatial constraints. The experimental apparatus is used to investigate fourteen kinematic scenarios within the range of Re values between 20 000 and 100 000 and St values between 0.02 and 0.1. Aerodynamic forces on the moving wing are measured using a force sensor arrangement through which the wing is connected to the motion control system. The experiments were carried out using an open-type small-scale wind tunnel facility. After the calibration and validation processes, the measurements were collected in fourteen different test scenarios. The measurements were then processed to calculate the time history variations in the lift and thrust coefficients in a wing motion cycle.

The computational investigation is carried out using the ANSYS Fluent Computational Fluid Dynamic (CFD) software. The objective is to produce high-resolution simulations of flapping wings under varying kinematic conditions to complement the experimental investigation. The CFD simulations cover twenty five kinematic scenarios including the fourteen investigated experimentally. The mesh quality and the time-step values used in the simulations were optimized using an extensive mesh and time-step convergence analysis. The CFD simulation methodology was subjected to validation through quantitative and qualitative comparisons with published experimental results. The simulation export files are post-processed to compute averaged time history variations of lift and thrust coefficients for a wing motion cycle. Furthermore, velocity and pressure contour plots were generated in the form of images and animations to gain insight into the underlying fluid mechanisms and their relation to lift and thrust performance.

This document provides comprehensive discussions on experimental and computational investigation methodologies, with separate analyses of the obtained results, as well as comparative discussions. The research premise is established through a comprehensive literature review, the summary of which is included in this document. Attached as Appendices are frameworks for experimental investigations using small to medium wind tunnels and guidelines for CFD investigations of model aerodynamics with motion using Ansys Fluent. These resources aim to transfer the unique collection of data and experiences to future researchers in the field. In addition, a user manual for the experimental apparatus developed during the research is included in the appendices to facilitate ongoing usage of the apparatus in future undergraduate and graduate research.

1.1 Objectives of the research

- Development of experimental set-up capable of capturing both quantitative and qualitative measurements of a flapping wing in the wind tunnel.
- Development of CFD framework to model flapping wing aerodynamics in two-dimensional domain.
- Identification of optimal aerodynamic and kinematic parameters for flapping wing propulsion.

1.2 Thesis overview

This thesis consists of four main sections. As the initiation of the thesis, a summarized literature review is included. Previous experimental and computational investigations of flapping wing aerodynamics and previous Flapping Wing Bioinspired Aerial Vehicles (FWBAV) are discussed. The research approaches to both experimental and computational investigations are explained separately in detail. Finally, the results from both sections are discussed separately and in comparison with one another to understand their characteristics. Furthermore, knowledge collected during the research on experimental and computational methodologies and challenges is compiled into two sections attached as Appendices.

CHAPTER 2

LITERATURE SURVEY

The literature survey was divided into three main sections, as illustrated in the diagram below, to comprehensively cover the primary areas of interest.

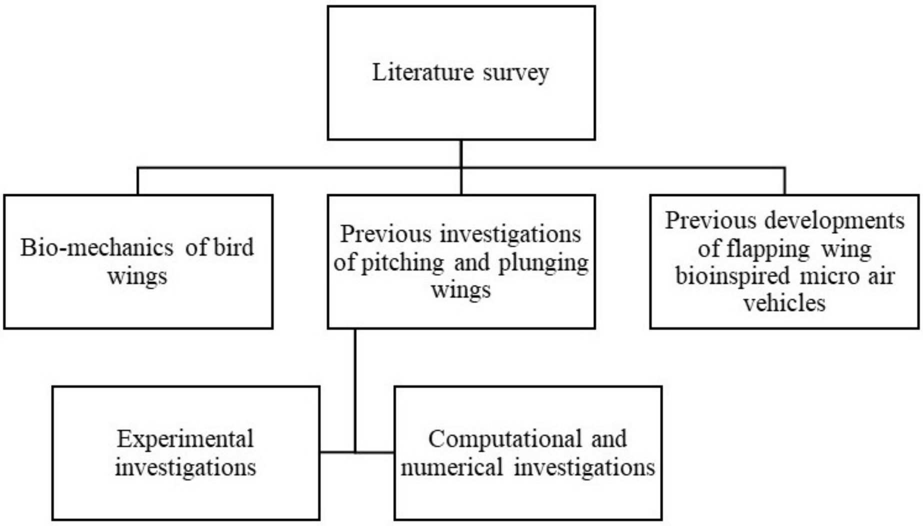

Fig. 2.1: Hierarchy of the literature survey

2.1 Bio-mechanics of bird wings

2.1.1 Historical remarks of flapping flight

According to the studies of paleontologists, the existence of winged animals can be traced back to the Carboniferous period (3.6×10^8 years ago). They describe the invasion of the land by both plants and animals have taken place in the Silurian period (4×10^8 years ago), after which in the Devonian period arthropod's evolution on land led to the six-legged form characteristic of insects before any development of wings took place. Extensive fossil evidence has been found to support the hypothesis that there was a remarkable diversity in winged insects by the middle of Carboniferous period [26]. In the meantime, the reptiles having evolved from Amphibia, later flourished remarkably in the Jurassic and Cretaceous periods (2×10^8 to 1×10^8years ago) and they included an extensive group of flying animals: the pterosaurs. They are the earliest vertebrates known to have evolved powered flight. Their wings were formed by a membrane of skin, muscles, and other tissues stretching from ankles to a dramatically lengthened four fingers.

Based on fossil records, paleontologists and biologists have determined that birds evolved from theropod dinosaurs, specifically Paraves, a diverse group originating in the late Jurassic period. Other discoveries include different stages of evolution of the wings for powered flight such as Theropod dinosaurs with extended forearms and quill-like feathers arranged as wings [27]. Biologists believe that feathers appeared long before wings for insulation and display purposes. However, the major evolution from flying dinosaurs to birds is miniaturization. But common bird characteristics such as small, lightweight, feathered, and winged body were pieced together over millions of years of evolution.

In the present day, the diversity of birds, mammals, and insects that perform flapping wing flight is extremely complex. Scientists claim there are 9 000 – 10 000 different species of birds and a staggering 5.5 million insect species. According to the definition of vertebrate birds, bats can be classified as vertebrates with flight capabilities. Although there are few species of squirrels that are vertebrates capable of hovering or gliding flight since the focus of the research is on flapping flight, they are not included in further discussion. Due to the huge biodiversity within the animals that perform flapping wing flight, studying their characteristics by following the species and the evolution tree is difficult and ineffective in gaining knowledge of their aerodynamic characteristics. Therefore, the said animals are categorized according to their wing and flapping motion characteristics so that more attention can be focused on the areas of studies relevant to the research [28].

2.1.2 Classification of natural wings

For the convenience of studying, all the animals with flapping wing flight capabilities are put into groups according to the behavior and characteristics of their flapping wings in normal forward motion flight [29]. They are,

- Flexible wings.
- Membranous muscular wings
- Minimal morphing feathered wings
- Morphing feathered wings

The following discussion review each wing type, motion of their muscles, feathers, and joints in flapping flight, information gathered by the study of wing motion and identified aerodynamic phenomena caused by those said characteristics.

2.1.2.1 Flexible wings

In nature, the wings of nearly all insects belong to this category, characterized by their extreme lightweight and thinness. The majority of these wings exhibit zero camber and behave akin to flat plates in their flapping motion through the air. Their movement is primarily governed by muscles located at the joints, providing both support and control simultaneously. Various insect species employ different muscles for this function, yet the underlying phenomenon remains consistent.

Insects with flexible wings typically possess two sets of wings on either side of their body. The synchronized motion of these wings is thought to enhance the aerodynamic efficiency of the insect. Research has shown that the intricate motion of these wings enhances the likelihood of wake capturing, an aerodynamic phenomenon in which the wake generated by one wing influences the following wing to operate more efficiently by manipulating the flow field around it [29]. The surfaces of these flexible wings have evolved to optimize aerodynamic efficiency during the flight maneuvers performed by insects [30].

2.1.2.2 Membranous muscular wings

Bats are known for their use of flapping membranous wings for flight, a unique trait among mammals. Their flight abilities are considered crucial to their evolutionary success, playing a significant role in their adaptation and ecological niche. Bat wings are a membrane connected with their legs which makes it highly adjustable by the muscles in the leg. Experimental and computation models have generated results as their lift generated is highly concentrated on the downstroke of wings. At upstroke, bat wings are folded and moved very close to the body [29].

2.1.2.3 Minimal morphing feathered wings

Feathered wings are classified into two categories based on their flight behavior, which is significantly influenced by wing morphing. The first category, minimal morphing wings, includes birds like the Hummingbird, known for their unique flight characteristics. Close analysis of hummingbird wings using ultra slow-motion cameras reveals that during forward and hovering flight, their wings behave almost rigidly. The joints connecting the wings to the body exhibit complex combinations of rotary and linear motions to effectively change the angle of attack and flapping frequency.

2.1.2.4 Morphing feathered wings

Majority of birds possess feathered wings that can morph into various configurations to meet their aerodynamic needs, enhancing their efficiency and maneuverability. While morphing techniques enable birds to achieve speed and agility in flight, they present significant challenges for modeling and analysis due to their complexity. The dynamic variations in wing movement result in unique upstroke and downstroke patterns tailored to specific flight conditions. This is made possible by the combination of muscles and skeleton within their wings [31]. The biomechanics of a morphing bird wing bears a resemblance to a human hand, although with different bone proportions. The hand section of the wing serves as the primary dynamic control mechanism for the bird, constituting approximately 80% of the wing length in smaller birds. In larger birds, which primarily employ their wings for soaring, gliding, and slow flapping, the hand section is proportionally smaller. Instead, the wing is governed by the elongated arm bones, which typically span from 40% to 60% of the total wingspan. [32].

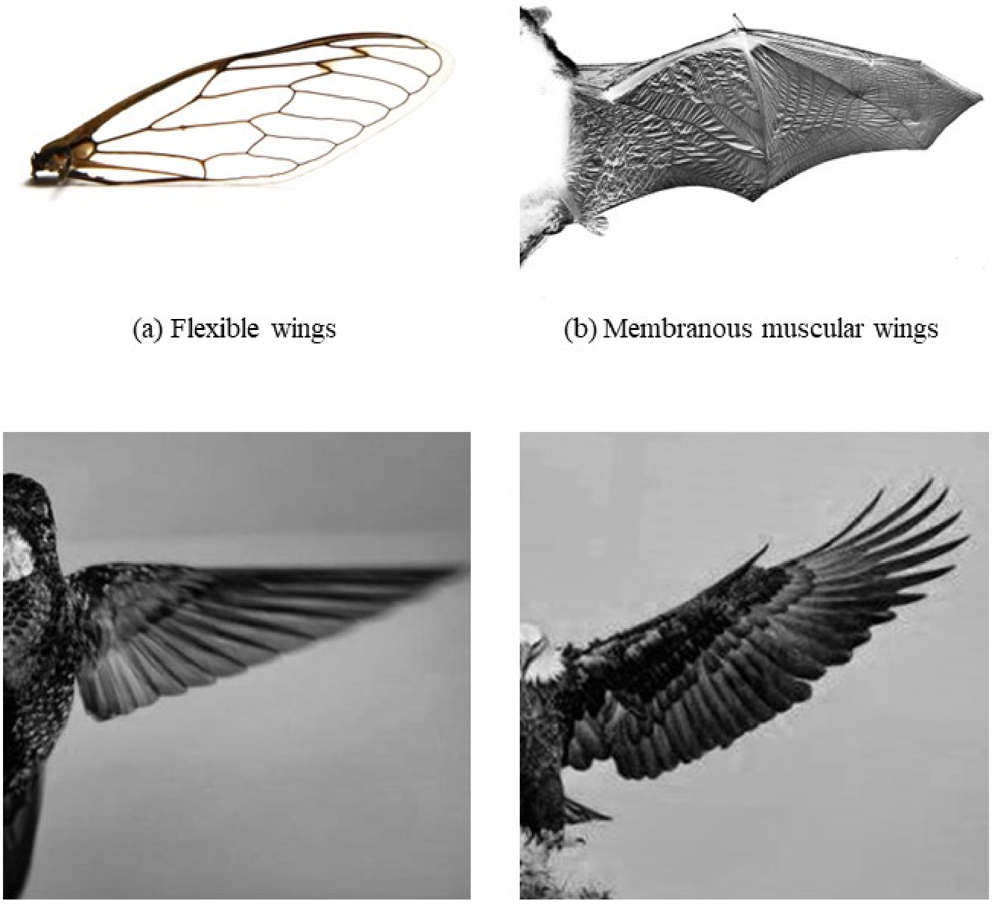

(a) Flexible wings

(b) Membranous muscular wings

(c) Minimal morphing feathered wings

(d) Morphing feathered wings

Fig. 2.2: Examples for the different wing types found in nature

2.1.3 Mechanics of flapping wings of birds

The biomechanics of bird and insect wings are complex and consist of multiple movements of muscles, skeletal structures, membranes, and feathers. All these components work in unison to enable the animal to perform complicated wing motions. The wing motion mechanics differ from one species of bird to another. For the ease of studying, they are usually simplified using non-dimenional parameters like Re, St, and reduced frequency (K).

2.1.3.1 Reynolds number (Re)

Reynolds number is the ratio of inertial forces to viscous forces within a fluid which is subjected to relative internal movement due to different fluid velocities. In a bird flight scenario, the relevant characteristic length is the chord length of the bird wing. Recan range up to six orders of magnitude among flying animals, from values close to 1 for smallest insects to 1 000 000 for a diving falcon. Beyond Re of 10 000, the regime in which the most vertebrates fly, the boundary layer can become transitional or turbulent, which governs aerodynamic performance in such a way that is not yet completely understood for birds

$$Re = \frac{V \rho c_{avg}}{\mu} \tag{2.1}$$

2.1.3.2 Strouhal number (St)

St is a dimensionless number usually used to describe oscillating flow mechanisms. St is commonly used in biological literature to nondimentionally quantify wing flapping frequency. The standard equation for St is given below, f is vortex shedding frequency and L is characteristic length with V being the flow velocity.

$$St = \frac{fL}{V} \tag{2.2}$$

Bruderer et al [33][34] have gathered a wealth of data by observing and measuring bird flights. This information includes flight velocity range, wing span, wing area, and wing flapping frequency. Table B.1 includes Re and St values of 60 species of birds calculated with these measurements.

TABLE 2.1: Flight characteristic data and calculated Reynolds number and Strouhal number values of bird species

Scientific Name	V_{avg} (ms^{-1})	C_{avg} (m)	Re	St
Carduelis spinus	9	0.0330	19549.77	0.045
Regulus regulus	7	0.0317	14607.20	0.097
Phylloscopus trochilus	9.5	0.0363	22664.36	0.066
Sylvia atricapilla	8.5	0.0414	23144.60	0.077
Sylvia borin	9	0.0417	24688.79	0.072
Sylvia communis	14	0.0351	32319.66	0.039
Sylvia curruca	12	0.0395	31146.67	0.060
Sylvia hortensis	7	0.0467	21487.41	0.100
Hippolais polyglotta	4	0.0324	8537.12	0.119
Hippolais icterina	9.5	0.0363	22697.76	0.062
Acrocephalus arundinaceus	9	0.0442	26137.36	0.072
Acrocephalus scirpaceus	8.5	0.0326	18244.68	0.063
Acrocephalus palusiris	9	0.0338	20036.92	0.075
Turdus viscivorus	13	0.0859	73486.11	0.044
Turdus philomelos	13	0.0620	53041.67	0.046
Turdus pilaris	14	0.0785	72306.83	0.040
Turdus merula	12	0.0771	60885.22	0.056
Oenanthe oenanthe	11	0.0472	34181.76	0.046
Saxicola rubetra	10.5	0.0422	29161.48	0.057
Phoenicurus phoenicurus	9.5	0.0444	27741.70	0.061
Phoenicurus ochruros	8.5	0.0433	24190.11	0.078
Erithacus rubecula	8	0.0452	23805.29	0.083
Prunella modularis	7.5	0.0460	22693.33	0.111
Motacilla flava	9.5	0.0412	25745.42	0.072
Anthus prafensis	12	0.0460	36275.74	0.056
Anthus trivialis	8	0.0485	25501.54	0.085
Delichon urbica	11.5	0.0389	29432.57	0.028
Hirundo daurica	18	0.0467	55253.33	0.018
Hirundo rustica	12.5	0.0399	32839.51	0.023
Riparia riparia	15	0.0345	34071.94	0.022
Alauda arvensis	19	0.0588	73471.78	0.028
Lullula arborea	10	0.0575	37851.07	0.067
Upupa epops	13	0.0959	82012.93	0.037
Merops apiaster	14.5	0.0587	55995.99	0.025
Apus pallidus	10.5	0.0598	41283.03	0.045
Apus apus	11.5	0.0378	28576.79	0.023
Apus melba	13	0.0533	45605.93	0.023
Capiimuigus ruficollis	10	0.0853	56084.21	0.063
Pterocles coronatus	17	0.0765	85499.47	0.042
Larus canus	14	0.1008	92779.56	0.022
Larus ridibundus	13	0.0901	77041.44	0.022
Tringa ochropus	3	0.0490	9665.99	0.100
Gailinago gailinago	18	0.0596	70519.56	0.022
Phiiomachus pugnax	16	0.0809	85188.43	0.033
Caiidris alpina	9.5	0.0385	24069.79	0.042
Asio flammeus	8	0.1310	68947.95	0.052
Vanellus vanellus	13	0.0970	82981.20	0.037
Giareola nordmanni	12.5	0.0844	69375.00	0.033
Giareola pratincola	15	0.0805	79406.93	0.028
Cursorius cursor	14	0.0754	69407.74	0.027
Falco peiegrinoides	15.5	0.1224	124838.91	0.037
Falco peregrinus	14	0.1296	119311.26	0.045
Falco eleonorae	12	0.0424	33480.89	0.018
Falco subbuteo	12	0.1092	86191.57	0.045
Falco vespertinus	14.5	0.1011	96437.53	0.036
Falco tinnunculus	12	0.0906	71510.46	0.037
Falco naumanni	18	0.0940	111296.00	0.026
Accipiter brevipes	14	0.1056	97219.56	0.036
Circus macrourus	15	0.1445	142538.91	0.031
Pernis apivorus	11	0.1895	137141.61	0.055

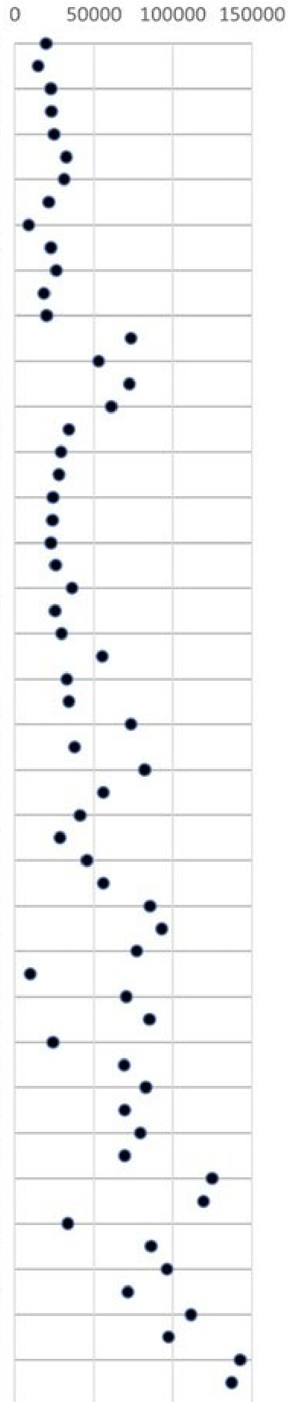

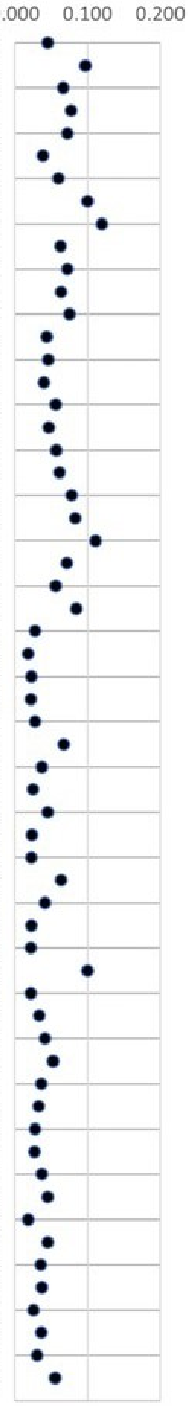

2.2 Previous experimental investigations of flapping wings

A summary of the technical details of the experimental apparatuses used in previous flapping wing investigations is given in Table 2.2. The majority of these experimental set-ups have contributed to more than one academic publication in unsteady aerodynamics of wing motion. In this chronological compilation of previous work, a clear trend of increased interest in bio-inspired wing motion and their aerodynamics can be observed. Most recent research has also investigated the flexibility of wings and its contribution to aerodynamic efficiency. Several investigations have dedicated their focus to fluid dynamic force measurements, while others have prioritized fluid flow visualization.

Additionally, certain studies have integrated simulation data to enhance the analysis of experimental results, although this information is not included in the summarized table. The trend of utilizing numerical methods to filter and improve the quality of experimental measurements is observed in the most recent investigations. The three-stage filtering process of using Butterworth low-pass, moving average, and Chebyshev low-pass filters for unsteady force measurement data has been used in multiple research works. Experimental investigations covering a range of velocities and wing motion parameters, such as Strouhal number or reduced frequency, have been limited. The majority of studies have focused on only a few selected scenarios, typically inspired by specific bird or insect species or intended for FWBAV applications.

The latest research frequently incorporates Particle Image Velocimetry (PIV) techniques, which offer a non-intrusive method of measurement ideally suited for these types of investigations. Wing motion is typically controlled by electric motors connected to gear or lever mechanisms. While not always explicitly mentioned in publications, the majority showcase the flexibility to vary wing motion frequency through actuator control.

TABLE 2.2: Summary of technical details of experimental apparatuses used for previous flapping wing investigations

Dickinson H.L. et al [17], 1999	
Pitch control	Stepper motor driven gearbox assembly
Plunge control	Stepper motor driven gearbox assembly
Heave control	Stepper motor driven gearbox assembly
Types of wings	Drosophila inspired Custom wing
Testing facility	1mx1mx2m free surface tank of mineral oil
Re range	136 (Hovering)
Force measuring	2D force transducer with 2 sets of strain gauges wired in full bridge configuration
Data collection and processing	Not mentioned
Flow visualization method	None

Sunada S. et al [35], 2001	
Pitch control	Servo motor driven belt drive
Plunge control	Servo motor driven linkage mechanism
Heave control	None
Types of wings	Rectangular wing (c=28.3mm)
Testing facility	A water tank
Re range	1000 (Hovering)
Force measuring	Load cell measuring F_x, F_y, M_y
Data collection and processing	Two strain amplifiers with low pass filter(F_c=1Hz)
Flow visualization method	Alumiunm dust sprinkled over the water surface

Jones K.D. et al [36], 2002	
Pitch control	None
Plunge control	None
Heave control	Motor driven gear mechanism
Types of wings	NACA 0014
Testing facility	1.5mx1.5m low speed wind tunnel
Re range	10 000 - 45 000
Force measuring	Laser measurements of displacement of the model suspended by cables
Data collection and processing	Data collection frequency =2-7Hz
Flow visualization method	None

Isaac K.M. et al [18], 2006	
Pitch control	None
Plunge control	Motor driven linkage mechanism
Heave control	Motor driven linkage mechanism
Types of wings	Custom flat plate wing
Testing facility	Not mentioned
Re range	5 000 - 7 000, 10 000
Force measuring	Single point force transducer in full bridge configuration
Data collection and processing	Not mentioned
Flow visualization method	None

Hubei T.Y. et al [19], 2008	
Pitch control	Manual adjustment
Plunge control	None
Heave control	Motor driven gear mechanism
Types of wings	Custom wing modeled after Goose wing
Testing facility	2mx2.2mx4.9m low speed wind tunnel
Re range	28 000 - 141 000
Force measuring	3 component load cell capable of measuring F_x, F_y, M_y
Data collection and processing	Data collection f=300HZ and 600Hz, Butterworth low pass filter
Flow visualization method	PIV with Nd-YAG double-pulse laser and two PCO SensiCam CCD cameras

Baik Y.S. et al [37], 2009	
Pitch control	Motor driven rotary stage
Plunge control	Motor driven linear traverse
Heave control	None
Types of wings	SD 7003 wing, flatplate
Testing facility	Horizontal free surface wind tunnel, low turbulence water channel
Re range	10 000,30 000,60 000
Force measuring	None
Data collection and processing	None
Flow visualization method	Distributed dye injection system, PIV with Nd-YAG laser and synchronized CCD cameras

Aono H. et al [38], 2010	
Pitch control	None
Plunge control	None
Heave control	Motor driven gear mechanism
Types of wings	Flat Zimmerman platform modeled after insect wing (AR=7.65)
Testing facility	Not mentioned
Re range	2 600
Force measuring	A load sensor
Data collection and processing	None
Flow visualization method	PIV with Nd-YAG laser and LaVision imager proX 4M camera.

Mazaheri K. [20], 2011	
Pitch control	None
Plunge control	None
Heave control	Motor-driven gear mechanism
Types of wings	Custom flexible membrane wing
Testing facility	2.8mx2.2m open test section wind tunnel
Re range	Velocity range: $6 - 12ms^{-1}$
Force measuring	One-dimensional load cell
Data collection and processing	Not mentioned
Flow visualization method	None

Granlund K. [22], 2011	
Pitch control	Electronic linear motor
Plunge control	Electronic linear motor
Heave control	None
Types of wings	Flat Zimmerman platform (AR=1), Flat plate (AR=2)
Testing facility	Air vehicle directorate wind tunnel (Turbulence intensity=0.4% at $15ms^{-1}$)
Re range	10 000
Force measuring	ATI Nano-25 IP68 component integral loadcell
Data collection and processing	Three step data filtering process. ATI Netbox low pass filter (f_c=11Hz), 11 point moving average, 6^{th} order Chebyshev low pass filter
Flow visualization method	Dye injection

Vandenheede R.B.R. [23], 2014	
Pitch control	Directly connected motor
Plunge control	Motor driven linear transverse slider
Heave control	None
Types of wings	Zimmerman platform (c=79.1mm) modeled after Hawkmoth
Testing facility	0.610m x 0.610 x 2.44m water channel
Re range	4 800 (Hovering)
Force measuring	ATI Mini 40 force/torque sensor
Data collection and processing	Averaged from six sets of 25 separate cycles, Butterworth low=pass filter
Flow visualization method	PIV with Nd-YAG laser, an external timing system, a high-resolution camera

Cleaver D.J. [24], 2016	
Pitch control	None
Plunge control	3 phase motor driven worm-gear mechanism
Heave control	None
Types of wings	NACA 0012 (c=0.1m, AR=1.5 and 3)
Testing facility	381mm x 508mm x 1530mm close loop water tunnel
Re range	10 000 ±200
Force measuring	Two-component binocular strain gauge force balance
Data collection and processing	Data collection f=1kHz, Averaged from 20 00 data point for 360 cycles
Flow visualization method	Volumetric flow measurements: a 3 component velocimetry system for Defocusing Digital Particle Image Velocimetry (DDPIV)

Chen L. [39], 2018	
Pitch control	Servo motor assembly
Plunge control	Servo motor assembly
Heave control	Servo motor assembly
Types of wings	Flat plate(c=0.06m)
Testing facility	0.8m x 0.8m x 0.8m tank filled with mineral oil
Re range	1 500(hovering)
Force measuring	ATI Nano 17 IP65 6 component load cell
Data collection and processing	4^{th} order Butterworth filter (f_c=5 x perturbation frequency in each trial)
Flow visualization method	None
Bhat S.S. [21], 2019	
Pitch control	Servo motor-driven belt and gear mechanism
Plunge control	Servo motor-driven linkage mechanism
Heave control	None
Types of wings	Custom flat wing
Testing facility	0.5m x 0.5m 0.6m tank filled with mineral oil
Re range	215 (Hovering)
Force measuring	ATI Nano 17 IP65 6 component load cell
Data collection and processing	Data collection f=100Hz, Low pass filter (f_c=5Hz)
Flow visualization method	None
Otomo S. [25], 2020	
Pitch control	Directly connected motor
Plunge control	None
Heave control	None
Types of wings	NACA 0018 (c=150mm)
Testing facility	0.6m x 0.6m x 3m water channel
Re range	32 000
Force measuring	Data collection f=1Hz, 3-step filtering (Butterworth, moving average and Chebyshevb filters)
Data collection and processing	Data collection f=100Hz, Low pass filter (f_c=5Hz)
Flow visualization method	Time Resolved Particle Image Velocimetry (TR-PIV)
Moriche M. [40], 2021	
Pitch control	Motor-driven gear
Plunge control	Motor-driven gear and lever
Heave control	Motor-driven gear and lever
Types of wings	NACA 0012, flat plate
Testing facility	Not mentioned
Re range	20 000
Force measuring	ATI Mini 40 6 component force balance
Data collection and processing	Data collection f=500Hz, averaged over 5 rounds of each case, Zero phase Butterworth filter(f_c=5Hz)
Flow visualization method	None

2.3 Previous computational investigations of flapping wings

Numerical investigations have been conducted to explore the fluid dynamic characteristics of flapping wings with varying kinematics across different flow conditions, employing a variety of methods [35] [41]. Numerical simulations of moving airfoils have evolved significantly over the years. Garrick used the assumptions of potential flow and small-amplitude oscillation to determine the propulsive efficiency of pitching and plunging flat-plate airfoil [42]. Investigation using the Unsteady Panel Method (UPM) by Basu and Hancock illuminated limitations in previous work like not considering the effect of airfoil camber and wake development [43, 44]. Circulation is recalculated every time step, and vorticity is shed into the wake. This allows for the development of self-inducing velocities in the wake. Later development and use of Finite Volume Method (FVM) and Large Eddy Simulation (LES) method to numerically solve Navier-Stokes equations further improve the computational accuracy of the investigations by overcoming limitations like the use of Kutta condition at the trailing edge which does not accommodate flow separation over the airfoil surface. A summary of technical details of a collection of such investigations are presented in table 2.3. The trend of using propitiatory Navier-Stokes solvers has changed with increased accuracy and popularity of commercial CFD simulation tools. However, attempts to increase the computational efficiency especially in Navier Stokes solvers using FVM and LES have generated new interest in optimizing other numerical approaches.

TABLE 2.3: Summary of technical details of previous computational investigations of flapping wing aerodynamics

Tuncer I. et al, [45, 46], 1998, 2000	
CFD method	2D compressible Navier–Stokes solver
Software tool	Custom developed Navier–Stokes code
Wing geometry	NACA 0012
Wing motion kinematics	Pitching and plunging motion at various reduced frequency, amplitude, phase shifts
Re range	1 100 - 12 000
Results	Time history of drag/ Velocity, vorticity and particle tracer rendering

Ramamurti R. [47], 2001	
CFD method	3D A finite element flow solver based on unstructured grids
Software tool	Custome developed Arbitrary Lagrangian Eulerian (ALE) Incompressible Navier-Stokes solver
Wing geometry	Custom shaped flat wing (Drosophila inspired)
Wing motion kinematics	Heaving and pitching motion at various frequencies and phase shifts
Re range	136 (match the Reynolds number of a typical Drosophila)
Results	Time history of thrust and lift / Velocity vector plot

Wu J.H. et al [41], 2004	
CFD method	3D Navier–Stokes solver
Software tool	Custom developed Navier–Stokes solver code
Wing geometry	Custom shaped flat plate
Wing motion kinematics	Heaving and pitching motion at various frequencies and phase shifts
Re range	Various values between 140-1800
Results	Time history of drag and lift / Velocity contour plot

Sengupta T.K. et al [48], 2005	
CFD method	2D Navier–Stokes Solver with vorticity transport equation (VTE)
Software tool	Custom developed Navier–Stokes Solver code
Wing geometry	NACA 0014 and 0015
Wing motion kinematics	Pitching and plunging motion at various frequency, amplitude, phase shifts
Re range	600 - 27 000
Results	Time history of drag and lift / Velocity and pressure contour plot

Yu X. et al [49], 2009	
CFD method	3D Navier–Stokes solver over moving overset grids
Software tool	Custom developed Navier–Stokes Solver code
Wing geometry	Custom shaped flat wing with insect body (Fruitfly inspired)
Wing motion kinematics	Heaving and pitching motion
Re range	20 - 600
Results	Time history of vertical and horizontal force coefficient, 3D iso-vorticity surface plots

Ishihara D. et al [50], 2014	
CFD method	3D incompressible Navier–Stokes solver with Fluid Structure Analysis (FSI) addition
Software tool	Custom developed Navier–Stokes Solver code with Lumped torsional flexibility model for FSI
Wing geometry	Insect inspired thin flat wing with leading edge rib
Wing motion kinematics	Heaving motion with various frequencies
Re range	254
Results	Time history of lift and drag and their coefficients, velocity contour and vector plot

Vandenheede R. et al [23], 2014	
CFD method	Three-dimensional, unstructured, pressure-based finite-volume solver written in the Loci framework
Software tool	Proprietary CFD tool Loci-STREAM
Wing geometry	Zimmerman wing - chord of 79.4 mm and a span of 241.3 mm
Wing motion kinematics	Pitching and plunging motion at various frequency, amplitude, phase shifts
Re range	4 800
Results	Time history of lift and thrust coefficients, Vorticity contour plot

Kurtulus D.F. [51, 52], 2016 and 2019	
CFD method	2D and 3D incompressible Reynolds-Averaged Navier-Stokes equations coupled with Menter's Shear Stress Transport (SST) turbulence model
Software tool	Ansys Fluent 6.3.26
Wing geometry	SD7003 airfoil
Wing motion kinematics	Pitching and plunging motion at various frequency, amplitude, phase shifts
Re range	1 000 and 60 000
Results	Time history of lift and drag and their coefficients, velocity contour and vector plot

Poudel N. et al [53], 2020	
CFD method	High-order unsteady Navier-Stokes solver
Software tool	Custom developed Navier–Stokes code
Wing geometry	NACA 0012
Wing motion kinematics	Pitching motion with various frequencies and amplitudes
Re range	12 000
Results	Time history of lift and drag and their coefficients, vorticity contour

2.4 Previous flapping wing bio-inspired aerial vehicle developments

Flapping Wing Bioinspired Aerial Vehicles (FWBAVs) have been developed by various research groups and commercial institute for more than a decade. However, not every attempt has resulted in successful flight. Table 2.4 contains a summarization of technical details of such development published in peer-review publication after successful testing. The clear majority of them are inspired by and in the scale of large insects and small birds. The lightweight construction has frequently taken precedence over other design decisions, including wing geometry and motion profile, which can impact aerodynamic performance. Materials such as carbon fiber, lightweight plastic films, and fabrics are commonly used in construction. While examples like "Festo SmartBird" and Dove feature small batteries for power supply, smaller Flapping Wing Bioinspired Micro Aerial Vehicles (FWBMAVs) inspired by insects often need to be wired to a separate power source, limiting their applicability. All the examples provided below have successfully achieved either forward flight or hovering flight, aligning with the primary objectives of their development. However, achieving precise flight velocity and attitude control remains a challenging task in BAV developments. Combining multiple flight scenarios, such as forward flight, hover flight, landing, and take-off flight, has also proven to be challenging.

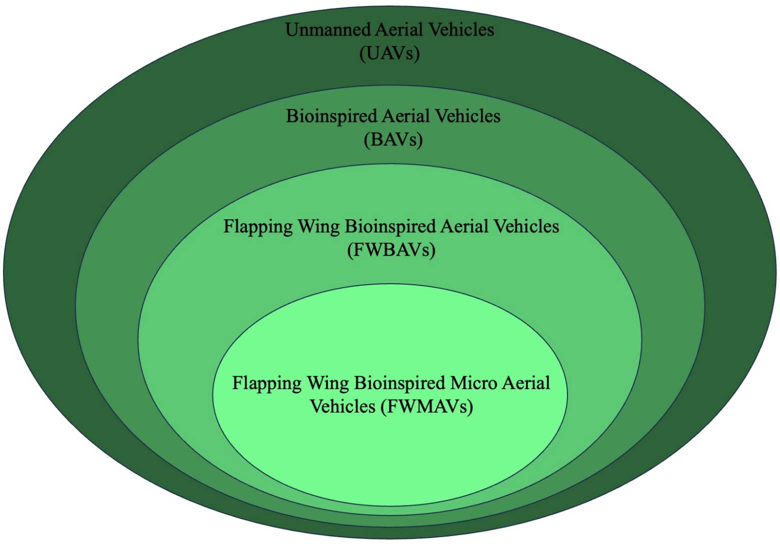

Fig. 2.3: Hierarchical position of Flapping Wing Bioinspired Aerial Vehicles (FWBAV) amoung other similar aircrafts.

TABLE 2.4: Summary of technical details of previous flapping wing bioinspired aerial vehicle development

Pornsin-Sirirak et al [10], 2001	
Vehicle name	Micro bat
Wing contour	Flat (Custom design)
Wing chord	Max chord 35mm
Wingspan	152.5mm
Construction	Carbon fiber spar, Mylar foil membrane
Pitch kinematics	None
Heave kinematics	Wing stroke ±45 degrees
Flapping frequency	30Hz
Flight velocity	Tested with wind tunnel speed of $10ms^{-1}$ in forward flight orientation

R.J. Wood [11], 2008	
Vehicle name	Not mentioned
Wing contour	Flat (inspired Syrphid hoverflies)
Wing chord	Max chord 5mm
Wingspan	30mm
Construction	Carbon fiber reinforced composite beams veins, the membrane is 15 μm thick polyester
Pitch kinematics	None
Heave kinematics	Wing stroke ±50 degrees
Flapping frequency	110Hz
Flight velocity	Hovering flight, peak wing velocity $6ms^{-1}$, peak $Re1200$

Croon et al [12] and Clercq et al [54], 2009	
Vehicle name	DelFly II
Wing contour	Flat (custom design)
Wing chord	Max chord 105mm
Wingspan	280mm
Construction	0.7mm diameter carbon rods viens, siz micron Mylar foil membrane
Pitch kinematics	None
Heave kinematics	Wing stroke ±25 degrees
Flapping frequency	13Hz
Flight velocity	Max forward velocity $7ms^{-1}$, Max backward velocity $1ms^{-1}$, Capable of hovering flight

Krashanista et al [13], 2009	
Vehicle name	Not mentioned
Wing contour	Flat (custom design)
Wing chord	140mm
Wingspan	740mm
Construction	Carbon fiber spars, Nylon cloth wing membrane
Pitch kinematics	None
Heave kinematics	Wing stroke ±55 degrees
Flapping frequency	4-12Hz
Flight velocity	Forward flight velocity $7.25ms^{-1}$

W. Send et al [55], 2012	
Vehicle name	Festo Smartbird
Wing contour	Custom cambered wing with spanwise variation
Wing chord	Mean wing chord 250mm
Wingspan	2000mm
Construction	Carbon fiber spars, gears and linkages, Flexible blow molded plastic skins for wings and fuselage
Pitch kinematics	Pitch angle ±7 degrees, Only the tip section of the wings
Heave kinematics	Wing stroke ±45 degrees, an articulated wing with a spanwise variation of stiffness
Flapping frequency	2Hz
Flight velocity	Forward flight velocity $5ms^{-1}$ (Max achieved $10ms^{-1}$), Capable of gliding flight

Keennon et al [14], 2012	
Vehicle name	Not mentioned
Wing contour	Flat (custom design)
Wing chord	Max wing chord 140mm
Wingspan	165mm
Construction	Carbon fiber spars, Mylar foil membrane
Pitch kinematics	None
Heave kinematics	Wing stroke ±100 degrees
Flapping frequency	30Hz
Flight velocity	Max forward velocity $6.7ms^{-1}$, Capable of hovering fligh

Gerdes et al [15], 2012	
Vehicle name	Robo Raven
Wing contour	Flat (custom design)
Wing chord	Mean wing chord 248mm
Wingspan	1168mm
Construction	Carbon fiber stiffening rod spars, 0.001 inch thick Mylar membrane
Pitch kinematics	None
Heave kinematics	Wing stroke ±50 degrees
Flapping frequency	4Hz
Flight velocity	Forward flight velocity $6.7ms^{-1}$

Yang et al [16], 2017	
Vehicle name	Dove
Wing contour	Custom developed cambered flexible wing
Wing chord	Max chord 100mm
Wingspan	500mm
Construction	Carbon fiber spars, Mylar foil membrane wing, Thin plastic
Pitch kinematics	None
Heave kinematics	Wing stroke ±50 degrees
Flapping frequency	4-12Hz
Flight velocity	Forward flight velocity $8-12ms^{-1}$, Capable of gliding flight

CHAPTER 3

EXPERIMENTAL INVESTIGATION OF AERODYNAMICS OF BIOINSPIRED PITCHING AND PLUNGING WINGS

3.1 Overview

The ability of animals to generate lift and propulsion by flapping their wings has been a subject of fascination and scientific inquiry for centuries. Bioinspired aerodynamics has been important in engineering research for the development of flapping wing air vehicles, morphing wing aircraft, and bioinspired wind turbine technologies. Research interest in flapping wing unmanned aerial vehicles has increased significantly in recent years. Harnessing unique flight characteristics of birds like maneuverability, endurance, and efficiency is the primary objective of such developments [2, 7]. Rotary and fixed wing UAVs are yet to showcase the efficiency and the adaptability observed in birds [8, 9]. In the pursuit of more efficient and maneuverable UAV development, the logical trajectory is replicating birds as technologically permissible. The recent advancements in computation, electronics, and fluid dynamics have paved the way for a renaissance in bioinspired fluid dynamics and its applications.

The development of bio-inspired aerodynamic applications demands knowledge of unsteady aerodynamics, especially in areas such as aerodynamic force generation, flow manipulation, and wake structure interaction of flapping wings. Researchers have been attempting to measure the forces and visualize the flow behavior with increasing accuracy and resolution using different methods. The use of live birds in laboratory experiments of their aerodynamic performance presents a unique set of challenges and contains both advantages and disadvantages compared to the use of robotic systems. Training birds to perform a certain maneuver inside a laboratory or a wind tunnel facility require time and effort and even then, the repeatability and the consistency of the maneuver would be uncertain. Aerodynamic forces and pressure variation on the wing are difficult to measure using live birds due to challenges in sensor development and positioning. Un-instrumented investigations [56], and experiments using preserved birds [57] have been used as solutions for these challenges. With the introduction of miniature actuators and computer control systems, robotic replications of bird wing motion have gained recognition as the most widely used approach in bio-inspired aerodynamics. Apart from accurate repeatability, and ease of sensor positioning, the similarity between the mechanisms used in experimental apparatus and Flapping Wing Bioinspired Aerial Vehicles (FWBAVs) are advantageous of this approach.

Understanding the aerodynamic performance of flapping wings in varying kinematic, environmental, and geometrical settings is the main building block of FWBAV development. Renewed interest and innovative applications have highlighted gaps in existing knowledge in flapping wing aerodynamics [58]. Although experimentally obtained force characteristics of pitching and plunging wings have been published by previous studies, the majority of them focus on specific or custom wing designs [17–21]. And also the existing investigations often focus on specific combinations of $Re$and St values in term of flight speed and wing motion mechanics. [22–25]. Therefore, they are limited in understanding the overarching characteristics of flapping wings in the large range of motion showcased by birds of flight. As show in Table B.1, the Re and St ranges of birds in forward flapping flight have been calculated using the measurements by Bruderer [33, 34]. The range of Re was found to be between 8.3×10^3 and 1.4×10^5, while the St ranges from 0.018 to 0.119 after analyzing data from sixty bird species.

In the pursuit of developing FWBAVs capable of performing efficient flights under various conditions, transient experimental measurements of lift and thrust are vital to identify and analyze the aerodynamic mechanism in flapping wing. Such discussion could be vital in further improving FWBAVs of the future. However, the availability of such data in varying wing kinematics is scarce. Some investigations illustrate the mean lift and thrust values of a wing in periodic motion eliminating the opportunity to discuss the transient nature of force generation [59, 60]. Modern FWBAVs are limited in terms of forward flight speed and wing flapping frequency and only cover a very small portion of the range showcased by birds [10–16]. However, these developments demonstrate that FWBAVs with further advancements have the potential to achieve the maneuverability, endurance, and efficiency of birds. But insufficient data on the force generation of flapping wings in a wider kinematic range is affecting the development of more efficient and maneuverable FWBAVs. The aim of this investigation is to address these two issues. Due to limitations caused by mechanical and electronic components, perfect replication of bird wings is yet to be achieved. Hence, simplified flapping wing mechanisms and kinematics are used in previous developments of FWBAVs [10–16]. Inspired by such examples, a simplified wing with an airfoil shape of NACA 0012 is used so that a broad collection of resources are available to reinforce the findings. Ease of manufacturing while preserving dimensional accuracy was also a contributing factor in using a simplified wing shape.

3.2 Methodology

3.2.1 Mechanics of the wing

As illustrated in Fig. 3.1, the distribution of Re and St of these 60 bird species shows that about 78% of them fly below Re 1×10^5 and use St values below 0.1. Therefore, the investigation was divided into fourteen groups with varying values of Re and St to cover the range of interest as mentioned in table 3.1. Upper bounds for Re and St ranges investigated are also enforced by the limitations of motors in the apparatus.

The pitch and plunge motion of the wing are modeled after sinusoidal functions. Sinusoidal functions are a close approximation of the true wing kinematic profile in pitch and plunge motions. The use of sinusoidal functions allows for precise control and replication of motion profiles in current and future investigations. FWBAVs tend to favor sinusoidal movements for the motion of wings for similar reasons.

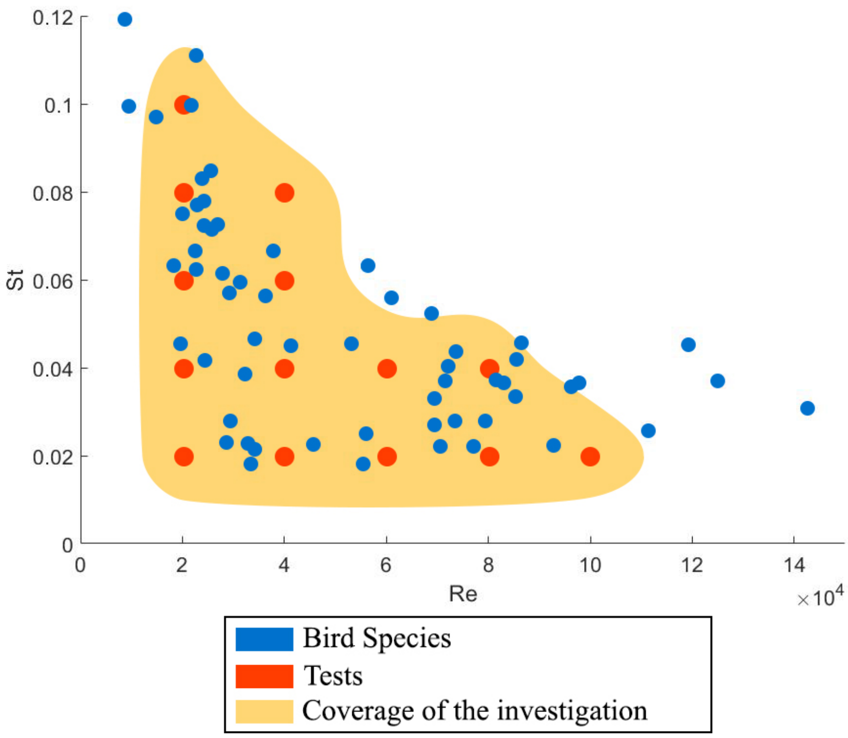

Fig. 3.1: St and Redistribution of forward flapping flight of the birds with experimental investigation coverage indicated.

3.2.2 Wing geometry

Wings are defined as one of the paired structures employed by certain animals to propel themselves in the air. They are classified according to a variety of factors including wingspan, chord length, wing bone and muscle structure, skin and feather struc-

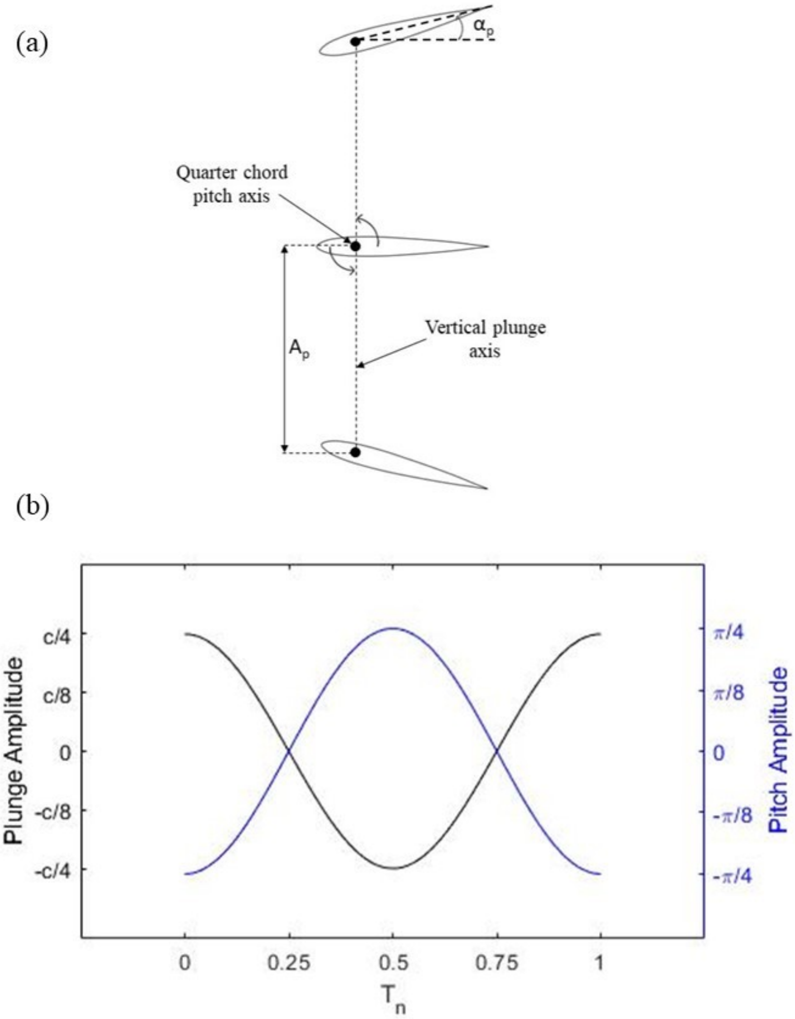

Fig. 3.2: (a)Diagram of wing motion, (b)Displacement-time graphs of plunge and pitch motion of the wings.

ture, and wing behavior under aerodynamic load. Diane Chin and David Lentkin [29] have classified wings of flying animals into flexible wings, membranous wings, minimum morphing feathered wings, and morphing feathered wings. The majority of bird wings are morphing feathered wings capable of both active and passive variations of the shape.

The combined effect of segmentation and morphing increases the complexity of bird wing motion. Such characteristics enable birds to manipulate the wings to suit different flight conditions. The muscles and feathers enable the wing to facilitate both active and passive wing morphing. For the initial investigation of bird wings, the geometry and motion of the wing are kept elementary. In this investigation, joints of the wing and its ability to morph are precluded to focus the analysis on wing kinematics like the pitching and plunging motion. This simplification permits the use of fused

TABLE 3.1: Division of the experimental investigation into groups with varying Reynolds and Strouhal number values

Re	0.02	0.04	0.06	0.08	0.1
20 000	Group A	Group B	Group C	Group D	Group E
40 000	Group F	Group G	Group H	Group I	
60 000	Group J	Group K			
80 000	Group M	Group N			
100 000	Group O				

filament fabrication 3D printing for manufacturing the wing sections. The 3D printer has a precision of 0.1mm. The dimensional accuracy of the wing was confirmed using a non-contact CNC vision measuring system.

A wing selected for a FWBAV is required to perform effectively under different flying conditions. Flapping forward flight, gliding forward flight, direction changes during flight, and hovering flight are among them. The final wing design would most likely be a complex three-dimensional shape with multiple sections with varying airfoil shapes. For the development of such a wing design, experimental data on the aerodynamic performance of different airfoil shapes in varying flight conditions are vital. The use of NACA airfoil shapes in this initial investigation allows us to understand the underlining aerodynamic phenomena of hovering flight and the effect of different geometrical feathers on aerodynamic performance. Furthermore, the discussion of results is assisted and substantiated by the already existing compilation of data on the aerodynamic performance of NACA airfoils.

The chord length of a wing in a FWBAV is determined by the size and payload capacity of the vehicle. Applications for nano-scale and micro-scale bioinspired aerial vehicles are limited due to their inability to carry payloads and restricted range [14]. Unmanned Aerial Vehicles (UAVs) in the scale of medium to large birds promise greater potential applicability. Therefore, wings in the range of 0.075m to 0.150m were used in the investigation while the data presented were gathered using a wing with a chord length of 0.075m. The selection was also confined by the test section size of the wind tunnel and the maximum solid and wake blockage ratios permitted.

The final wing model's surface quality was regulated due to its significant impact on aerodynamic performance [61]. Standards for surface roughness of wind tunnel models followed by NASA recommend surface roughness (R_a) to be kept close to 1µm [62]. This was achieved by wrapping the sanded and painted wing assembly in laminated plastic sheets.

TABLE 3.2: Surface roughness measurements of the wing after different treatments

Roughness value (μm)	Untreated 3D print	Sanded (800 grit)	Spray-painted with primer	Covered with laminated sheets
R_a	17.13	9.44	4.78	1.01
R_z	76.123	48.29	19.74	5.26
R_q	20.31	10.64	5.51	1.54

3.2.3 Decomposition of bird wing motion

Biomechanics of bird and insect wings are complex and consist of multiple movements of muscles, skeletal structures, membranes, and feathers. All these components work in unison to enable the animal to perform complicated wing motions. Wing motions of flying animals vary depending on the animal species, the objectives of the flight, and environmental conditions. Since segmentation and morphing are precluded in this investigation, the motion of an animal wing is simplified by decomposing it into multiple sub-motions as given in Fig. 3.2. This enables experimental investigation of the effect of each sub-motion on the aerodynamic performance of the wing. Pitch and plunge sub-motions are selected for this investigation based on conclusions of previous studies by Platzer et al [58] and Lai and Young [63]. They state the reason for the preference for combined pitch-plunge as the increased thrust forces and propulsive efficiency compared pitch-only or plung-only motions.

Effects of pitch axis location and plunge axis angle variation on the aerodynamic performance of flapping wings have rarely been discussed in previous studies. However, pitch axis location changes from one bird species to another based on their shoulder joint location, and every bird species have been observed to use varying plunge axis angles in different phases of their flight. During the extensive literature review, experimental or computational investigations on these two mechanisms were rarely found which emphasizes the requirement of a rigorous investigation. The experimental set-up was designed and developed with these objectives in mind.

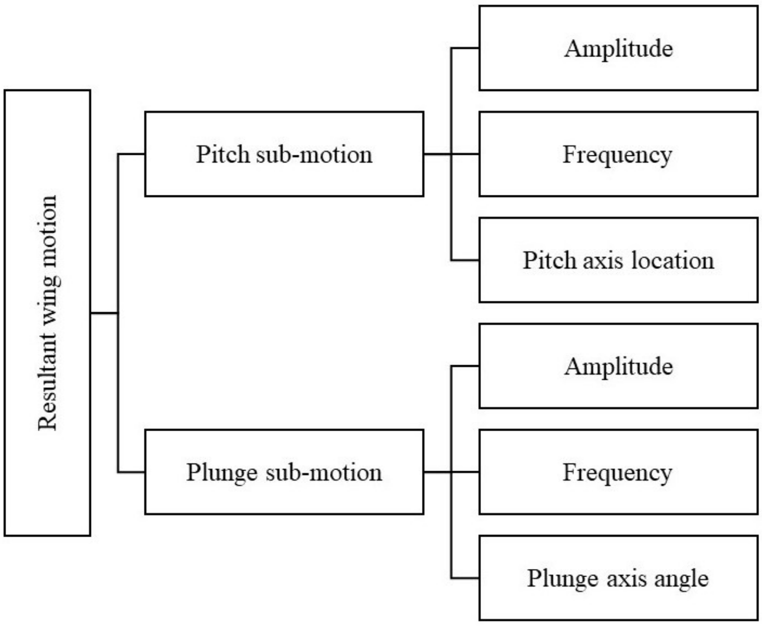

Fig. 3.3: Decomposition of wing motion into independently controllable variables.

3.2.4 Mechanical design of the apparatus

The wing motion control system consists of three sub-assemblies as shown in the figure below. The purpose of the support structure sub-assembly is to provide stable structural support to all the components. The electronics housing creates a dust-free space for the control electronics in the primary structure, which enables the entire system to be relocated easily as a singular entity. The wide base design provides stability and enables the platform sub-assembly to tilt in a cantilever arrangement. Adjustable leg mounts allow for leveling on uneven floors. The bearing-mounted shaft on top of the support structure is rotated through a worm and wheel gear mechanism driven by a stepper motor to tilt the platform sub-assembly. The self-locking feature and 30:1 gear reduction of the worm and wheel gear mechanism enable the platform to be tilted at very small angles and locked in place. This feature enables the angle of the plunge axis to be varied.

The platform sub-assembly moves the wing in pitching and plunging motions. The pitching motion is provided by a stepper motor connected to the wing. Said motor is fixed onto a plate driven vertically via the ball screw mechanism rotated by a second stepper motor. To achieve the required vertical translational velocity of the wing during plunging motion in high St and Re values, the second stepper motor needs high RPM and torque performance due to the ball screw mechanism's 2mm pitch. Therefore, a custom-developed gearbox is used to connect the stepper motor to the ball screw. The gearbox consists of two helical gears made of 3D printed plastic with metal inserts for secure connection with motor and ball-screw shafts. The gearbox increases the

TABLE 3.3: Technical specification of the USL06-05 single-axis force sensor

Item	Details
Rated capacity	$\pm 200N$
Rated output	Approx. 0.90 mV/V) $1800\mu\varepsilon$
Allowable overload	200%
Non-linearity	± 1% R.O. (After applying interference correction)
Hysteresis	± 1% R.O. (After applying interference correction)
Interference	± 1% R.O. or less
Guaranteed temperature range	10 to 60^oC (No condensation)
Temperature effect on output	± 0.03% / ^oC

rotation velocity of the ball screw eight times to achieve the translational velocity in plunge motion needed to cover all the kinematic cases of the wing motion.

To achieve precision control of the sinusoidal motion in the plunge control motor, a PID feedback system is implemented using a rotational encoder. The pitch control stepper motor does not require an encoder since its angular changes are small and can be preciously controlled by the built-in stepping mechanism. The load cell arrangement is fixed in between the pitch control motor and the wing sub-assembly. The load cell used is a USL06-H5 single axis force sensor with specifications given in Table 3.3. The force sensor is limited only to measure compression and tension forces in a single axis. Therefore, a mechanism was developed to translate the forces on the wings to the compression and tension forces on the force sensor. Furthermore, to measure both thrust and lift forces on the wing, the experiment has to be repeated with varied force sensor orientation as explained in the experimental procedure section.

The apparatus is developed to be completely detachable from the wind tunnel without any permanent alterations to the wind tunnel. All components, including the control system electronics, are designed and developed in modular form for easy maintenance and updating. The mechanism is designed to be used beyond the scope of this investigation in both research and practical demonstrations in undergraduate studies.

For more details of the design, operation, and maintenance of the experimental apparatus please refer to Appendix A: User manual for the experimental apparatus.

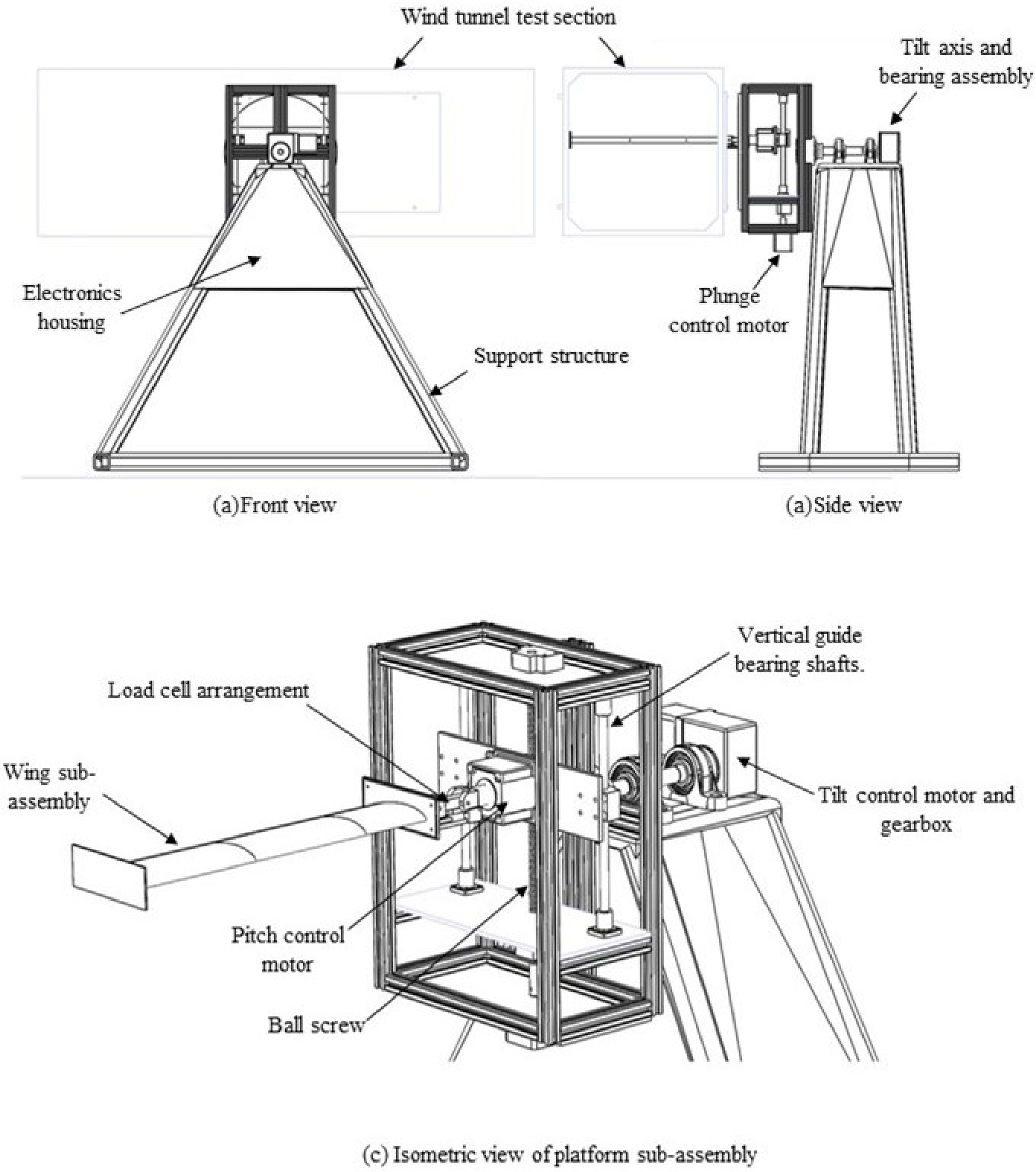

Fig. 3.4: Experimental apparatus (a) Front view and (b) Side view of the apparatus, (c) Isometric view platform sub-assembly

3.2.5 Control system design of the apparatus

The control system transfers information between the computer and motors controlling wing motion, while also sending force measurement data from the force sensor back to the computer. All electronic components of the system are housed inside the dust-free enclosure. A 24V power supply provides the electrical power required for the system.

Multiple voltage regulators are used to step down the voltage as suitable for sensors and other equipment. A "Raspberry-Pi" computer is used as the control center which is capable of wireless communication with a computer. The stepper motor controllers govern the motion of the three stepper motors. The motors are connected to the wing as described in the mechanical design. The analog signal from the force sensor is amplified and regulated before being converted into digital signals and transferred back to the "Raspberry Pi". The "Raspberry-Pi" saves the measurements with the synchronized angular position of the wing in both pitch and plunge motions using data from motor encoders. These measurement files are processed to compute the lift and thrust coefficient results.

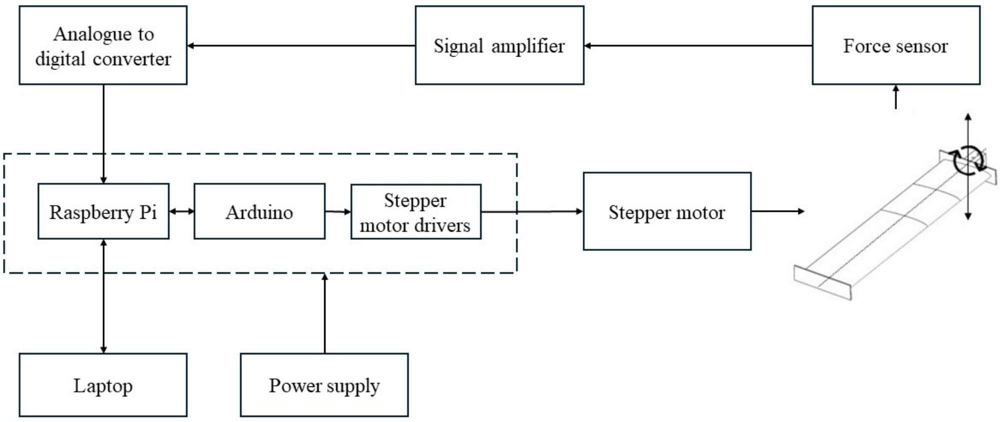

Fig. 3.5: Control system diagram of the wing motion control system and data acquisition system

3.3 Experiment and data processing procedure

3.3.1 Experiment procedure

The experiment apparatus was positioned adjacent to the wind tunnel with the wing inside the test section as shown in Figure 3.4. The angular orientation of the wing was adjusted to be horizontal at the beginning of each experiment. Due to the capability of the available force sensor, aerodynamic forces parallel and perpendicular to the wing chord were measured separately in two stages. For each Group in Table 3.1 pitching and plunging motion scenarios were investigated. For each motion, two sets of data were collected. They are

1. Force measurements without wind with very minimum possible velocity in wing motion (quasi-steady-state) – M1
2. Force measurements with the wind in velocities determined by $Re$and St calculations – M2

The purpose of taking three measurements is to isolate aerodynamic forces generated by the wind and wing motion separately with minimum error. Each of these measurements is taken in two instances to minimize the effect of any random errors. In each instance, the force measurements are taken for a minimum of 15 wing motion cycles.

The saved data files were analyzed using a custom-developed MATLAB program. Data filtration, reduction, and uncertainty calculations were carried out in stages to compute the lift and thrust coefficient values and their uncertainty range.

Measurements were taken at a 250 Hz sampling rate. The data are filtered using a three-step filtering process using Butterworth, moving average, and Chebyshev filters which have been successful in multiple previous investigations as mentioned in Table 2.2. The fourth-order low-pass Butterworth filter is used to attenuate the data with a frequency higher than the cutoff frequency value. The desired cut-off frequency is determined by analyzing the frequency distribution of the measurement data. The power spectrum density versus frequency plot assists in identifying the desired cut-off frequency [64]. The moving average filter is used to reduce random noise while retaining a sharp step response. The number of elements used for the average is optimized

TABLE 3.4: Terminology used in naming unsteady aerodynamic force data

Group	Measuring orientation	Wing motion	Measuring instance	Test number
Group letter	C: parallel to the chord, P: perpendicular to the chord	PP: pitching and plunging only	M1,M2	test1 and test2

by comparative analysis of multiple results. The low-pass Chebyshev filter is used for further improvement of the smoothness of the data variation. The four parameters needed to fully define the Chebyshev filter are low-pass response, the cutoff frequency, the percent ripple in the passband, and the number of poles [65]. Refinement of filter parameters is important to retain the characteristics of the results while reducing noise.

After the three-stage filtering process, measurement data are divided into wing-motion cycles using the wing-motion kinematic data as a reference. These separated data sets are used to compute the average variation and standard deviation. To isolate measurements due to pitching and plunging wing motion, quasi-steady-state measurements (M1) with corresponding wing orientation are subtracted from unsteady measurements (M2). The voltage measurements were converted into force measurements using the calibration data and the lift and thrust coefficient values were computed. The flow chart in Fig. 3.6 and the data reduction Equations for 5 to 8 would further illustrate the steps of the data processing procedure.

$$\begin{aligned} V_P &= V_{PM2} - V_{PM1} \\ V_C &= V_{CM2} - V_{CM1} \end{aligned} \tag{3.1}$$

$$\begin{aligned} F_P &= mV_P + n \\ F_C &= mV_C + n \end{aligned} \tag{3.2}$$

$$\begin{aligned} F_D &= F_P Sin\alpha + F_C Cos\alpha \\ F_L &= F_P Cos\alpha - F_C Sin\alpha \end{aligned} \tag{3.3}$$

$$\begin{aligned} C_D &= \frac{F_D}{0.5 * \rho V^2 cl} \\ C_L &= \frac{F_L}{0.5 * \rho V^2 cl} \end{aligned} \tag{3.4}$$

$V_{P/C}$	Voltage measurement perpendicular/ parallel to the wing chord
m, n	Calibration coefficients
$F_{P/C}$	Force measurement perpendicular/ parallel to the wing chord

F_L	Lift force
F_D	Drag force
C_L	Lift coefficient
C_D	Drag coefficient
ρ	Air density
V	Freestream velocity
c	Wing chord length
l	Wing span length

3.3.2 Uncertainty analysis

Uncertainty analysis is a mandatory component of any experimental study. In this investigation, A survey was conducted during the development stage of the experimental apparatus to identify and minimize measurement uncertainties. However, due to technical limitations, some uncertainties are inevitable. An uncertainty analysis was carried out to identify precision errors in the measured data and calculate ranges for result confidence levels. The 95% confidence large sample uncertainty assessment approach is used in this investigation as recommended by AIAA. Identification of uncertainty contributors for each measurement requires theoretical knowledge and experience in experimental fluid dynamics. Therefore, the list of errors provided by the advisory report of fluid dynamics of AGARD for NATO is referred for the uncertainty analysis [62].

The absolute uncertainty of the measured voltage is calculated as half of the difference between the maximum and minimum values for each instance of the separated cycles. The general equation of uncertainty propagation through the data reduction equation is given in Equation 9. Application of this general conversion to equations 5, 6, 7, and 8 would result in their corresponding equations being used for fractional uncertainty propagation through these data reduction equations. Assume their numbering as 10, 11, 12, and 13. The flow chart illustrating the data processing procedure in Figure 3.6 would further explain the use of these equations.

$$\delta_{Ab} = \frac{M_{max} - M_{min}}{2} \tag{3.5}$$

$$\begin{aligned} |\sigma_{V_P}| &= \sqrt{\sigma^2_{V_{PM2}} + \sigma^2_{V_{PM1}}} \\ |\sigma_{V_C}| &= \sqrt{\sigma^2_{V_{CM2}} + \sigma^2_{V_{CM1}}} \end{aligned} \tag{3.6}$$

$$
\begin{aligned}
|\sigma_{F_P}| &= \sqrt{\sigma_m^2 + \sigma_{V_P}^2 + \sigma_n^2} \\
|\sigma_{F_C}| &= \sqrt{\sigma_m^2 + \sigma_{V_C}^2 + \sigma_n^2}
\end{aligned} \tag{3.7}
$$

$$
|\sigma_F| = |\sigma_{F_D}| = |\sigma_{F_L}| = \sqrt{\sigma_{R_P}^2 + (Cos\alpha.\sigma_\alpha)^2 + \sigma_{R_C}^2 + (Sin\alpha.\sigma_\alpha)^2} \tag{3.8}
$$

$$
|\sigma_{C_D}| = |\sigma_{C_L}| = \sqrt{\sigma_F^2 + (-2.\sigma_V)^2 + (-1.\sigma_c)^2 + (-1.\sigma_l)^2} \tag{3.9}
$$

Uncertainty of the chord and span length measurements are calculated using the

TABLE 3.5: Measurement variables and their uncertainty contributors

Variables	**Description**	**Measuring method**	**Uncertainty contributors**
α	Angle of attack of the wing	Using a digital level gauge	Calibration methods Zeroing of reading
c	Chord length of the wing	Using a Vernier caliper	Calibration methods Zeroing of reading
l	Span length of the wing	Using a measuring tape	Calibration methods Zeroing of reading
V	Free stream speed of the flow	Using a hot wire anemometer	Calibration methods Zeroing of reading Temperature reading Data acquisition instrument signal conditioning
V_p, V_c	Voltage measurements from the force sensor	Using usl06-h5 series 1-axis load cell	Calibration methods Calibration standard weight and/or load cells Model and balance dynamic motion pitch, plunge, and tilt Balance attachment technique to model zeroing of reading Mechanical and structural design of the balance Temperature effect Data acquisition instrument signal conditioning

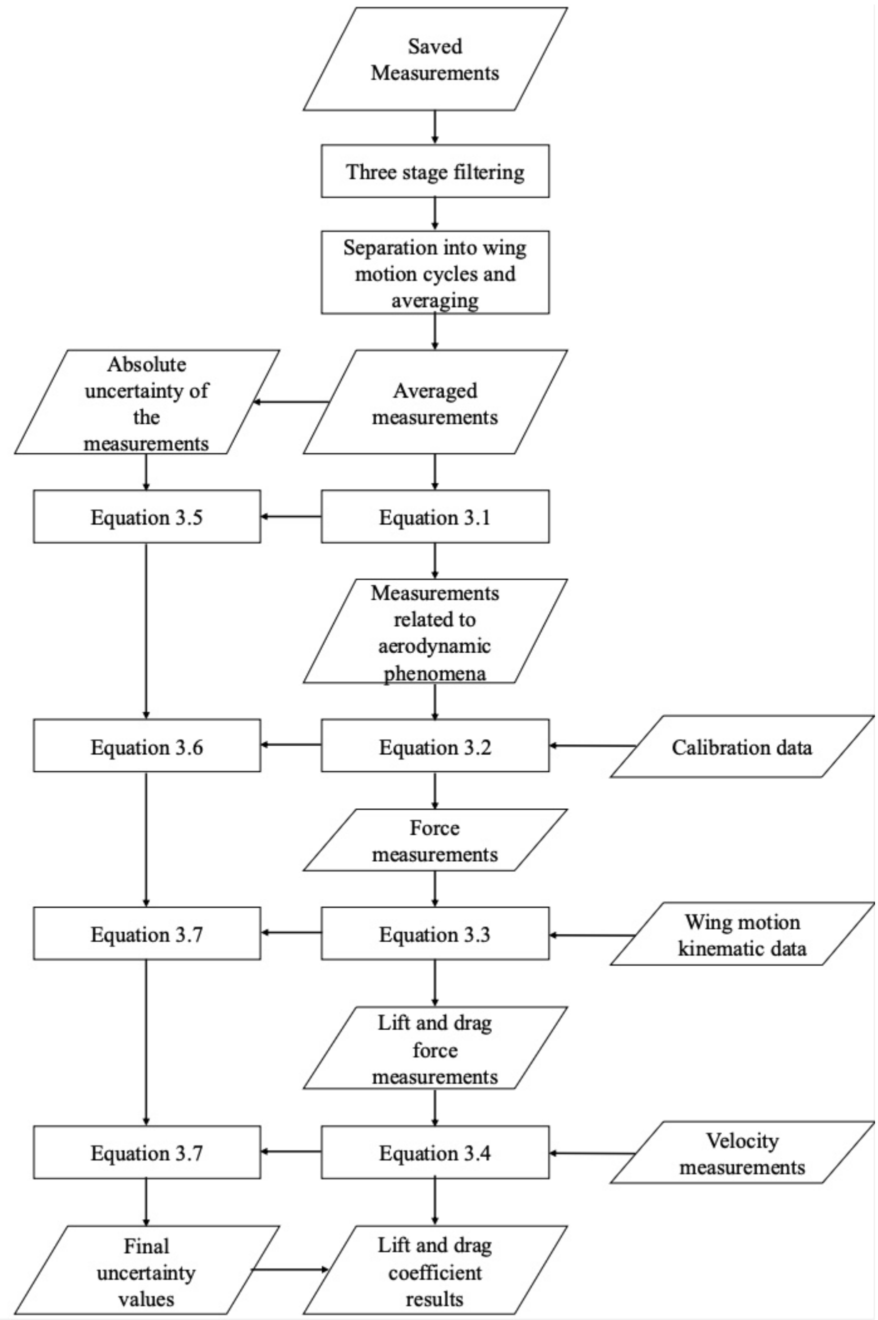

Fig. 3.6: Flow chart illustrating the data processing procedure

equation for the uncertainty of scale measuring devices $\delta = \frac{smallest\ increment}{2}$. The uncertainty of the angle and wind velocity measurements is calculated using the equation for the uncertainty of digital measurement devices $\delta = smallest\ increment$. All the uncertainty values are converted into percentile uncertainties before propagation through data reduction equations. The corresponding percentile uncertainty propagation equation for each data reduction equation can be generated using the following method. If the measured quantities are $x \pm \delta(x), y \pm \delta(y).....z \pm \delta(z)$ and used to compute a results which has a form of $R = R(x, y...., z)$. The general percentile uncertainty in R is given by,

$$\sigma(R) = \sqrt{\left[\sigma(x)\frac{\partial R}{\partial x}\right]^2 + \left[\sigma(y)\frac{\partial R}{\partial y}\right]^2 + ... + \left[\sigma(z)\frac{\partial R}{\partial z}\right]^2} \tag{3.10}$$

3.3.3 Validation of the measurements

The experimental apparatus and measurement methodology are validated by recreating the experimental investigation by Kim et al. [66]. In the referred experimental investigation, a NACA 0012 airfoil was subjected to pitching motion in varying reduced frequency values (K) and Re. In the test case used for the validation, Re is 4×10^4 and K is 0.1. Comparison of lift coefficient (C_L) and drag coefficient (C_D) time series variations of Kim's experimental results and results of this investigation is shown in Figure 3.7.

The agreement of the experimental measurements using the experimental apparatus with the results from Kim's investigation was calculated using the Procrustes analysis. In the analysis, the difference between the two curves of average experimental force coefficient values and results from Kim's investigation is calculated. The resultant linear transformation coefficients of the analysis for both C_L and C_D comparisons were computed to be 1, meaning the best possible correlation between the two curves. The standard deviations variations observed near the peaks and troughs can be attributed to the unsteady nature of the underlying aerodynamic phenomena that influence the generation of lift and drag by the wing.

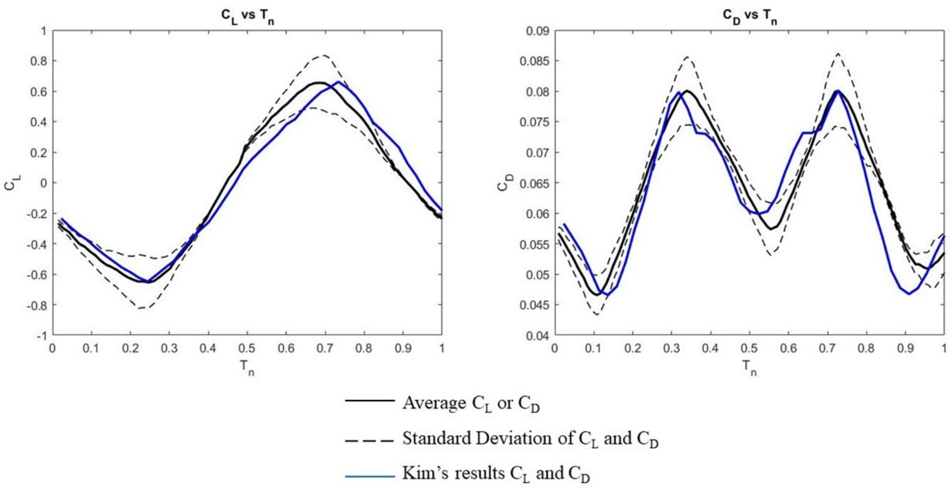

Fig. 3.7: Comparison of experiments results for validation.

3.4 Results and discussion

Transient variations in C_L and C_T values were analyzed for an average motion cycle in fourteen test groups with varying kinematics. The standard deviation range indicates stability in force generation across motion cycle stages, while the 95% confidence range accounts for random error. The close proximity of these ranges underscores the confidence in the experimental investigation. Experimental measurements of the transient force coefficients provide a detailed discussion of the aerodynamic mechanisms involved. All test groups show two local minimums in both C_L and C_T but at different times in the wing motion cycle. Although the geometry of the wings and the motion are symmetric, the two local minimums in the curves of both C_L and C_T show clear differences. Similar shapes are observed in the C_L and C_T curves across all test groups, but characteristics that differ from the values Re and St can be identified.

The comparison of average lift and thrust coefficients as shown in Fig. 3.13 illustrates trends between the scenarios with different $Re$and St values. The mean values of lift and thrust coefficients increase by an average of 35% and 83% respectively with increasing Strouhal number in Reynolds number values of 20 000 and 40 000. The same trend is less pronounced in Revalues of 60 000 and 80 000. However, mean lift coefficient values decrease by an average of 46% with rising Revalues as St values are at constant at 0.02 and 0.04. While the mean thrust coefficient values showcase both rising and receding trends with increasing Re. The standard deviation values of the mean coefficients represent the dynamic nature of the transient forces and provide insight into the stability of a FWBAV.

3.4.1 Key characteristics in transient results

In C_L variations, the trends of increasing lift with the downstroke and decreasing lift with the upstroke are distinct. The effective angle of attack can be identified as the primary contributor to this behavior. Changes in the angle of attack favor lift generation as the wing moves further into the downstroke while pitching. However, contrary to a steady state wing, the pitching and plunging motion of the wing create additional aerodynamic mechanisms that change the effective angle of attack. Multiple investigations have concluded the presence of stable LEV below $Re 1 \times 10^5$ and its contribution to changing effective AoA and improving lift generation in a flapping wing [67–69]. Shyy and Lui state that the LEV is generated by the equilibrium of the pressure gradient, the centrifugal force, and the Coriolis force [70]. The presence of the LEV creates a low-pressure region that generates suction on the upper surface. In these investigations, LEV has been found to increase the lift above the critical angle of attack during wing translation by attaching a vortex core to the upper leading edge. According to Platzer et al [58], the flow behavior of micro air vehicles with flapping wings in low

Re is complex because efficient thrust generation is achieved via both LEV and TEV shedding. These vortices continue to affect force generation after detaching from the surface of the wing through interactions with the airflow surrounding the wing.

Another common feature of C_L variations in all groups is elevated lift generation near stroke reversal. Similarly, C_T variations show clear increments around stroke reversal. According to Birch and Dickinson, thrust elevations were observed near stroke reversal due to the beneficial effect of wing-wake interactions [71]. Interactions between the detached vortices and the flow field of the wing are defined as wing-wake interactions. Experimental flow visualizations and Navier-Stokes simulations of flapping wing aerodynamics have observed that detached vortices influence the flow around the wing [72, 73]. These interactions can have beneficial and nonbeneficial effects during forward flight [74]. The effects of wing wake interaction are dominant near stroke reversal because vortices tend to detach with the stroke reversal and rotational and translational motion of the wing are minimal at stroke reversal. The probability of wing wake interaction is highest in scenarios with high St and low Re flapping wings. This is because detached vortices are not convected rapidly by the flow, allowing them to interact with the moving wing. Evidence of this trend is apparent in the time series data of C_T of the test groups, as with increasing St the peaks and the average values of C_T increase.

Among the test groups, there are five groups each with 20 000 $Re$and 0.02 St . A comparison of the transient force coefficients of these groups is illustrated in Fig. 3.1. Comparison of results from other groups highlights characteristic and gradual variations among C_L and C_T curves. The results from the Re 20 000 and St 0.02 test group shows a significant phase shift compared to the other results in both C_L and C_T variations. Significant differences in the magnitude of local minimums and maximum values are observed with varying Re and St . The comparison of groups with St at 0.2 showcases a gradual decrement of C_L and C_T maximum and minimum magnitudes as Re increases from 20 000 to 100 000. However, the lift and thrust forces would have increased with the Re. In constant Re of 20 000, clear increments of C_L maximum and minimum values which occure around 0.5 and 0.9 T_n are observed with increasing St values. However, in C_T comparison of the same groups, only the group with St with 0.04 shows a considerable deviation in minimum and maximum values. Changes in St values are more effective in altering the resultant aerodynamic forces as the ranges of the second set of plots are much greater than those of the first set.

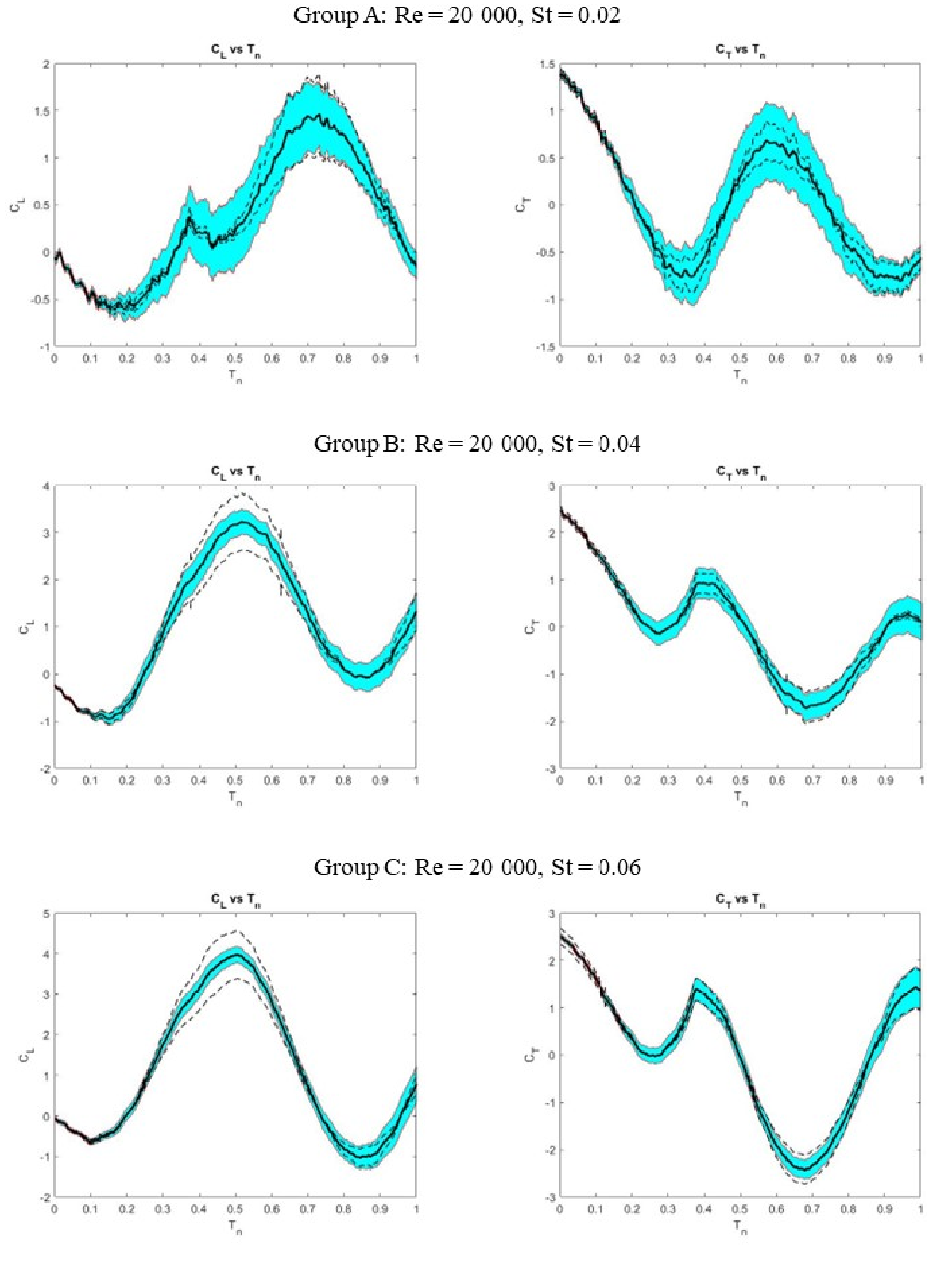

Fig. 3.8: C_L and C_T variation of groups A,B,C

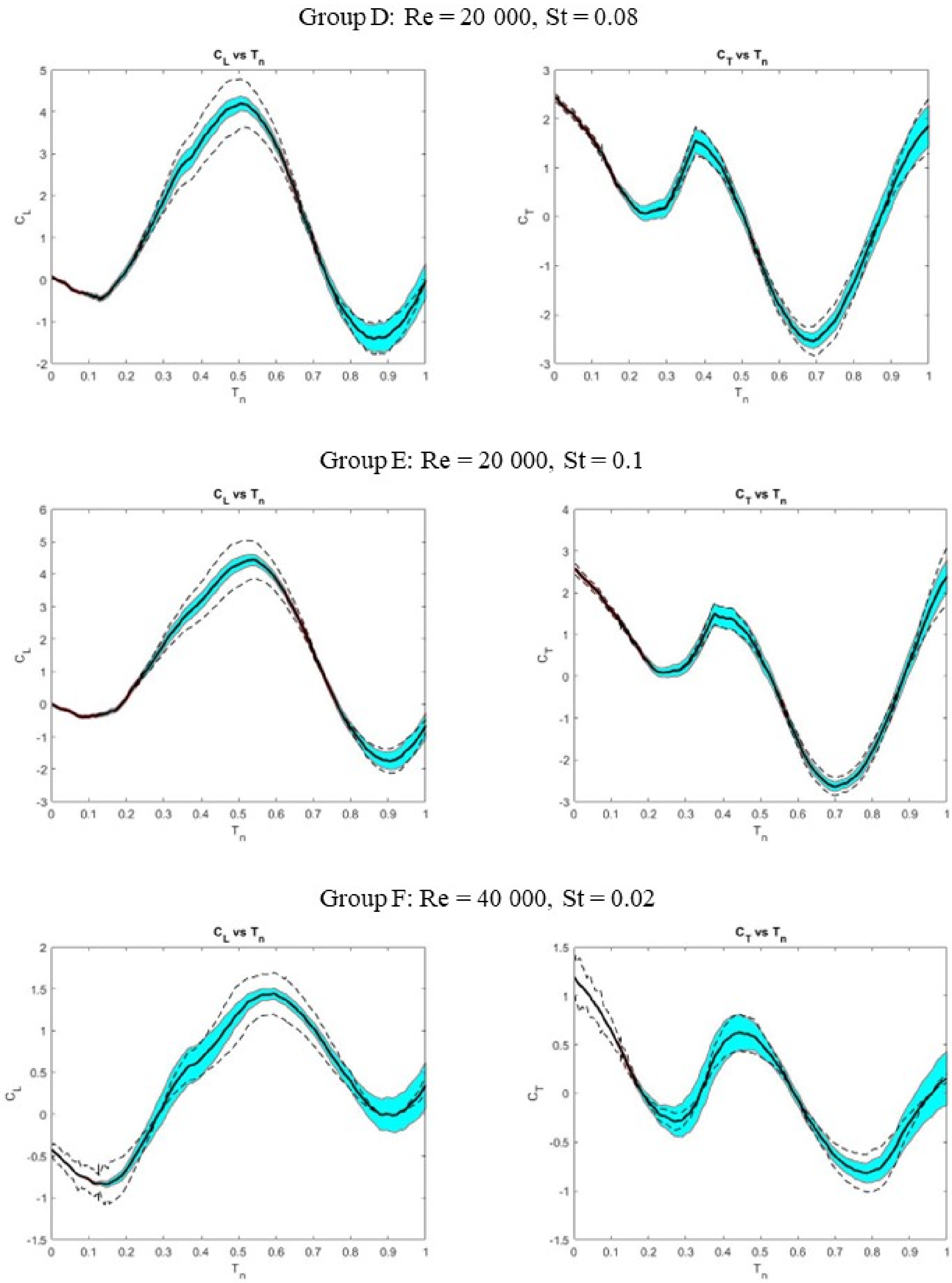

Fig. 3.9: C_L and C_T variation of groups D,E,F

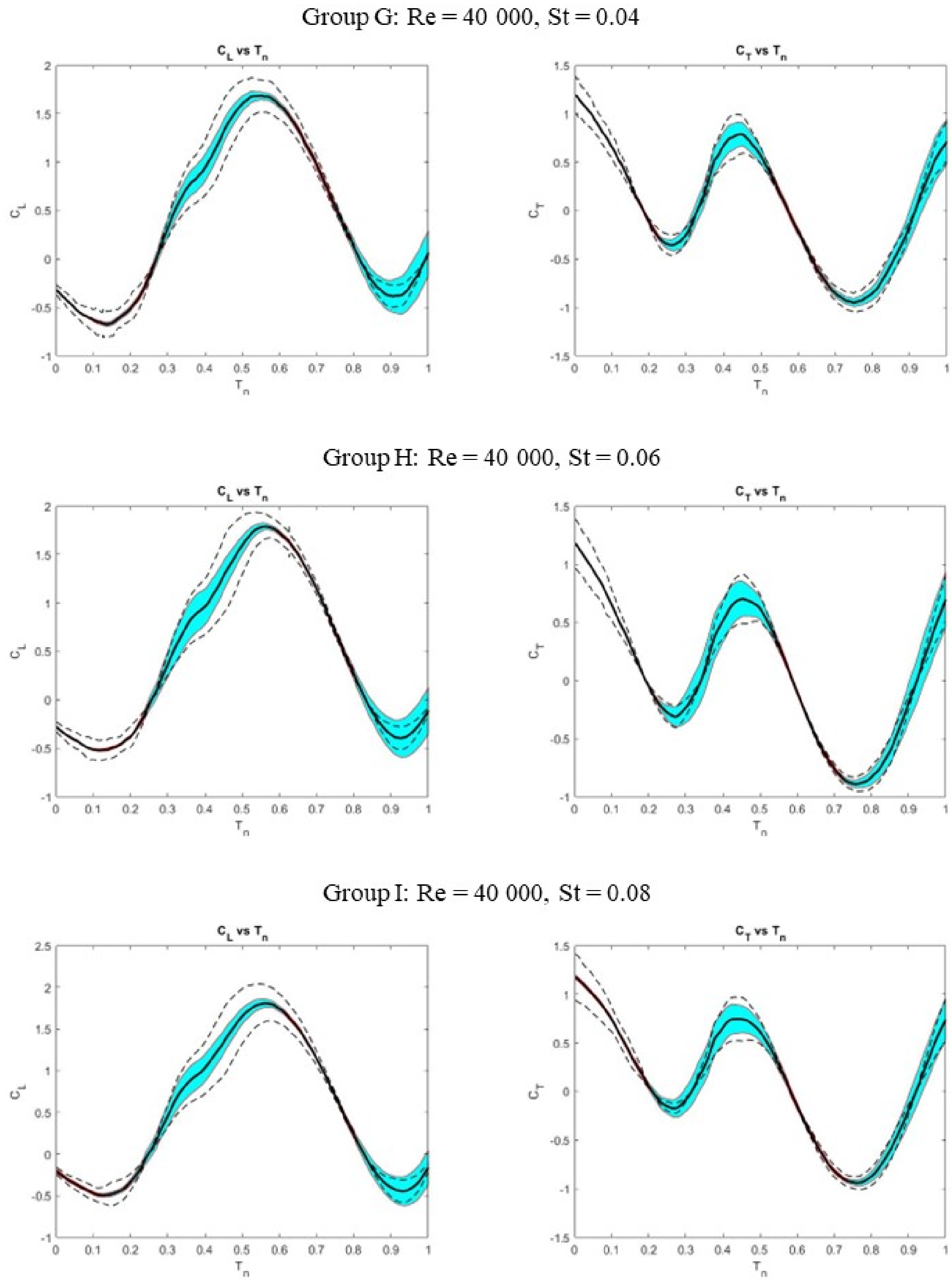

Fig. 3.10: C_L and C_T variation of groups G,H,I

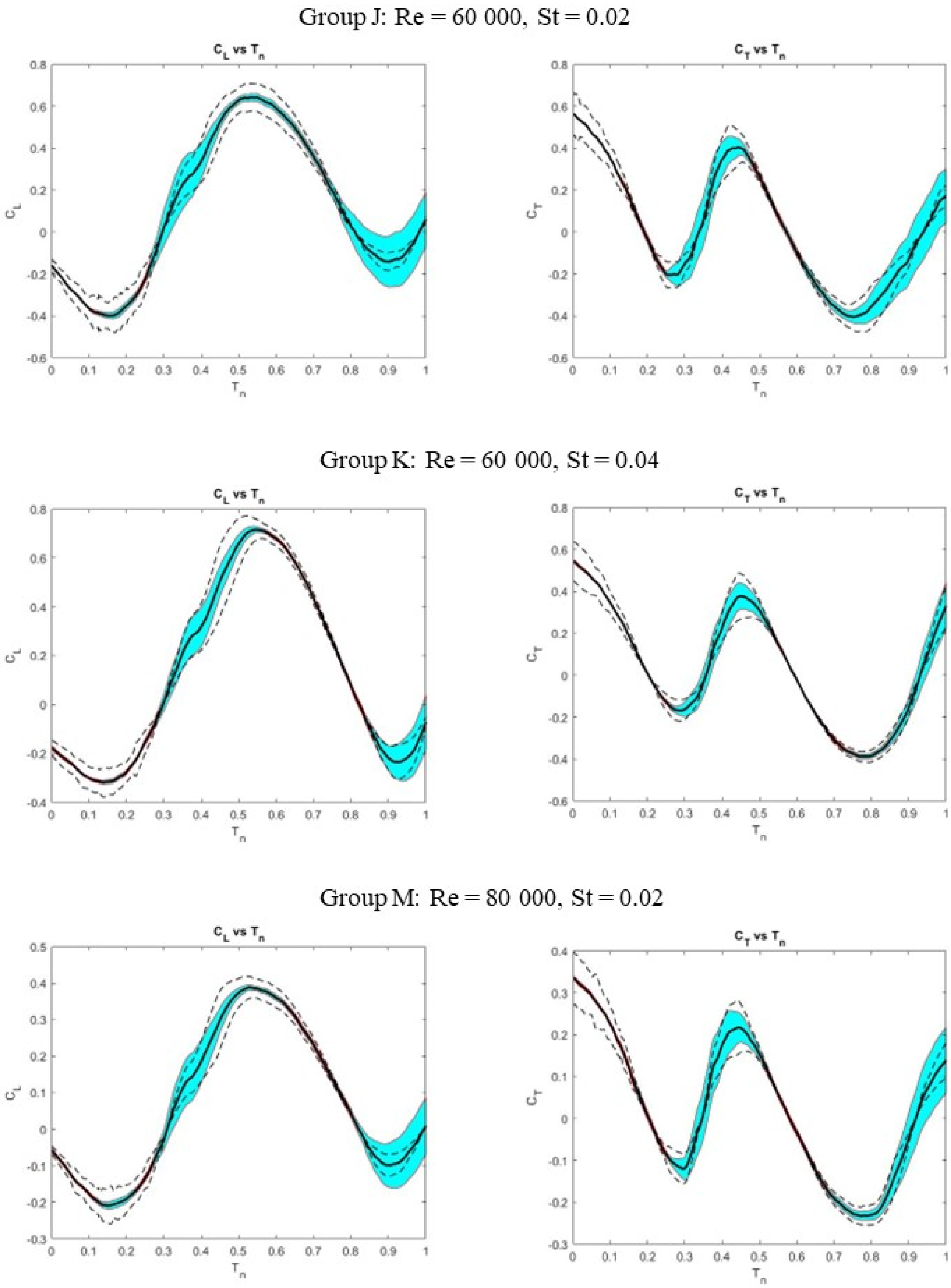

Fig. 3.11: C_L and C_T variation of groups J,K,M

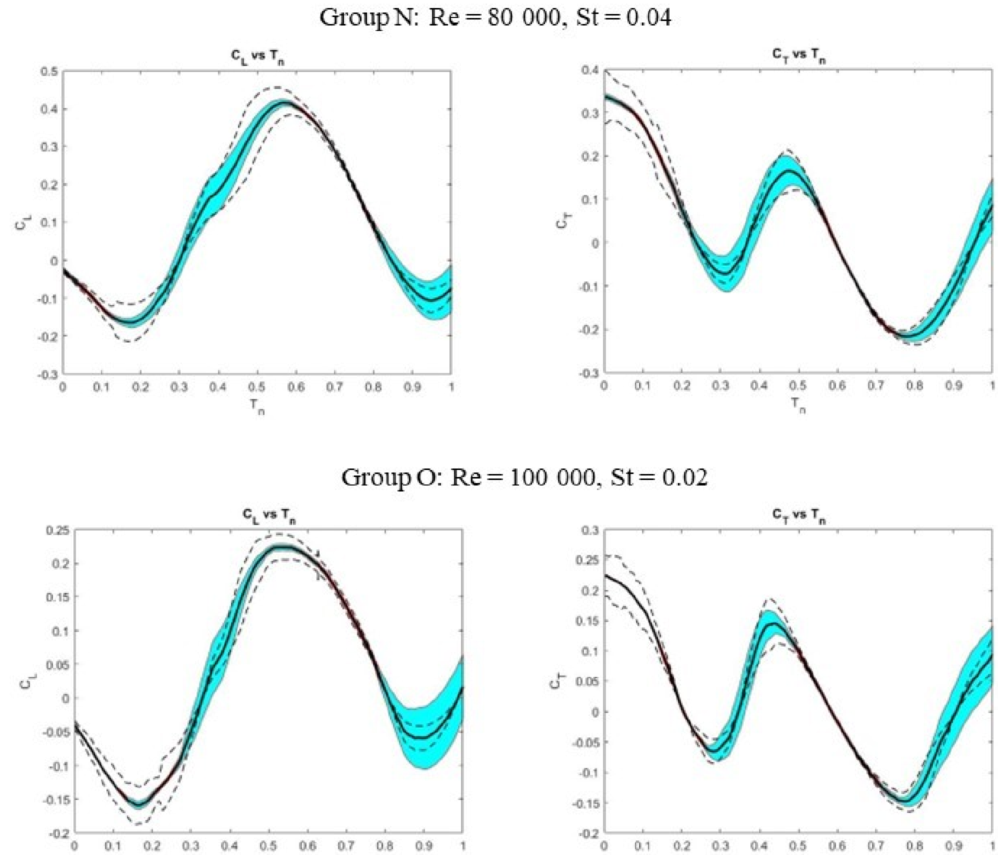

Fig. 3.12: C_L and C_T variation of groups N,O

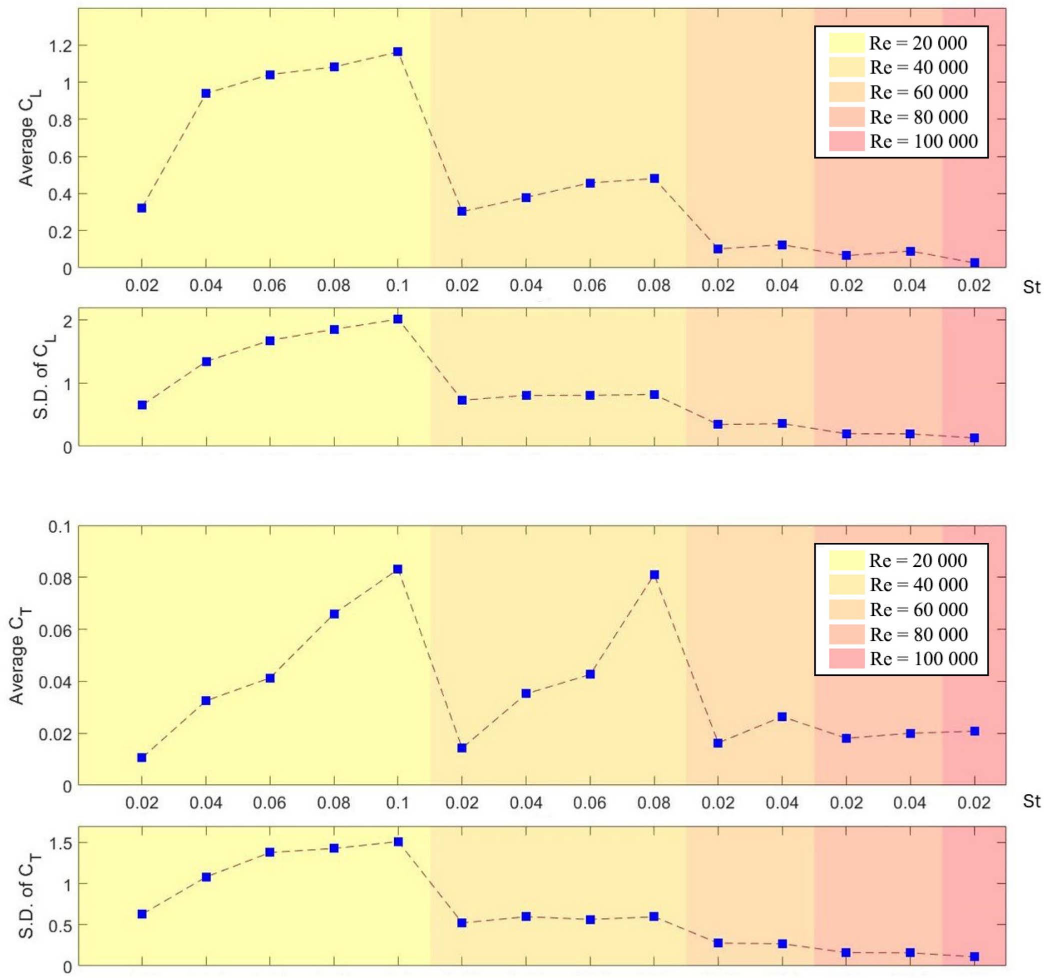

Fig. 3.13: Mean C_L and C_T of the test groups and corresponding standard deviation values.

3.4.2 Implications of the results toward the development of FWBAVs

The ability of a FWBAV to change altitude, direction, and forward flight speed is vital for performing aerial tasks. Birds are observed to accomplish these tasks with ease and efficiency. Modern rotary wing UAVs have become so versatile in applications because of their agility and stability. To outperform modern UAVs, FWBAVs must perform better in these areas. The mean C_L and C_T values in a wing motion cycle determine the ability to gain altitude and forward flight speed of a FWBAV. As illustrated in Fig. 3.13, in each Re, the mean values of C_L increase with increasing values of St . In each Re, the mean C_T values decrease with increasing St values. Identification of such trends is of vital importance in the design and development of FWBAVs.

Due to the unsteadiness of aerodynamic forces on a flapping wing, a FWBAV would experience undesired perturbations in accelerations during flight. Such behaviors have previously been observed in the developments of FWBAVs [14, 16]. Minimizing fluctuations in aerodynamic forces within a wing motion cycle would improve the stability of flight in FWBAVs. Flight stability is paramount in achieving objectives such as level flight and object tracking. Standard deviation values of the transient force measurements were calculated to quantify the fluctuations in test groups. As illustrated, the standard deviation values increase with increasing St and decreasing Re for both C_L and C_T values. This indicates that stability of a FWBAV using a similar wing kinematic would decrease with increasing Re and would increase with increasing St .

Considering both mean and standard deviation values, the best ranges of Re and St values can be selected for a FWBAV flight phase depending on its objective. When aiming for maximum elevation gain, Low Re value of 20 000 would be suitable since they provide high C_L magnitudes. However, the corresponding standard deviation values are also the highest recorded which indicates a reduction in elevation gaining stability in Re 20 000 with increasing St values. To obtain maximum forward flight acceleration, Re value of 40 000 stands out as the most suitable choice. In Re 40 000, the C_T magnitudes are higher or equal with considerably low standard deviation values to that of Re 20 000.

CHAPTER 4

COMPUTATIONAL INVESTIGATION OF AERODYNAMICS OF BIOINSPIRED PITCHING AND PLUNGING WINGS

4.1 Overview

The aim of the computational investigation is to supplement the experimental investigation by generating additional data on pitching and plunging wing aerodynamics in varying kinematics. Due to technical limitations of the experimental apparatus, the achievable wing pitching and plunging frequency was limited. Even though the experimental investigation was comprehensive enough to investigate the majority of the bird wing kinematic range as illustrated in 3.1, identification of the trends in lift and thrust performance in pitching and plunging wings would benefit from investigating the rest of the kinematic range. In order to reinforce the identified trends in various Re and St values beyonds the experimental findings, the region with the same Re and St values that's not used by any observed bird species are also investigated using the computational method. This region as shown in Fig. 4.1 also include some combinations of Re and St values that are not included in the experimental investigation due to technical limitations of the apparatus. Moreover, the computational investigation aims to offer additional insights into pressure, velocity variations and flow characteristcis.

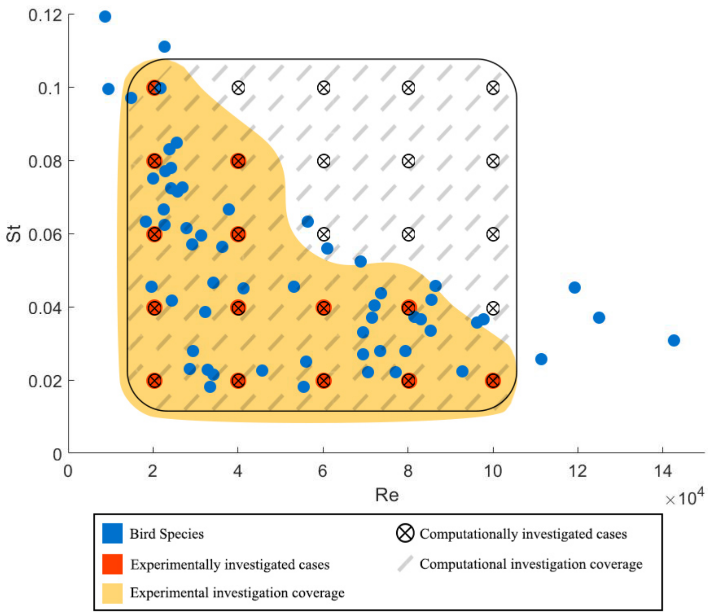

Fig. 4.1: St and Re distribution of forward flapping flight of the birds with coverage of experimental and computational investigations indicated

Since the experimental investigation considers only pitching and plunging motions of the wing, restricting any spanwise motion, the computational analysis can be conducted in a two-dimensional (2D) domain using a transient simulation setup. The primary advantage of a 2D simulation lies in its comparatively lower computational cost. This is attributed to the significantly smaller number of mesh cells, which in turn reduces the memory and processing power required for computation. With fewer elements to solve, the simulation achieves convergence more efficiently, requiring fewer iterations per time step. However, certain limitations are inherent in using a 2D simulation. Given the three-dimensional (3D) nature of turbulent eddy structures and vortices, a 2D approach cannot accurately capture these complex flow characteristics. Additionally, a 2D simulation does not account for spanwise flow effects, thereby limiting insights into their influence on the aerodynamic force generation of a pitching and plunging wing [75] . Despite these limitations, the decision to employ a 2D transient simulation was made due to constraints on computational resources and the primary objective of the computational study is to supplement the findings of the experimental investigation.

4.2 Overview of Ansys fluent CFD software

The commercial CFD software Ansys flunet uses a Finite-Volume Method (FVM) based calculation progress to compute solutions for flow parameters like pressure, temperature and velocity. The fundamental of the calculation progress is based upon converting the Navier-Stokes transport equations into a matrix form, which can be solved using an iterative method involving a collection of numerical methods to minimize the errors. To accommodate different dynamic fluid scenarios, Ansys Fluent contains different solvers and turbulence modeling solutions. Selection of these solvers and turbulent models along with all other settings within the software tool should be done with sound arguments based on knowledge about the flow physics of the simulated application.

4.2.1 Solver

Ansys Fluent offers two main solvers options: one pressure-based and another density-based, providing two distinct approaches to solve the governing equations toward an approximate solution. The pressure-based solver is further categorized into segregated and coupled methods, depending on the algorithm of computation used to solve for momentum and pressure. These approaches are summarized in the following flow chart.

Pressure based coupled solver is more suitable for low Re complex flow scenarios including moving geometrical components. Since they solve momentum and pressure

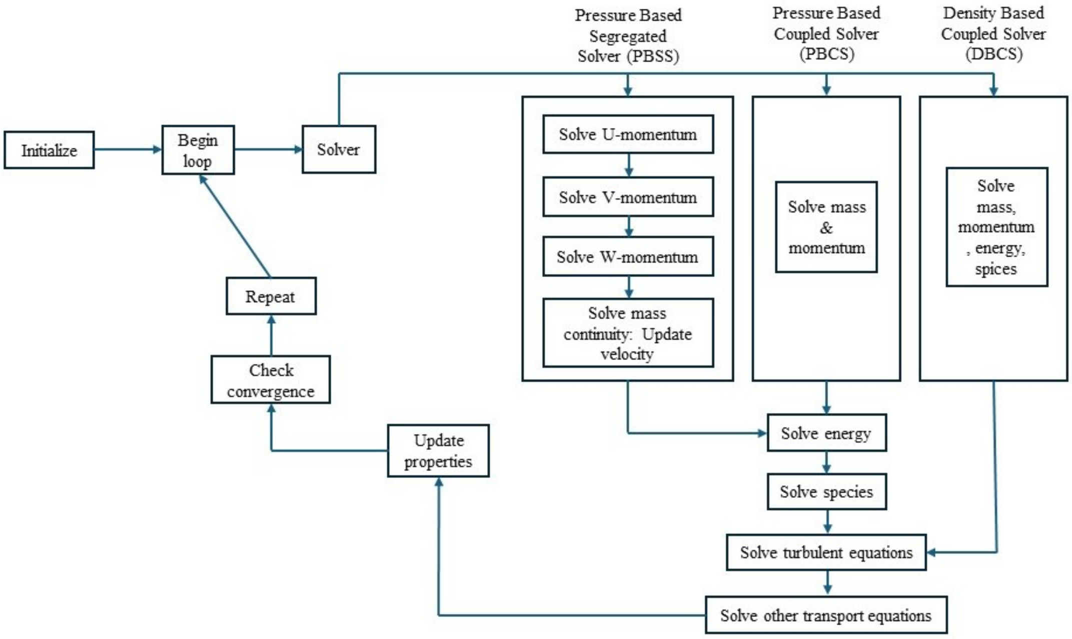

Fig. 4.2: Flow of information within the different solver types in Ansys fluent

equations simultaneously, the algorithm allows for more accurate representation of the physics of the flow compared to the segregated solver. For these reasons, the pressure based solver was selected for the use of this investigation.

4.2.2 Turbulence modeling

Multiple turbulence modeling options are available in Ansys fluent, majority of them are based on the Reynold Averged Navier-Stokes (RANS) turbulence modeling criteria. RANS is a reduced form of Navier-Stokes equations with steady-state solution decoupled from time varying fluctuation in the system [76]. The modeling method of these time varying fluctions are different in each turbulence model giving them particular limitations and advantageous in various flow regimes are mention in Table 4.1.

Transition SST turbulence model is selected for this investigation based on it's proven accuracy in complex aerodynamic flow conditions. This four-equation RANS turbulence model was originally developed by F.R. Menter and R. Langtry [77, 78]. The Transition SST model is well-suited for laminar to transitional flow scenarios with Reynolds numbers on the order of 1×10^5, particularly in aerodynamics and turbomachinery applications [79]. This is due to the improvements made in computing the production and dissipation of turbulence kinematic enegry and specific dissipation rate of turbulence. Limitations of earlier models like "k-ω SST" turbulence models were removed by introducing turbulence intermittency terms and a modified blending function to improve turbulence modeling near wall regions [80].

TABLE 4.1: Turbulence model available for RANS solvers in Ansys fluent

Turbulence model	Description	Suitable applications
Spalart-Allmaras	one-equation turbulence model for kinematic eddy turbulent viscosity	Offers robustness and efficiency in simulating attached and moderately separated flows, Initially developed low Reflow and suits aerodynamic applications, Not suitable for general industrial flows. [81]
k-ϵ	one of the simplest and most widely used RANS turbulence models. It assumes isotropic turbulence and employs two transport equations: one for turbulent kinetic energy (k) and the other for its dissipation rate (ϵ)	Developed specifically for planar shear layers and recirculating flow, performs well for a wide range of turbulent flows but may struggle in complex flow situations. [82]
k-ω	Offers corrections for low Reynolds number and shear flows, accounts for viscous heating, and requires minimal memory resources. Use two partially differential equations to solve for turbulence kinetic energy (k) and specific rate of dissipation (ω)	Accurate for attached boundary layers, backward-facing steps, and mildly separated incompressible flows. [83, 84]
Transition k-kl-ω	Modified k-ω turbulent model with addition of another equation solving for kL, where L is an integral length scale of turbulence and k is the turbulent kinetic energy	Provides qualitatively correct transition behavior for a wide range of flow conditions including freestream turbulence, pressure gradient, and surface curvature on the turbulence development.[78, 85]
Transition Shear Stress Transport (SST) [gamma-Retheta-SST]	Combines the benefits of the k-ω and k-ϵ models. It uses the k-ω model near the wall to resolve the boundary layer accurately and the k-ϵ model away from the wall to handle adverse pressure gradient flows	Provide significant improvement for all flows involving adverse pressure gradients and suitable for wide range of aerodynamic applications, Accurately predict pressure-induced separation and the resulting viscous-inviscid interaction. [77, 86, 87]

4.2.3 Governing Equations

As mentioned previously, Ansys fluent employs the finite-volume method (FVM) to compute flow parameters. The core computational process involves discretizing the Navier-Stokes equations into a matrix form, which is then solved iteratively using a combination of numerical techniques to minimize errors and ensure solution convergence.

The Navier-Stokes equations describes how density, pressure, velocity and temperature of a moving fluid are related using mass, momentum, and energy conservation equations as given in Equations 4.1 to 4.3 [80, 88]. With a finite volume method CFD calculation algorithm, the conservation equations are condensed into the form of transport equations which can used to model the movement and conservation of properties like momentum, energy and mass in a common equation format. Transport equations are also used to calculate the distribution of parameters like pressure, temperature, velocity and turbulence kinetic energy within the discritized fluid domain. The transport equation for velocity vector in partial differential form is provided in Equation 4.4. Using processes and assumptions of finite volume method, this equation can be converted into linearized matrix form as shown in Equation 4.5 [89]. During the convertion process, some decisions regarding the discretization method used to calculate the cell face values from the cell centeroid values should be taken [75, 90].

$$\frac{\partial \rho}{\partial t} + \nabla.(\rho U) = 0 \text{ ; Continuity equation} \tag{4.1}$$

$$\frac{\partial U}{\partial t} + \nabla.(\rho \nu U) = -\frac{\partial P}{\partial x} + \sum_{i=x,y,z} \frac{\partial \tau_{ii}}{\partial i} + \rho f_x \text{ ; Momentum equation for U,V,W} \tag{4.2}$$

$$\begin{aligned}\frac{\partial}{\partial t}[\rho(e + \frac{V^2}{2})] + \nabla.[\rho(e + \frac{V^2}{2})\boldsymbol{V}] = \rho \dot{q} + \sum_{i=x,y,z} \frac{\partial}{\partial i}(k_T \frac{\partial T}{\partial i}) + \sum_{i=x,y,z} \frac{\partial (u_i P)}{\partial i} \\ + \sum_{i=x,y,z} \frac{\partial (u_i \tau_{ij})}{\partial i} + \rho f.\boldsymbol{V} \text{ ; Energy equation}\end{aligned} \tag{4.3}$$

$$\begin{aligned}\underbrace{\frac{\partial (\rho U)}{\partial t}}_{\text{Temporal derivative}} + \underbrace{\nabla.(\rho U U)}_{\text{Convection term}} = \underbrace{-\nabla P}_{\text{Pressure(internal force)}} + \underbrace{\nabla.(\mu(\nabla U + \nabla U^T))}_{\text{Diffusion term}} \\ + \underbrace{-\frac{2}{3}\mu(\nabla.U)I}_{\text{Friction(internal force)}} + \underbrace{\rho g}_{\text{Gravity(external force)}}\end{aligned} \tag{4.4}$$

$$\underbrace{M}_{\text{Coefficient matrix}} \underbrace{U}_{\text{Velocity vector}} = \underbrace{B}_{\text{Right-hand side term}} \tag{4.5}$$

As pressure-based coupled solver is selected for this investigation, the linearized matrix form of the transport equations are solved to compute the parameter vector using a particular configuration of equations. The coupled algorithm uses a implicit treatment of the pressure gradient in the momentum equation by combining the three momentum equations, and pressure or pressure correction equation into a single matrix equation that is solved iterataively [91].

Turbulence computations using the transition SST model account for parameters including turbulence kinematic energy (k) and specific dissipation rate of turbulence (ω) through solving a seperate collection of transport equations as given in Equation 4.6. P_k and D_k terms accounts for production and dissipation of k or ω and they are controlled through a improved blending function (F_1) to improve accuracy of modeling in near wall regions [87, 92].

$$\frac{\partial(\rho k)}{\partial t} + \nabla.(\rho U k) = \nabla.((\mu + \frac{\mu_k}{\sigma_k})\nabla k) + P_k - D_k \tag{4.6}$$

ρ	Fluid density
U	Velocity
ν	Kinematic viscosity
P	Pressure
τ	Shear stress
f_x	External force
e	Specific Internal Energy
$\boldsymbol{V}$	Velocity vector field
$\dot{q}$	Energy generation per unit volume
k_T	Thermal conductivity
T	Temperature
f	Body force per unit mass
μ	Dynamic viscosity
I	Identity matrix
g	Gravitational acceleration

μ_k	Turbulent eddy viscosity
σ_k	Turbulent Prandtl number for k

4.3 Methodology

Simulations to investigate the aerodynamics of pitching and plunging wings will be conducted in a two-dimensional domain. Since the experimental investigation also maintained a uniform cross-sectional shape and motion in the spanwise direction, two-dimensional CFD simulations are appropriate. Additionally, this approach reduces the computational cost of the investigation. Table 4.3 illustrate all the combinations of Re and St values. In addition to all the test groups addressed in the experimental investigation, eleven test groups beyond the capabilities of the experimental apparatus are investigated.

4.3.1 Pilot simulation

The CFD simulation process started with the pilot simulation. The primary objective of the pilot simulation was to successfully carry out a transient simulation of pitching and plunging wings. The kinematic and fluid flow input values were selected referring to the numerical investigation by Young and Lai [63]. All the input values and boundary conditions are mentioned below.

The domain for the simulation was defined so that the development and propagation of the wake could be observed. The domain size was kept minimum to reduce the number of mesh elements which would increase the computation cost of the simulation. The definition of domain was followed by the mesh generation process. Several key decisions needed to be made on the quality of the mesh which subsequently influence the quality and accuracy of the simulation results. Special attention needs to be given to the mesh element size, quality, and shape in each region of the domain. In order to accommodate wing motion in the simulation, the "Dynamic Mesh Motion" tool of ANSYS fluent was used. Therefore, the mesh was developed accordingly. Discussions available at the "www.cfd-online.com" website were useful as guidelines in mesh development [93]. Due to the mechanism of "Dynamic Mesh Motion", triangular mesh elements were favored over structured quadrilateral mesh elements. The gradual increment of mesh size from the wing boundary to the domain boundary which is called "mesh stiffness" is extremely important in avoiding "negative mesh element area errors". Also, the maximum mesh element size near the wing boundary should be smaller than the amount of distance the wing moves at its maximum velocity in a time step. To avoid this error, the time step size needs to be fine-tuned iteratively. The time step value used in the successful simulation was 0.001 of the periodic time of the flapping cycle.

TABLE 4.2: Parameters used in the pilot simulation

Wing chord length	100 mm
Reynolds number (Re)	1×10^5
Inlet flow velocity	$9.7\ ms^{-1}$
Strouhal number (St)	0.4
Plunge amplitude	50 mm
Pitch amplitude	15^o
Plunge and pitch frequency	77.3 Hz

TABLE 4.3: Division of the CFD simulation into groups with varying Reynolds and Strouhal number values

Re	St				
	0.02	0.04	0.06	0.08	0.1
20 000	Group A	Group B	Group C	Group D	Group E
40 000	Group F	Group G	Group H	Group I	Group P
60 000	Group J	Group K	Group L	Group Q	Group R
80 000	Group M	Group N	Group S	Group T	Group U
100 000	Group O	Group V	Group W	Group X	Group Y

Since the Dynamic Mesh feature was selected to accommodate the wing motion within the domain, an unstructured mesh with localized element sizes was employed [75]. The elements in the vicinity the airfoil boundary were the smallest while elements near the domain boundary were the largest, having a gradual increment of mesh element size from the airfoil to the domain boundary.

4.3.2 Geometry and mechanics of the wing

NACA 0012 airfoil with chord length of 100mm is used as the geometry, keeping consistent with the experimental investigation. The fluid domain was developed in accordance with the requirement brought forward by the "dynamic mesh" feature as illustrated in the Fig 4.2. Frequency of pitch and plunging motion frequency is calculated as required by the "CG motion" UDF used for the simulations. Additionally the pitch and plunge motion amplitudes are also included in the UDF. The wing motion profile is kept identical to the experimental investigation as illustrated in 3.2.

4.3.3 Mesh and time-step optimization

The mesh and time-step value used in the pilot simulation are only optimized to overcome errors generated during the simulation. Before continuing with the rest of the simulations in the investigation, the mesh and time-step values need to be optimized

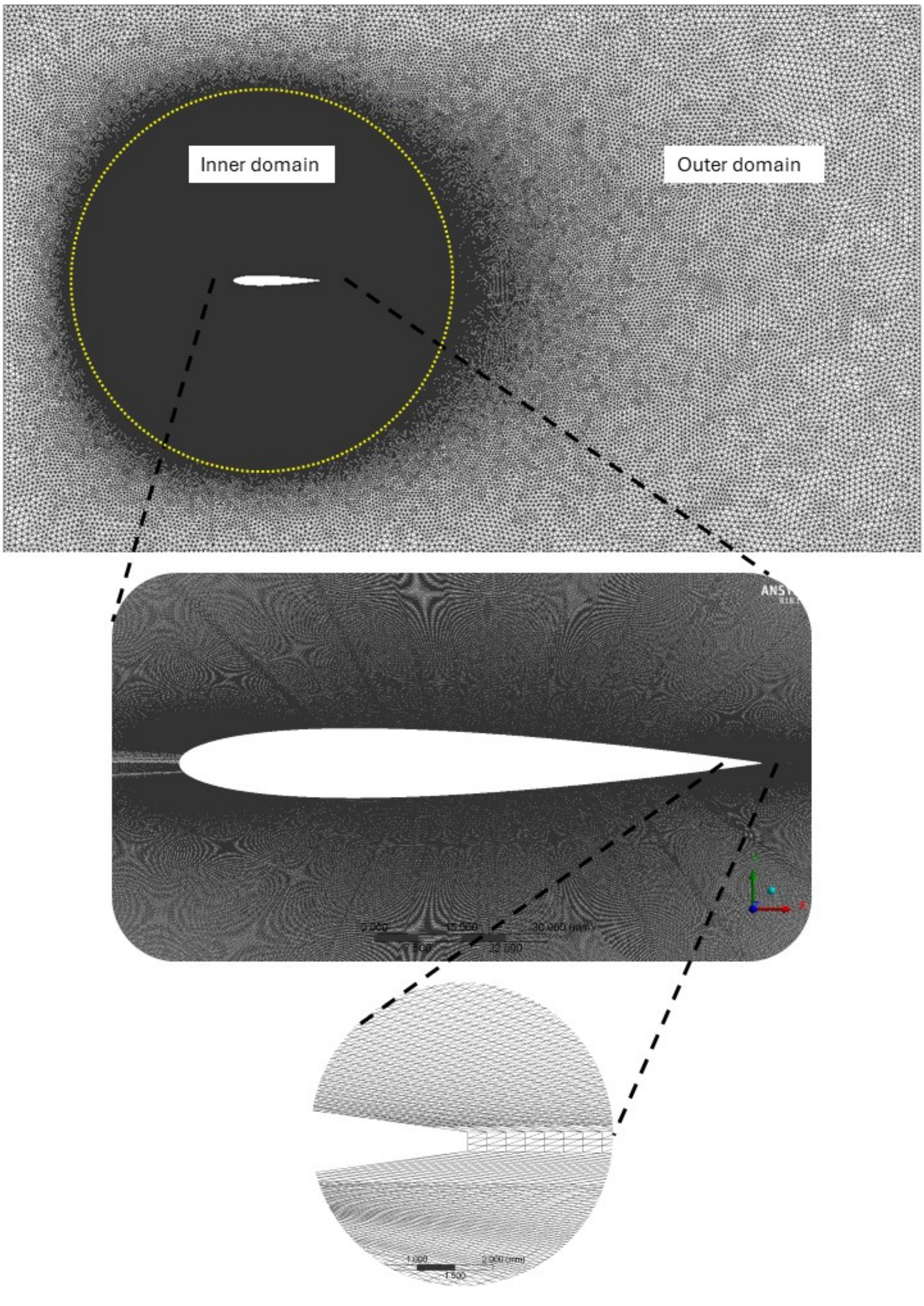

Fig. 4.3: Optimized mesh developed to accommodate "Dynamic Mesh"

TABLE 4.4: Information on the three mesh arrangements used for the optimization

Parameter	Mesh α	Mesh β	Mesh γ
Number of elements	4.6×10^5	1.5×10^6	2.9×10^5
Minimum element size (m)	1×10^{-5}	2×10^{-4}	5×10^{-4}
Maximum element size (m)	2.5×10^{-3}	5×10^{-3}	1×10^{-2}
Computational time taken per cycle (processor hours)	20	3.4	1.3

for maximum accuracy with minimum computational cost using convergence analysis method. Two mesh arrangements should be created, using the successful mesh from the pilot simulation as a baseline. One mesh should be less refined, while the other should be more refined in terms of mesh resolution. The results and computational cost in terms of processor hours should be taken into account when selecting the optimal choice from the three. If the selected mesh is newly developed, the process should be iterated with another mesh further along the same trend until a satisfactory mesh arrangement is achieved [94]. Similarly selected three time step values are used for the time-step optimization process.

It is expected to use the selected mesh and time step value of the optimization process for a series of investigative simulations. Mesh β was used in the pilot simulation. Mesh γ was developed with reduced resolution by increasing the minimum mesh element size to 0.002m (x2 compared to Mesh β). The drag and lift force results of the Mesh γ simulation showcase considerable deviation from the other two simulation, therefore Mesh γ was taken out of consideration. The deviation between the force results from Mesh α simulation and Mesh β simulation was observed to be insignificant, especially when considering the additional computational time taken for the Mesh α. Therefore, Mesh β was selected as the most suitable for the next series of simulations.

In the pilot simulation, the time step of $T_P/800$ simulation was used after optimizing to overcome the negative mesh volume error. T_P is the periodic time of the plunge motion function. In the time-step convergence analysis, time-step values of $T_P/800$ and $T_P/1200$ were used for the comparative analysis. $T_P/800$ simulation showcased large deviations of thrust and lift force values compared to the other time step values. $T_P/800$ simulation was also faced with "negative mesh volume" error after about 7000 time steps. Therefore, it was taken out of consideration. Drag and lift results of$T_P/1000$ and $T_P/1200$ simulations were observed to be similar in quantity and resolution. Considering the computational time taken for the two simulations $T_P/1000$ was selected as the most suitable time step value for the next series of simulations.

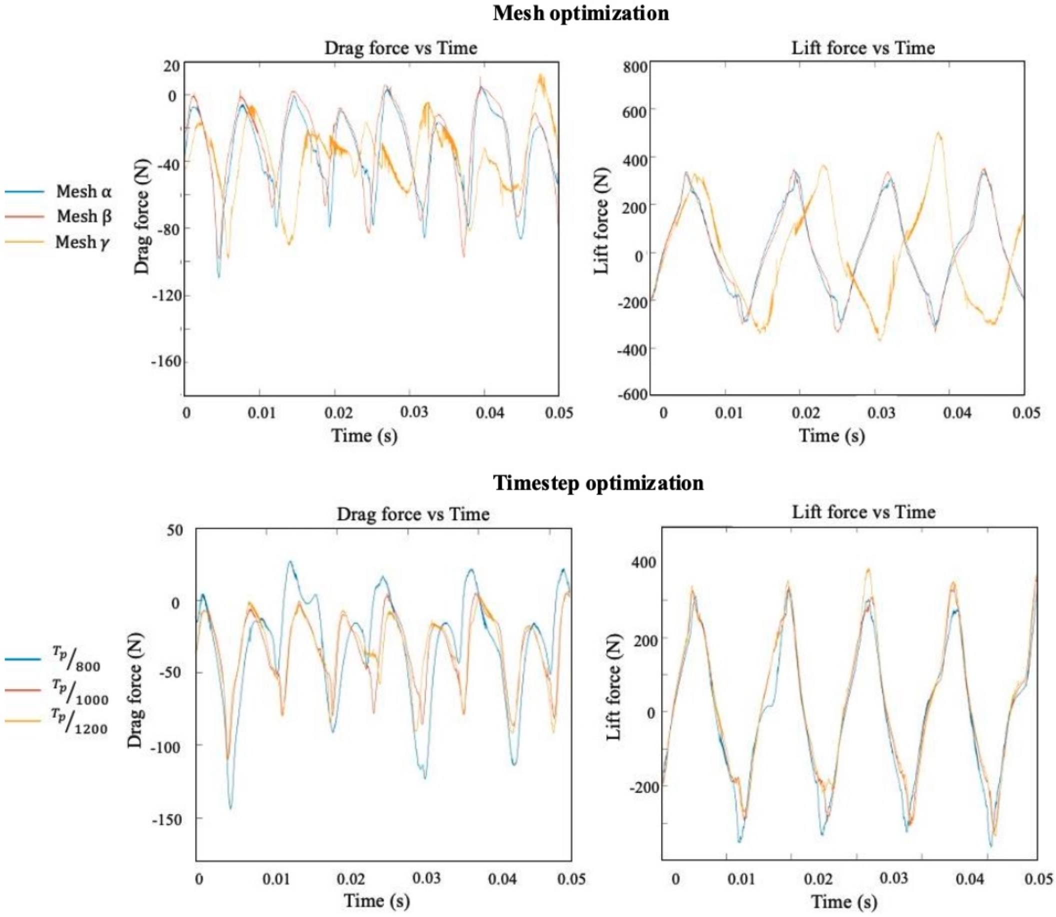

Fig. 4.4: Comparison of lift and drag force results in mesh and time-step convergence studies

4.3.4 Qualitative and quantitative validations

The simulation procedure was validated using both qualitative and quantitative comparisons. For the qualitative comparison, experimental results of Lai and Platzer were used [95]. The optimized mesh and time-step value are used with other settings kept identical to the pilot simulation. The rising plume wake structures created by the interaction of the counter-rotating vortices are visible in the velocity contour of the simulated wake as shown in Fig. 4.5. Vortices are shed in every half-cycle of the airfoil motion and they are subsequently carried downstream. Simulated wake also agrees with the detailed analysis done by Young and Lai [18] on the results of the investigation by Lai and Platzer [95].

For the quantitative validation, the experimental investigation by Kim et al. was recreated using the optimized mesh and time-step values [66]. The same investigation was used for the validation of the experimental method. In the original investigation, a NACA 0012 airfoil was subjected to pitching motion in varying reduced frequency values (K) and Re. In the test case used for the validation, Re is 4×10^4 and K is 0.1. Results from the original investigation with both experimental and computational results generated in this validation process are illustrated in Fig. 4.6.

Agreement between the computational results and Kim's results were quantified using average percentile deviation between the two data sets. Average percentile deviation values for lift and drag results are 7.1% and 13.7% respectively indicating a reasonable agreement.

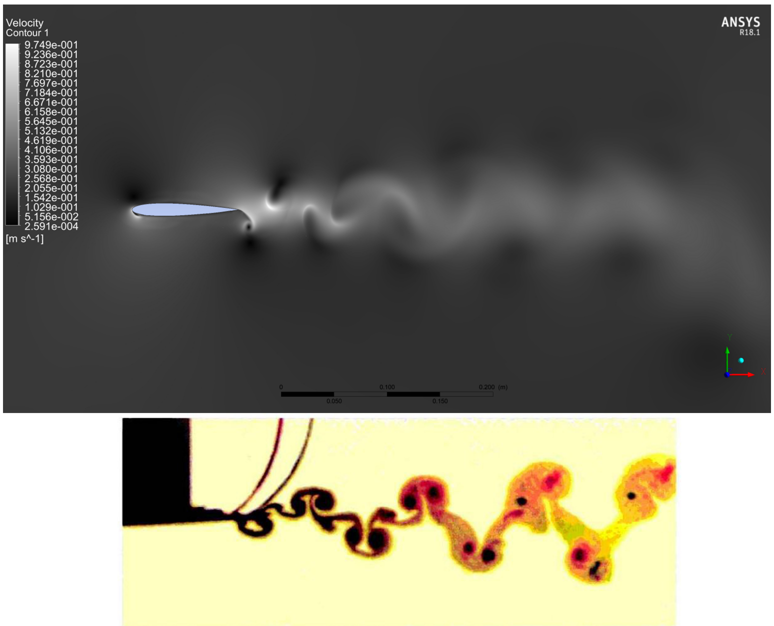

Fig. 4.5: Comparison between experimental results from Platzer and simulated wake

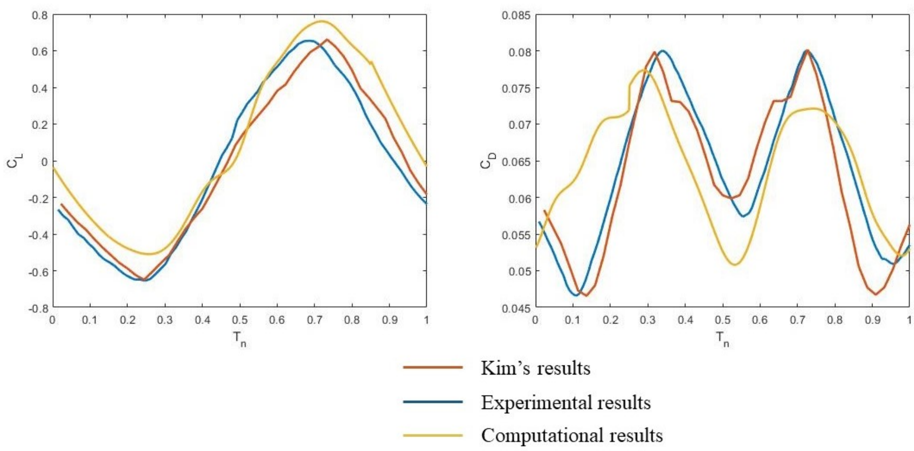

Fig. 4.6: Comparison between results from Kim's experimental investigation and experimental and computational results of this investigation

4.3.5 Investigative simulations

Following the pilot simulation, mesh and time-step optimization and validation processes, the simulation set-up for the series of investigative simulations is constructed based on the results of the previous steps. The domain is constructed to fullfil the requirements of the "Dynamic Mesh" tool that is used to move the "Inner domain" section containg the aerofoil. The dimensions of the domain used for the simulations are given in Fig. 4.7. The domain and mesh are same as the Mesh β as illustrated in Fig. 4.3.

The boundary conditions for the simulation set-up is a direct derivation of that of the successful pilot simulation. The inlet velocity is governed by the Re of the simulated scenarios as mentioned in Table 4.3. The outlet is defined as a pressure outlet with zero gauge pressure. The top and bottom boundaries of the mesh is defined as "Symmetrical" to remove any effects by those boundaries on the fluid flow around the moving aerofoil. The motion of the inner domain containing the aerofoil is governed by the "Dynamic Mesh" tool of Ansys Flunet and a User Defined Function (UDF) . An example UDF is given in Fig. 4.8 as an example.

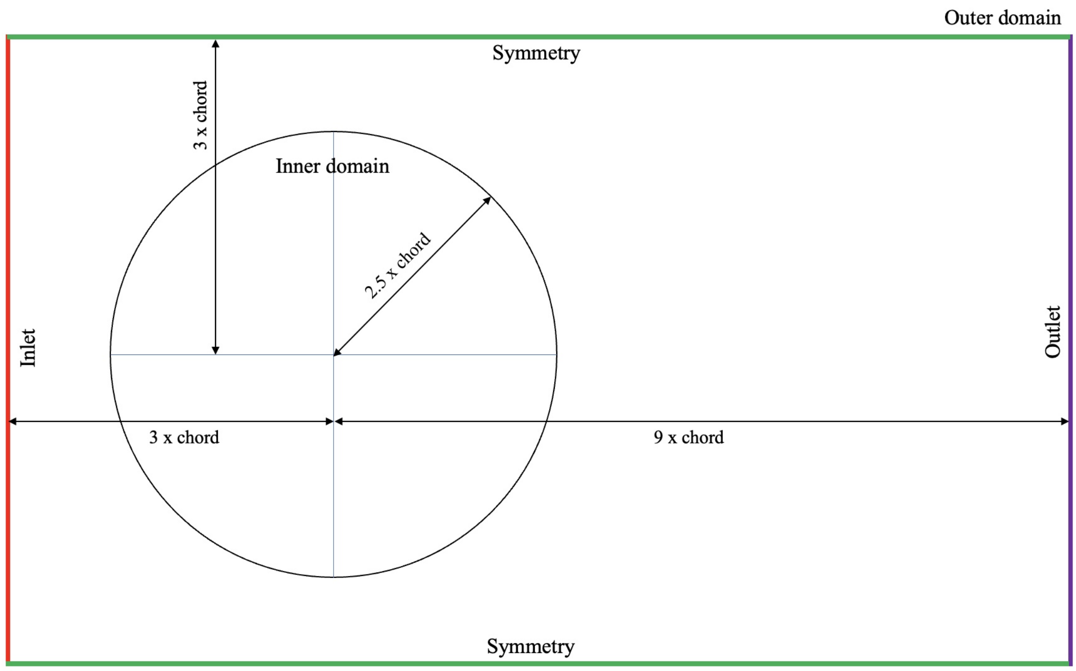

Fig. 4.7: Domain dimensions and boundary conditions (chord length = 100mm).

```
#include "udf.h"
#define angular_vel 4.8583
#define plunge_amplitude 0.5
#define pitch_amplitude 15*M_PI/180

DEFINE_CG_MOTION(shm, dt, cg_vel, cg_omega, time, dtime)
{
      double omega;

      double h =
plunge_amplitude*angular_vel*cos(angular_vel*time);
      omega = pitch_amplitude*angular_vel*cos(angular_vel*time);

      cg_vel[0]= 0.0;
      cg_vel[1]= h;
      cg_vel[2]= 0.0;

      cg_omega[0]= 0.0;
      cg_omega[1]= 0.0;
      cg_omega[2]= omega;

}
```

Fig. 4.8: User Define Function (UDF) example to govern the motion of the inner domain.

4.4 Results and discussion

The time history variations of lift and thrust coefficients, calculated from the results exported from the series of CFD simulations, are discussed alongside the velocity and pressure contour plot renderings. These results are analyzed independently and in comparison with the experimental findings obtained previously.

4.4.1 Key characteristics of transient results

All lift and thrust variations illustrate maximum and minimum values around stroke reversal. Lift coefficient fluctuations consistently peak near $0.5T_N$ and trough around T_N, while thrust coefficient variations also exhibit local peaks around stroke reversal at $0.5T_N$ and T_N, and local troughs at $0.25T_N$ and $0.75T_N$. However, thrust variations demonstrate greater diversity across different Re and St values compared to lift variations. The overall shape of the lift and thrust fluctuations have large similarities to the experimental results obtained. Figures 4.12 - 4.15 illustrate the lift and thrust variations in the test groups with varying Re and St values. The Revalues range from 20 000 to 100 000 while St values vary from 0.02 to 0.1 as mentioned in table 4.3.

Comparison of lift and thrust coefficients in groups with similar Re and St values reveal trends in aerodynamic force generation in pitching and plunging wings. In C_L

variations, the maximum value observed near $t = 0.5T_N$ increases gradually with increasing St values. This characteristic trend is common in all Re groups from 20 000 to 100 000. However, the deviation between of the maximum value between two consecutive St values is observed to be reducing with increasing Re values. Meaning in high Re values, the lift variations plots are packed closer together than in low Re value comparisons. In C_T variations, the two local minimum values showcased by every group around $t = 0.25T_N$ and $t = 0.75T_N$ gradually increase with increasing St values. This trend is more clearly visible around the second local minimum in all the groups and effects the mean C_T performance in a positive manner.

To delve deeper into the fluid mechanisms driving the observed variations in lift and thrust of a plunging and pitching airfoil, velocity and pressure contour plots of the fluid flow were generated, as depicted in Figures 4.9, 4.10 and 4.11. Fluctuations of the velocity contours around the moving wing are analysed for a periodic time of wing motion (T_N). At the instance when $t = 0$, the airfoil is at the peak of its plunging motion. Stagnation of velocity is noticeable at the top of the Leading Edge (LE), accompanied by an increase in velocity magnitude at the bottom of the LE. Additionally, a low-velocity region is observed at the bottom of the Trailing Edge (TE), which is indicative of the Trailing Edge Vortex (TEV). Thrust coefficient reaches it's first local minimum at $t = 0.27T_N$ which is close of zero pitch and plunge magnitude position happening at $t = 0.25T_N$. During this phase, the movement of the low-velocity area associated with the Leading Edge Vortex (LEV) is distinctly visible as it moves backward along the bottom surface of the wing. Concurrently, the lift coefficient undergoes a transition from negative to positive, primarily influenced by the variation in angle of attack due to the wing's pitching motion. The lift coefficient peaks at approximately 0.65 around $t = 0.47T_N$, closely preceding the stroke reversal at $t = 0.5T_N$, coinciding with a local maximum in thrust coefficient. The velocity contour plot depicts a pattern reminiscent of the $t = 0$ instance, with low-velocity regions near the bottom surface of the Leading Edge (LE) and the top surface of the Trailing Edge (TE), and high-velocity regions around the top surface near the LE. At $t = 0.72T_N$, the thrust coefficient reaches another local minimum value of -0.44. This occurs during the upstroke of the wing motion, around the instance of zero pitch and plunge magnitude position at $t = 0.75T_N$. In this instance, the low-velocity region on the top surface of the airfoil is gradually shedding toward the Trailing Edge (TE). The thrust coefficient reaches its overall maximum at $t = 0.96T_N$, near the stroke reversal. Similar observations to those made at $t = 0$ can also be made here to account for the increased thrust.

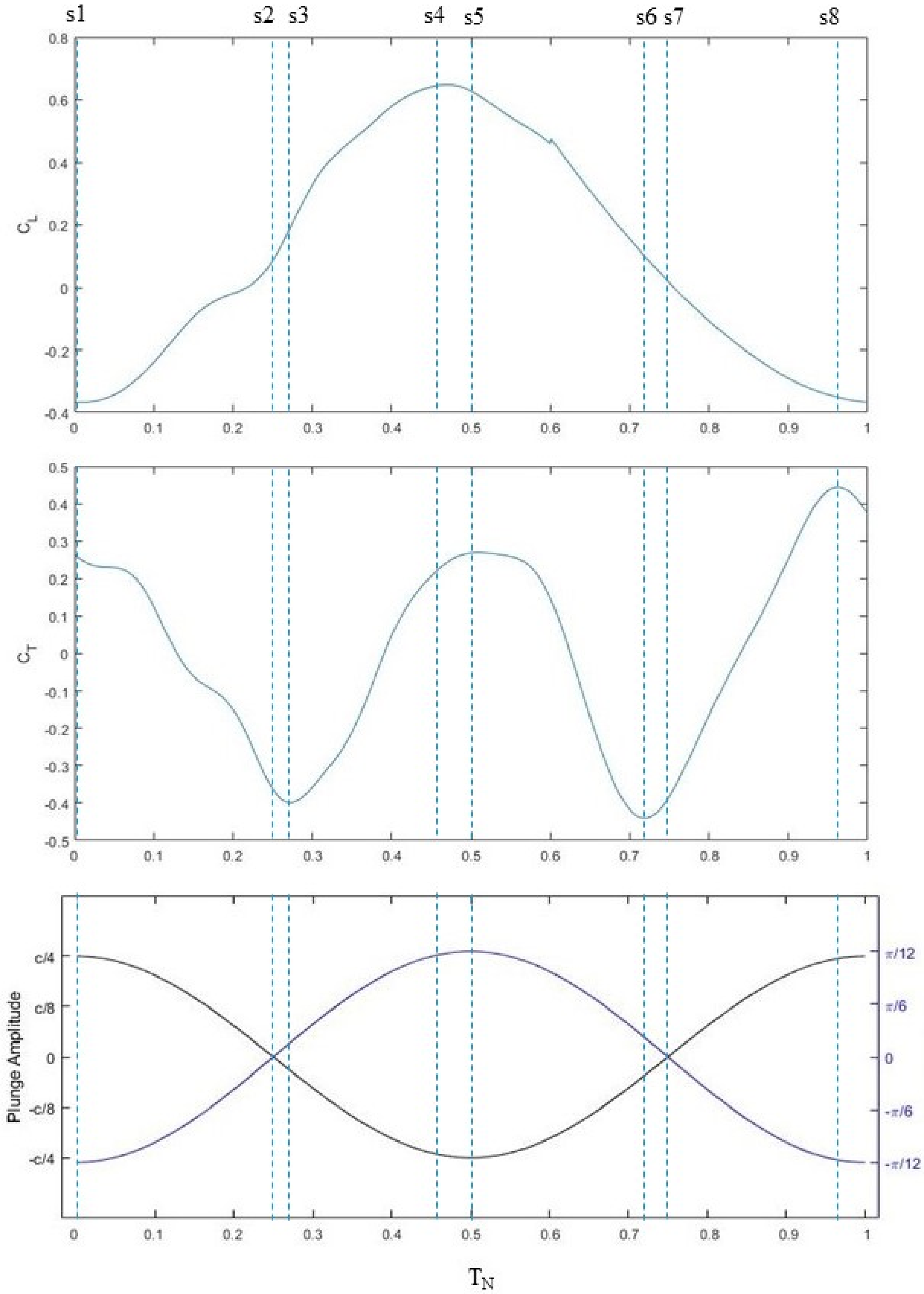

Fig. 4.9: Stacked plot graph of the lift and thrust coefficients and pitch and plunge magnitudes of group L with Re= 60 000 and St = 0.06

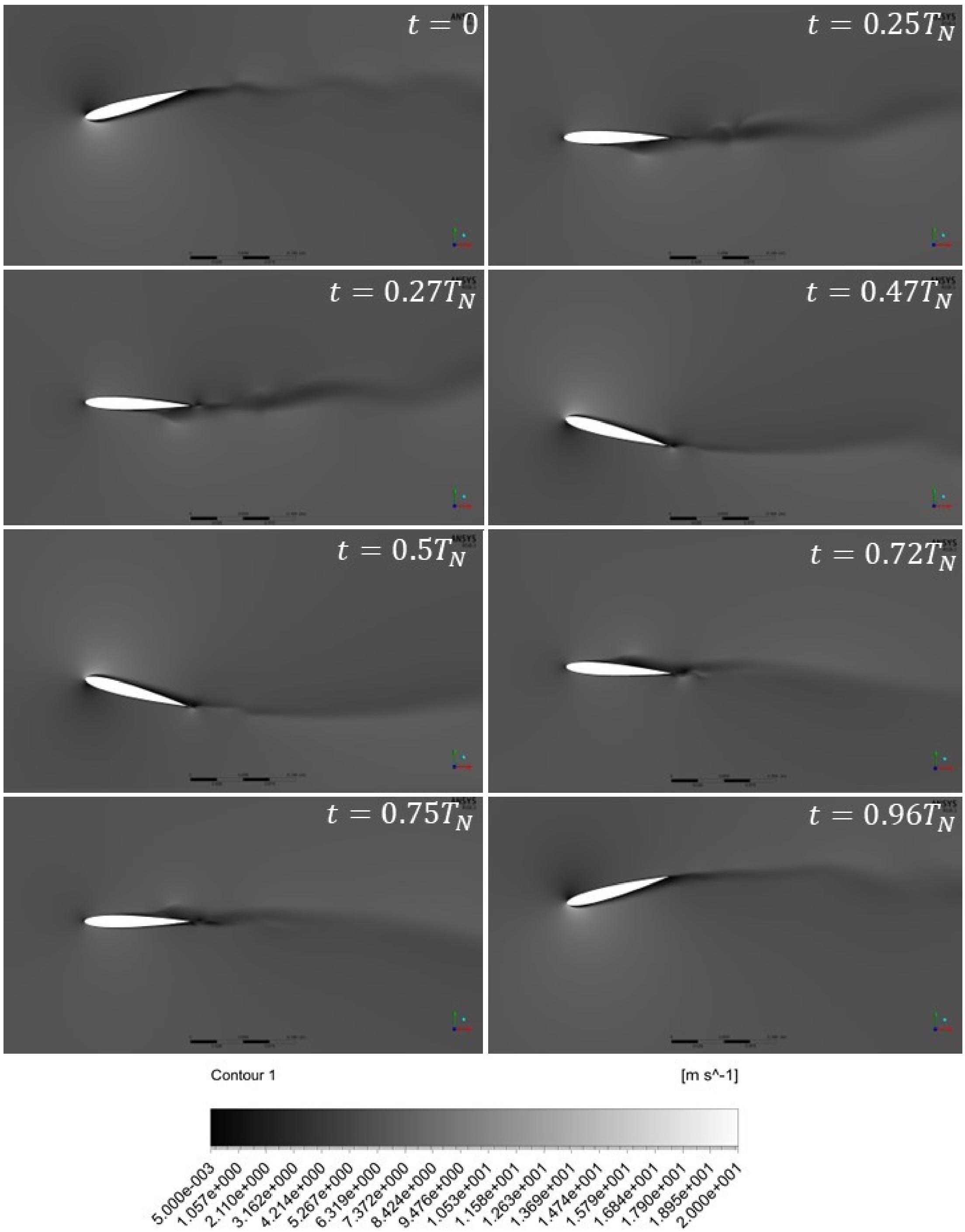

Fig. 4.10: Velocity contour plots in Greyscale of pitching and plunging wing of Group L with Re= 60 000 and St = 0.06

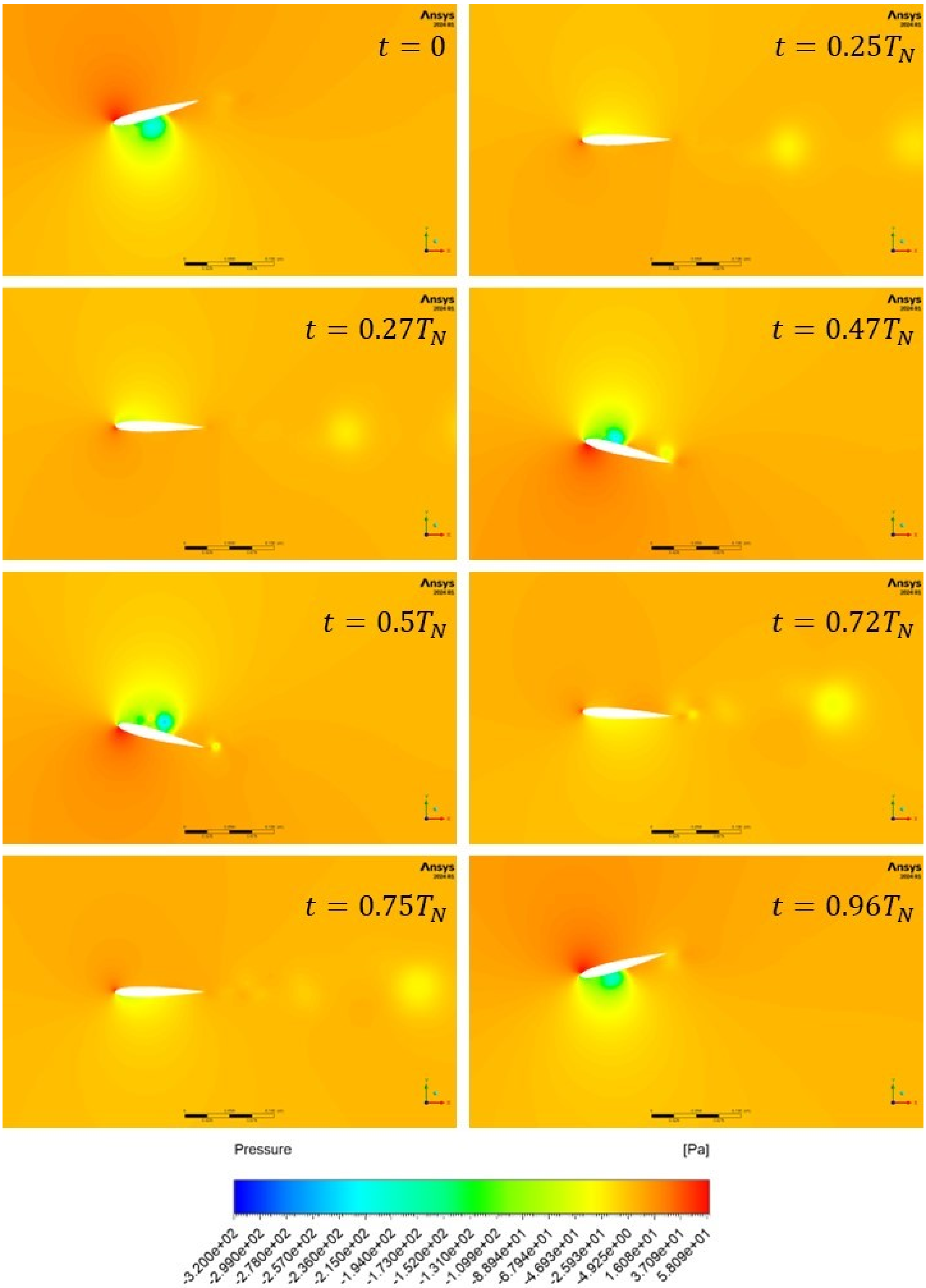

Fig. 4.11: Pressure contour plots of pitching and plunging wing of Group L with Re= 60 000 and St = 0.06

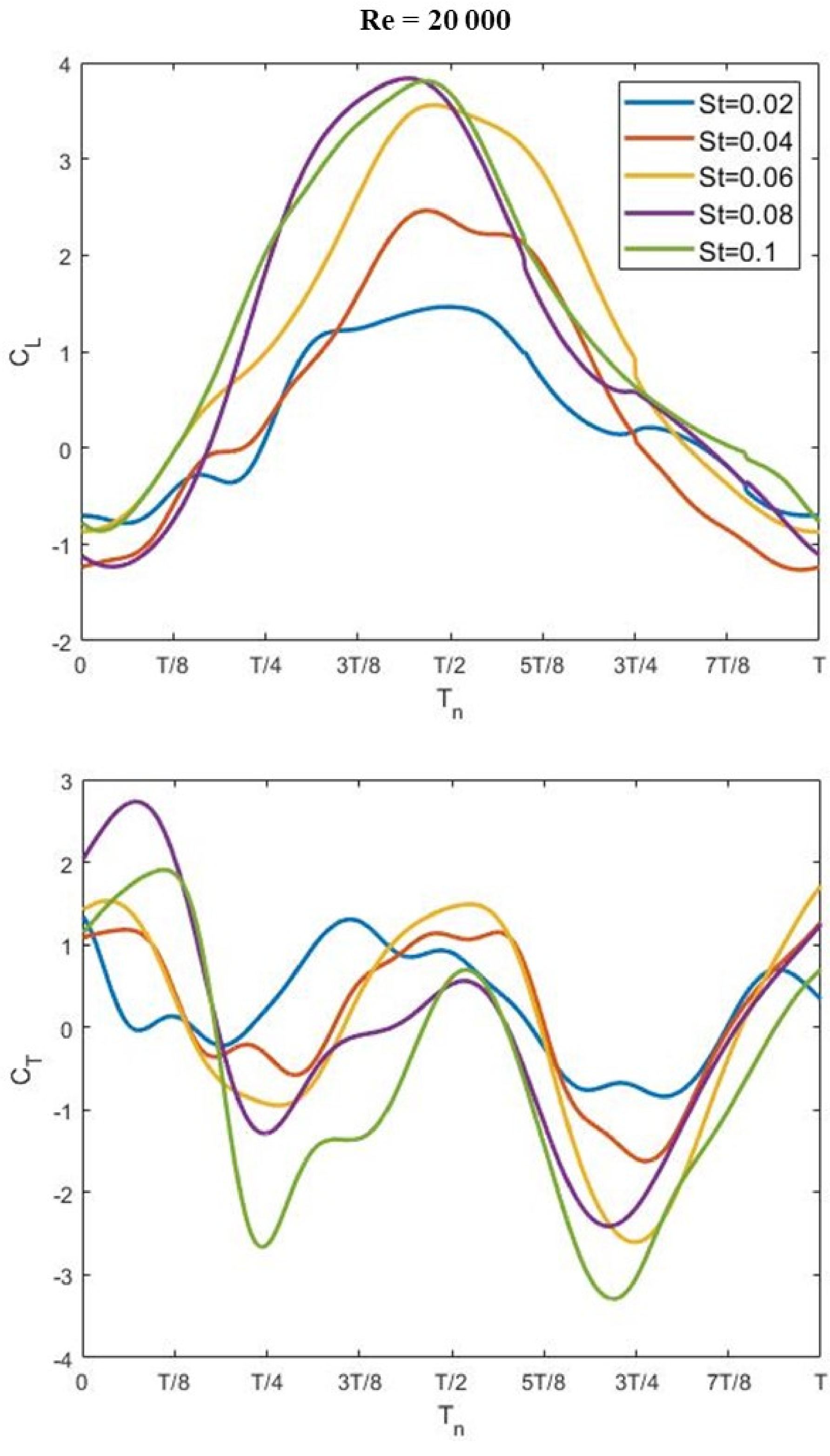

Fig. 4.12: Computational result of C_L and C_T variations of test groups with Re value of 20 000 with St values from 0.02 to 0.1

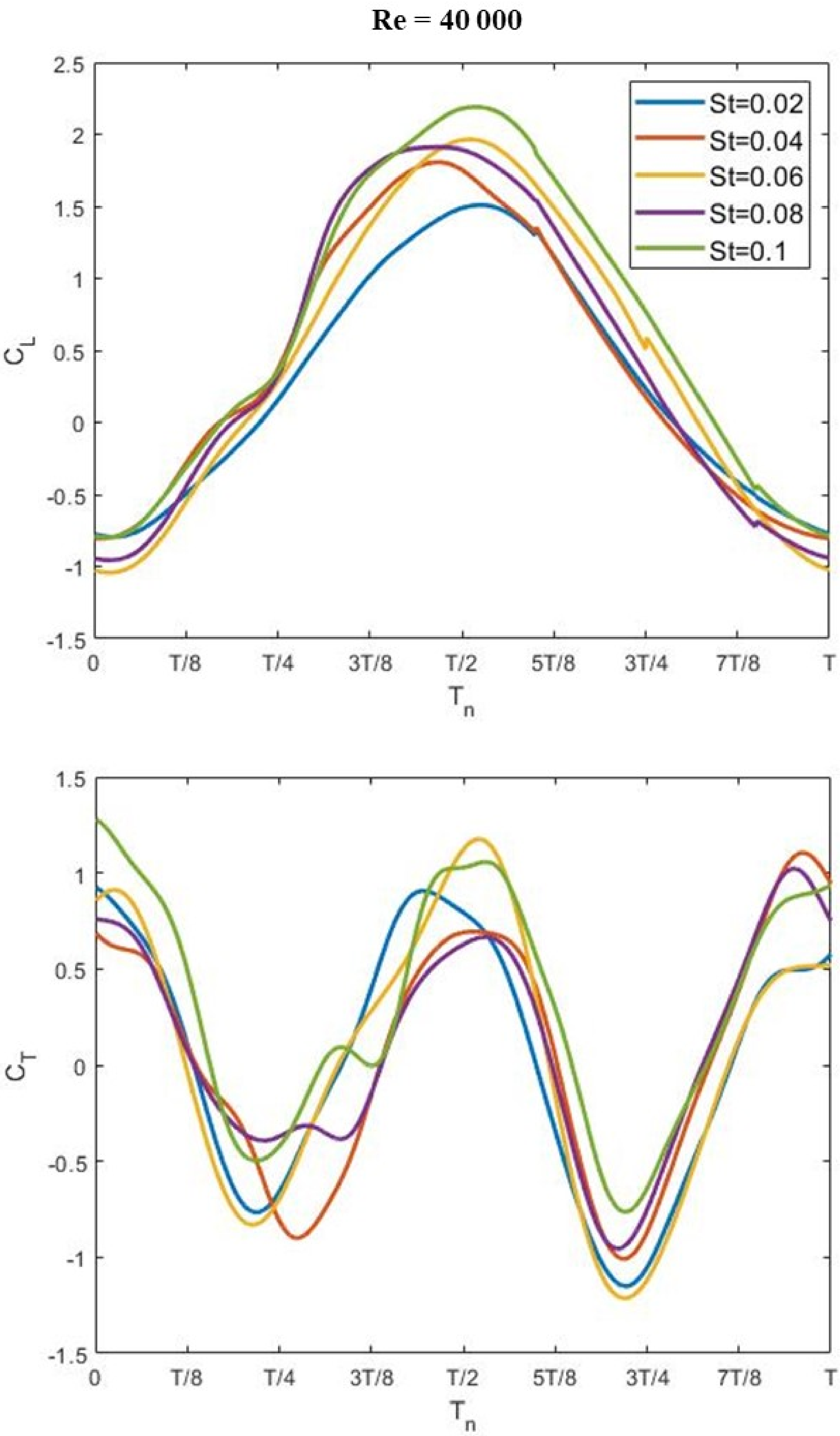

Fig. 4.13: Computational result of C_L and C_T variations of test groups with Re value of 40 000 with St values from 0.02 to 0.1

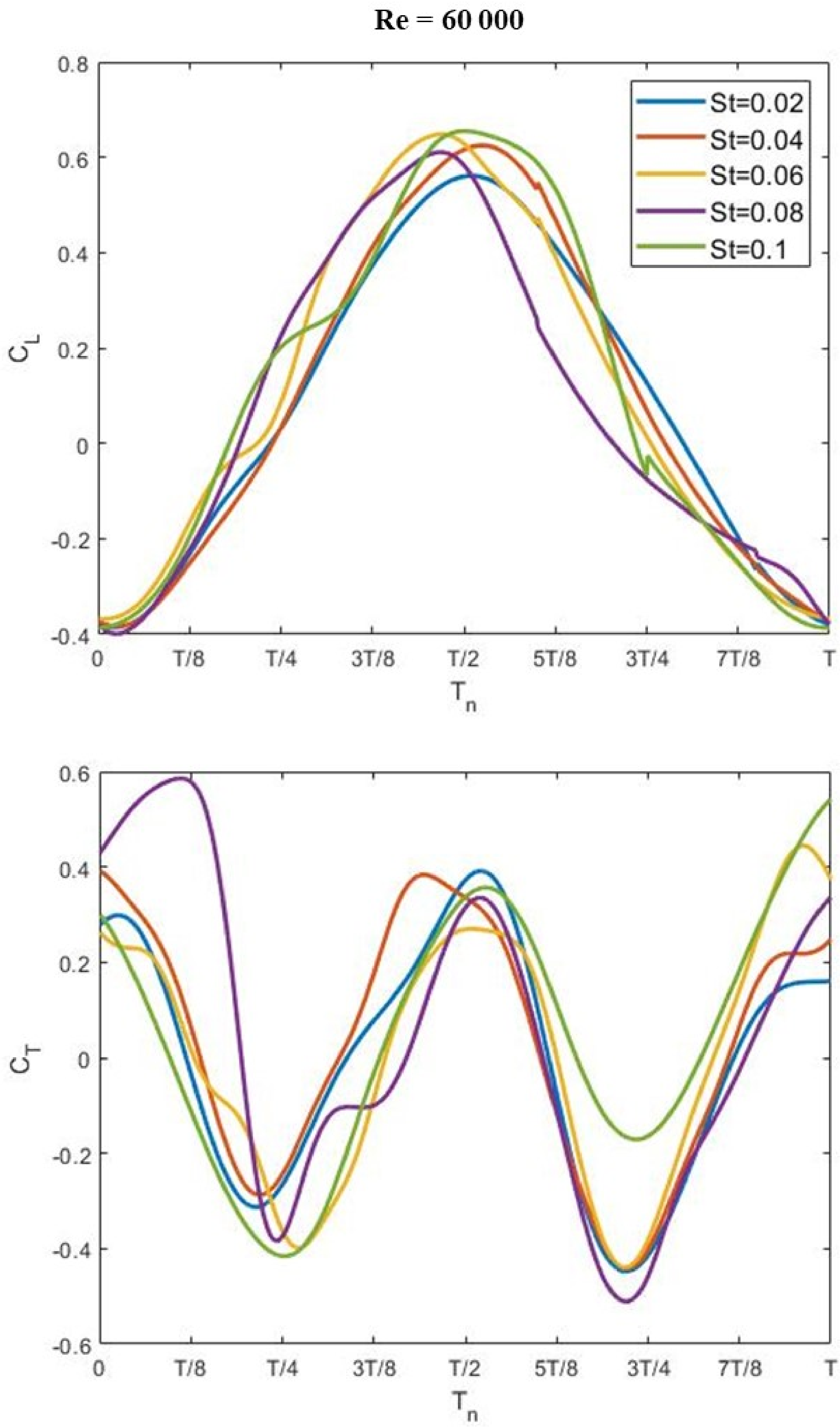

Fig. 4.14: Computational result of C_L and C_T variations of test groups with Re value of 60 000 with St values from 0.02 to 0.1

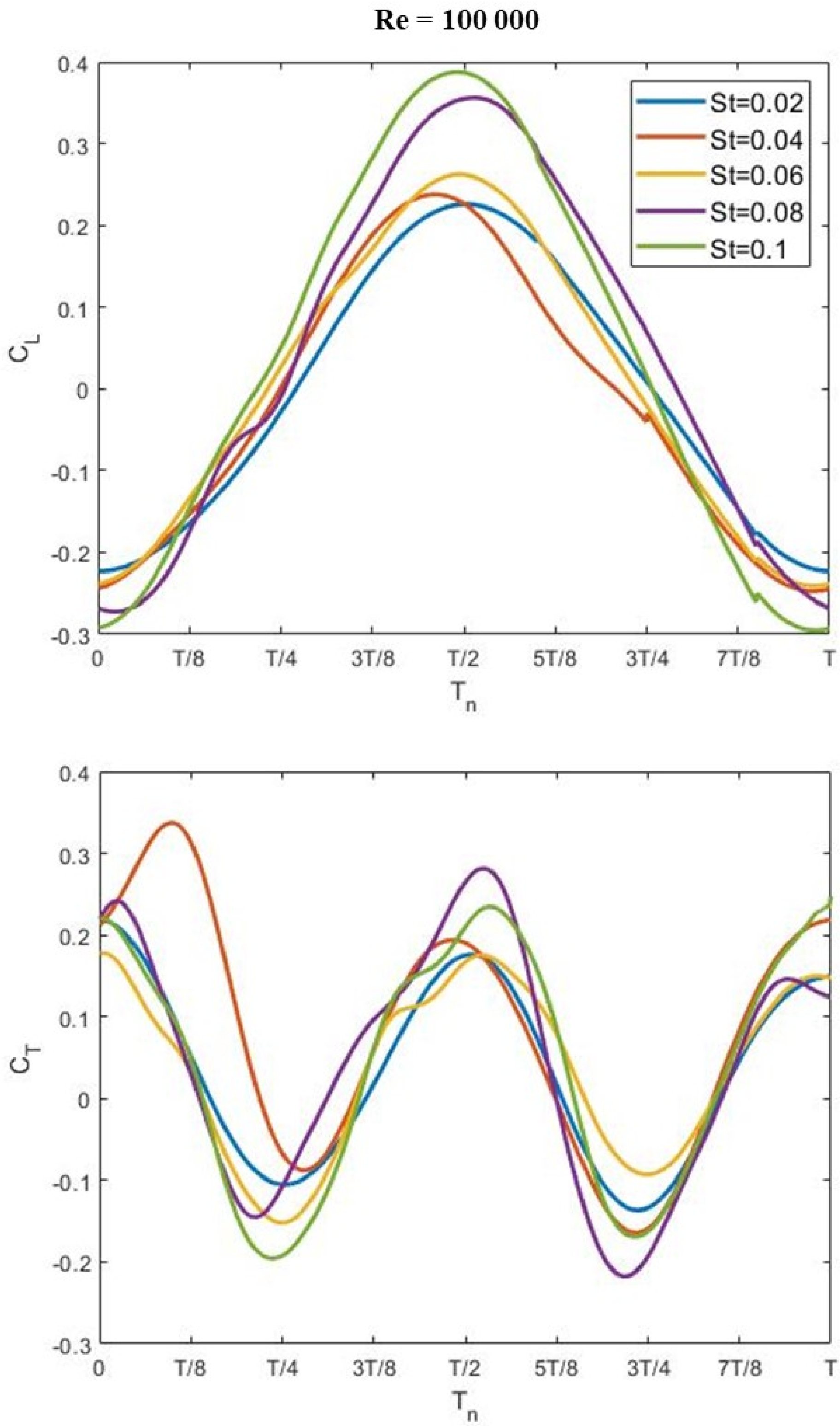

Fig. 4.15: Computational result of C_L and C_T variations of test groups with Re value of 100 000 with St values from 0.02 to 0.1

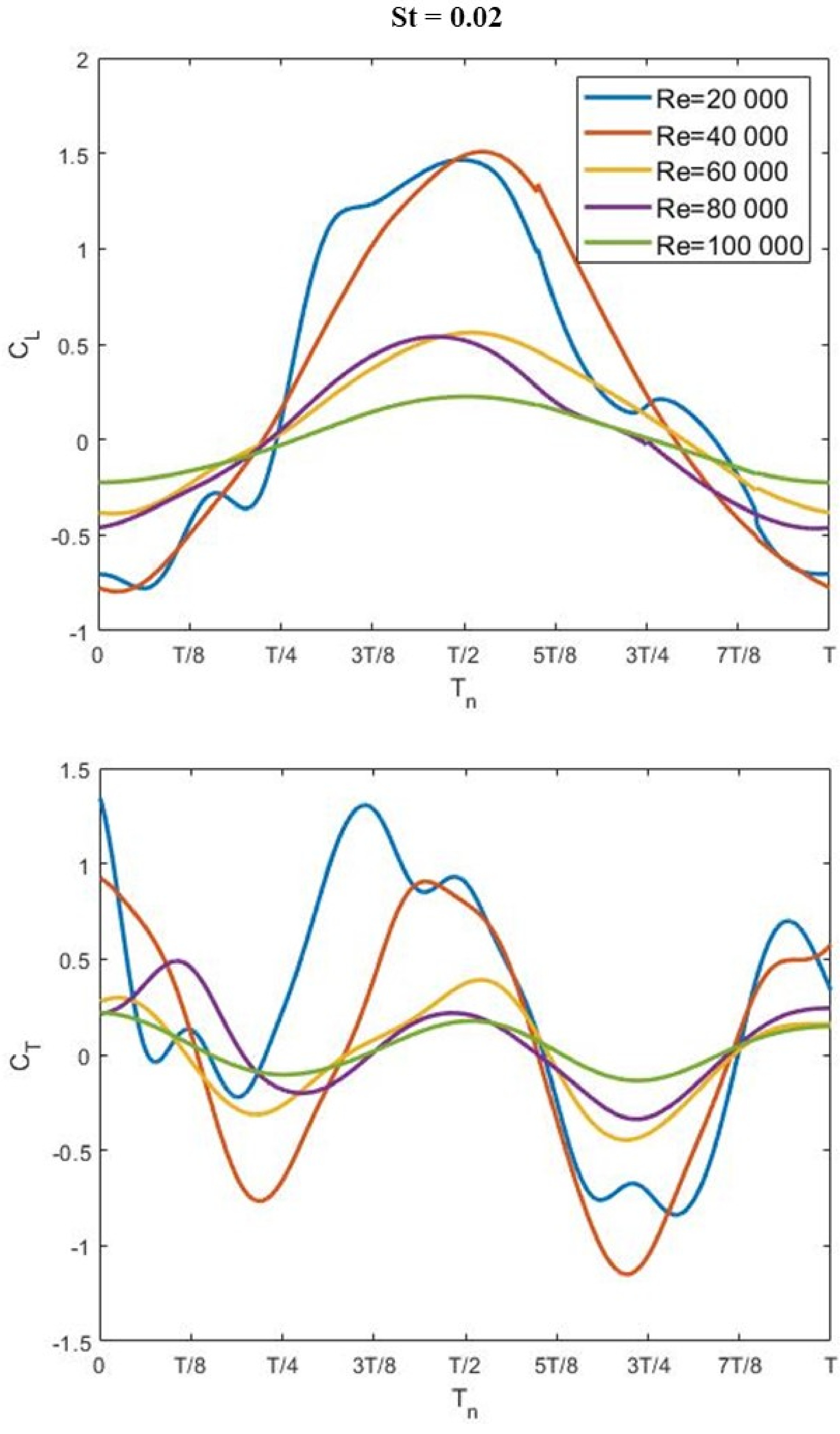

Fig. 4.16: Computational result of C_L and C_T variations of test groups with St value of 0.02 with Re values from 20 000 to 100 000

4.4.2 Comparison of average lift and thrust performance

The mean values of C_L and C_T for an average motion cycle are calculated using the exported results of computational investigations. Comparison of mean values enables to understand any overarching characteristic trends in C_L and C_T performances in pitching and plunging wing scenarios with varying Re and St values. Mean C_L values increase with increasing St values and decrease with increasing Re values. Mean C_T values increase with both increasing St and Re values. These trends were also identified in experimental measurements. However, the supplementary computational investigation results emphasize the presence of these characteristic trends within the investigated range of Re and St . The mean C_L values exhibit an average increase of 31.3% with rising St values, while they decrease by an average of 53.7% with increasing Re values. On the other hand, the mean C_T values demonstrate an average increase of 31.9% with increasing St values and a rise of 11.4% on average with increasing Re values.

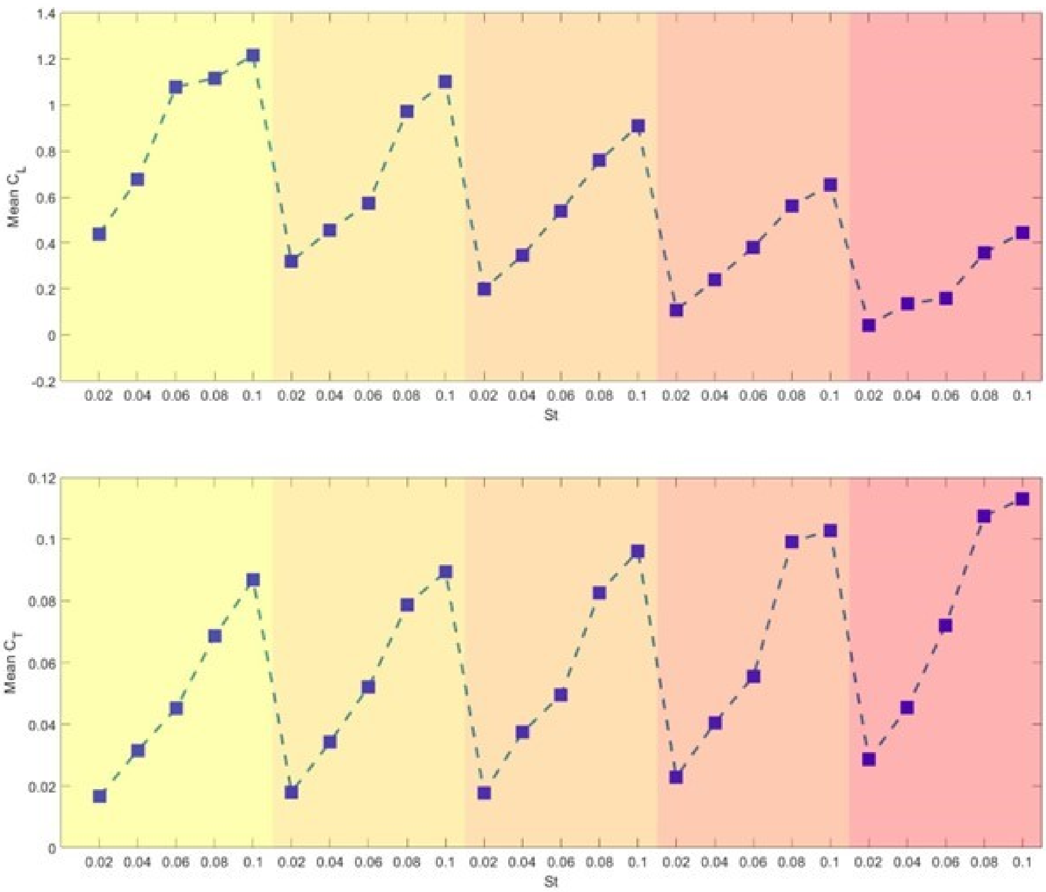

Fig. 4.17: Computational results of average C_L and C_T variation across varying $Re$and St values

4.4.3 Comparison of experimental and computational results

C_L and C_T variations and their mean values resulted from the experimental and computational investigations are comparatively analysed. Arguments for any identified deviations are formulated with the assistance of velocity and pressure contour plot results from the computational investigation. The overall agreement between the computational and experimental results is excellent. The alignment between the two sets of data increases notably with increasing Re. In comparing the mean C_L and C_T values, the characteristic trends observed in the experimental results persist in the computational data as well. While some deviations exist between the mean C_L and C_T values of the two methods, the overall agreement is deemed satisfactory as illustrated in Fig.4.18. The average percentile deviation between the experimental and computational results is 12.15$\%$ for all values with varying $Re$and St values.

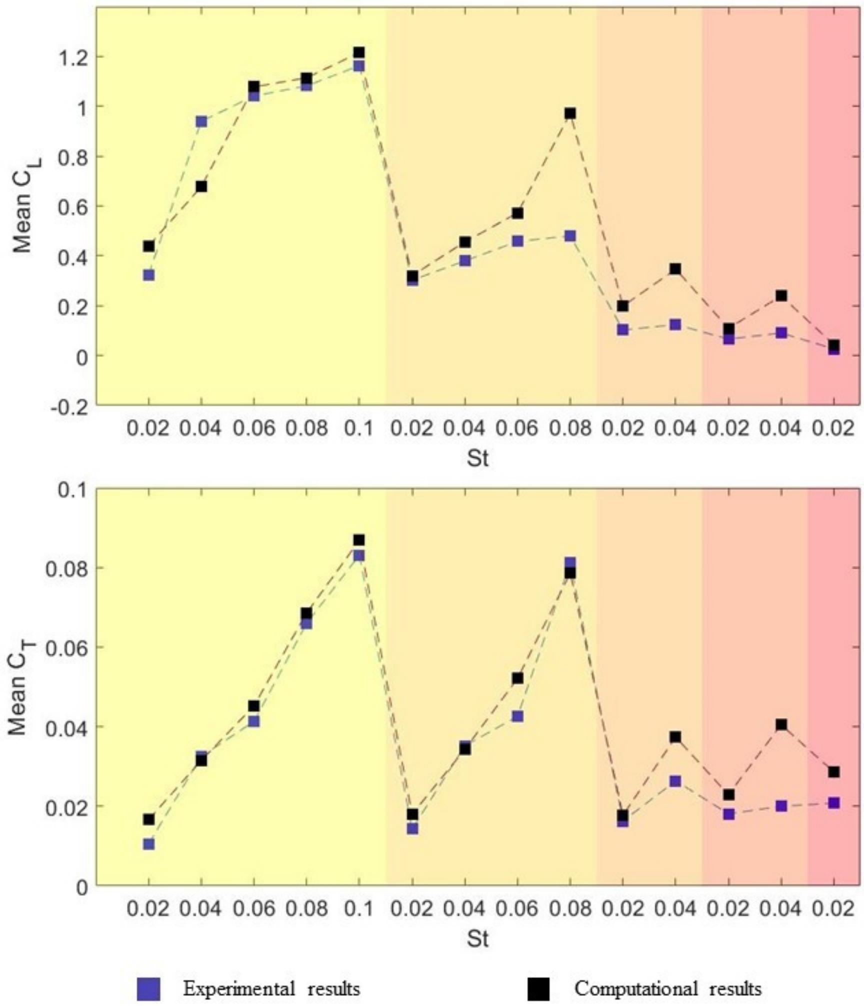

Fig. 4.18: Comparison of experimental and computational results of mean lift and thrust coefficient values

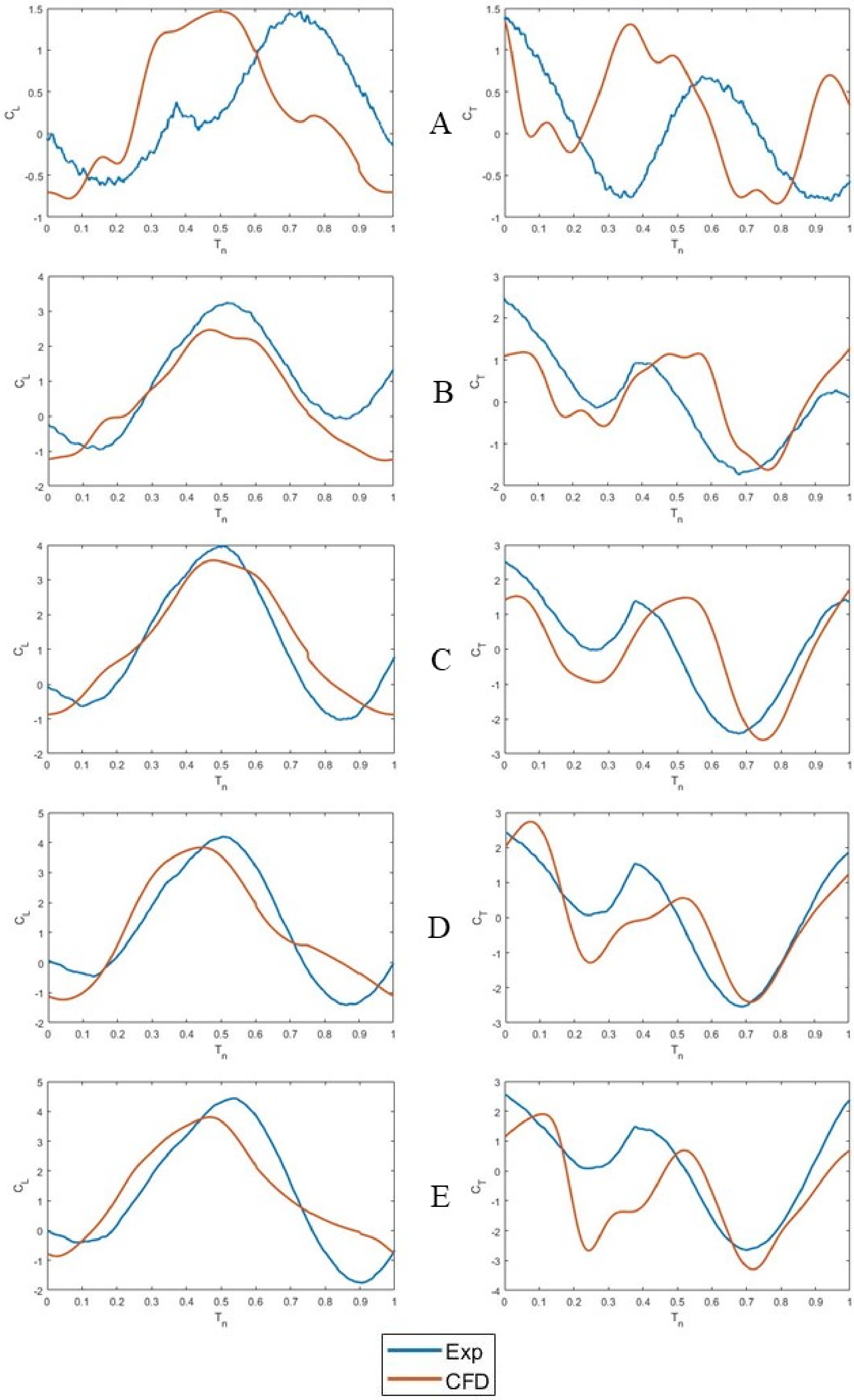

Fig. 4.19: Comparison of experimental and computational results of lift and thrust coefficient variations in different kinematic scenarios of groups A,B,C,D,E

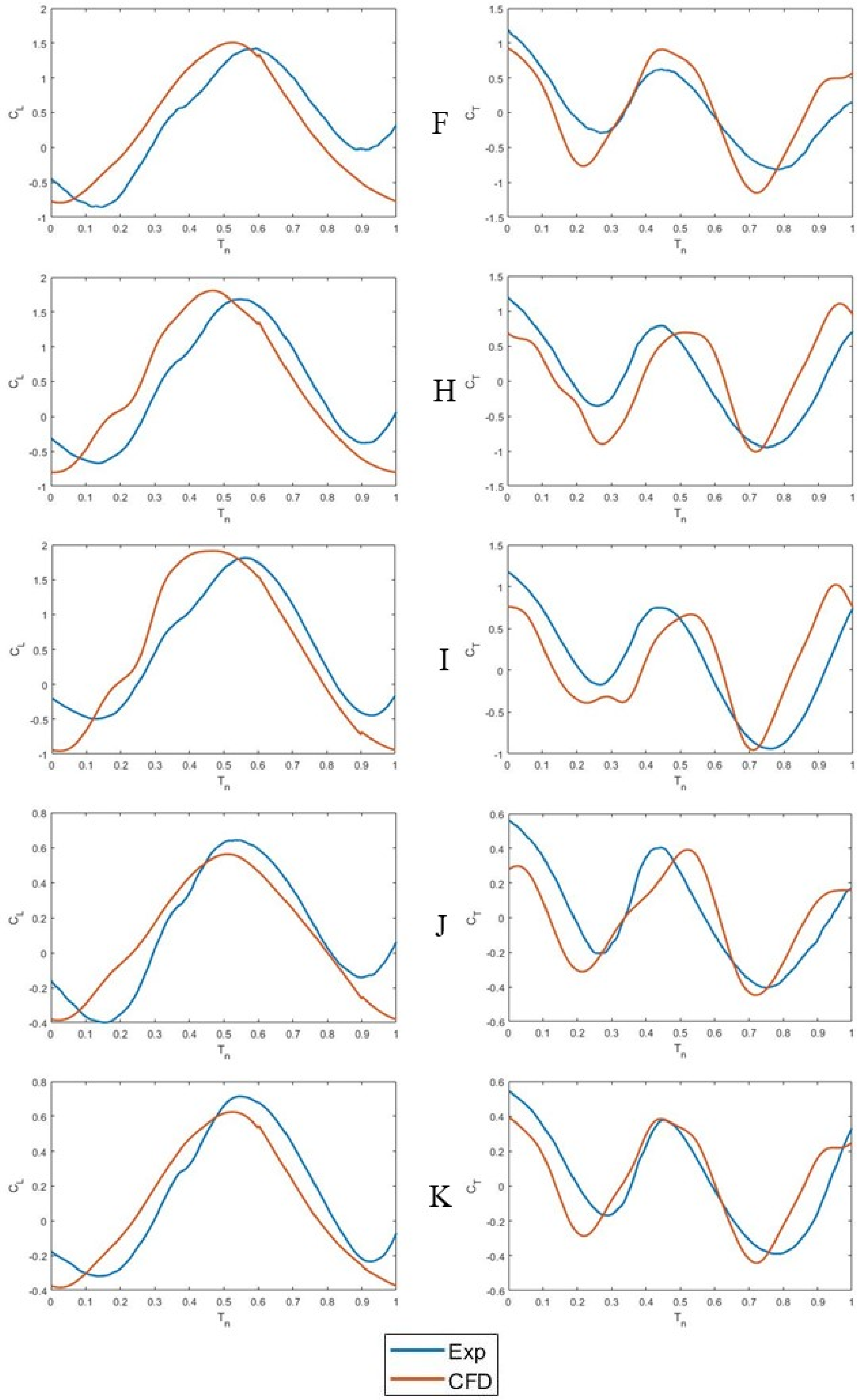

Fig. 4.20: Comparison of experimental and computational results of lift and thrust coefficient variations in different kinematic scenarios of groups F,H,I,J,K

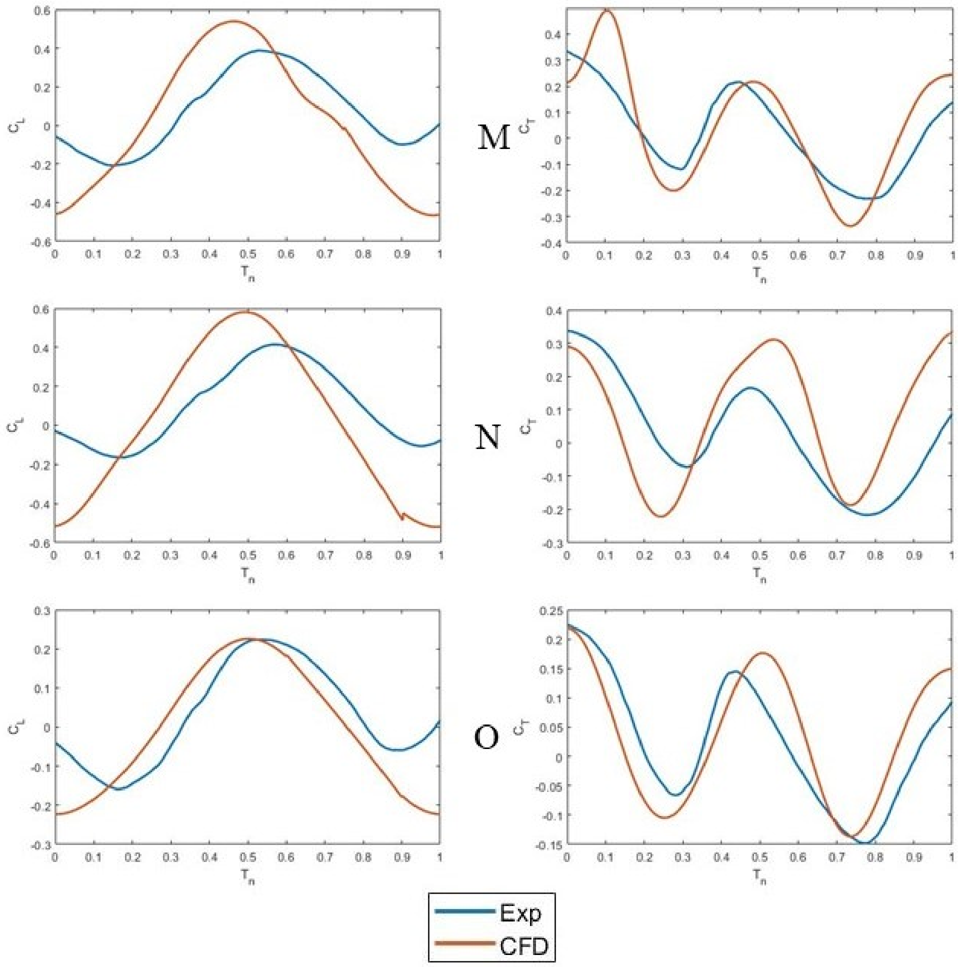

Fig. 4.21: Comparison of experimental and computational results of lift and thrust coefficient variations in different kinematic scenarios of groups M,N,O

CHAPTER 5

CONCLUSIONS AND FUTURE WORK

5.1 Conclusions

This study investigates the unsteady aerodynamic forces acting on wings subjected to combined pitching and plunging motions under different kinematic parameters. The findings of both experimental and computational investigations provide valuable insight into the underlying physics and overarching characteristics of force generation, contributing essential knowledge for the advancement of FWBAVs.

The analysis of the experimental results provides significant insights, particularly regarding the influence of the effective angle of attack on C_L variations across all test groups. Both C_L and C_T variations exhibit local maxima near stroke reversals, affirming the existence of wing wake interactions, especially in low Re values. In the C_T plots, the second valley which occurs around 0.6 to 0.8 T_n is generally observed to be lower than the first. This indicates that, even when using a symmetrical airfoil shape, the upstroke typically creates more drag in all combinations of Re and St . As the Re increases and the St decreases, gradual decrements of extremum values in transient lift and thrust coefficient variations are observed. Mean lift and thrust coefficients increase, as the St rises, with Re values constant at 20 000 and 40 000. However, the mean lift coefficient values decrease with rising Re while St values are at 0.02 and 0.04. Therefore, it can be concluded that the aerodynamic lift and thrust of a pitching and plunging wing following a symmetric sinusoidal motion without a phase difference can be predictably controlled by varying the Re and St values of their flight.

With both C_L and C_T values gradually decreasing with increasing Re values, the results indicate the inherent suitability of flapping wing propulsion for low Re flight scenarios. These trends suggest that the flight characteristics of flapping wing micro air vehicles exhibit increasing stability but decreasing efficiency as Re values rise from 20,000 to 100,000. The computational results showcase characteristic trends of C_L and C_T values which reinforce the conclusion made using the experimental results while showcasing sufficient agreement with both time-series variations and mean value comparisons. The mean C_L values increase with rising St values, while they decrease with increasing Re values. Furthermore, the mean C_T values demonstrate an increase with both increasing Re and St values.

Both experimental and computational results indicate Re region of 40 000 with St values ranging from 0.6 to 0.1 are most suitable for future FWBAV development as both C_L and C_T production are comparatively high in those regions of Re and St values.

5.2 Future work

- The experimental investigation could be enhanced by incorporating flow visualization methods, such as laser-illuminated smoke streams. Advanced techniques like Particle Image Velocimetry (PIV) would significantly increase the value of the results and help identify unsteady aerodynamic phenomena affecting the pitching and plunging wings.

- The accuracy and quality of computational results can be significantly improved by utilizing advanced turbulence modeling techniques such as Large Eddy Simulation (LES) and Direct Numerical Simulation (DNS). While these methods demand substantial computational resources and high-performance computing capabilities making them significantly more expensive than the Reynolds-Averaged Navier-Stokes (RANS) approach used in this research, they offer superior accuracy. LES enhances accuracy by directly resolving large-scale unsteady structures, enabling a more precise representation of transient and separated flows. Meanwhile, DNS provides the most detailed turbulence representation by solving the full time-dependent Navier-Stokes equations without any averaging. Despite their higher computational cost, these methods offer considerable benefits in capturing complex flow phenomena with greater fidelity.

- Given the financial and time commitments inherent in both experimental and computational investigations, future endeavors should prioritize the development of a numerical simulation tool for modeling the aerodynamics of pitching and plunging wings. The insights gleaned from this investigation would significantly aid in such development. Such a numerical simulation tool would greatly assist in future Flapping Wing Bioinspired Aerial Vehicles (FWBAVs) developments by reducing the cost and time demands of the designing stage.

- The pursuit of creating efficient, capable, and reliable FWBAVs requires ongoing research and development efforts. This entails integrating aerodynamic investigations with advancements in robotics, focusing on lightweight and efficient actuators, and materials science, emphasizing flexible wing and body construction. Additionally, advancements in aeronautics are crucial for developing novel in-flight navigation and automation techniques for FWBAVs. Continuous progress in these areas is essential to surpass the performance of rotary-wing UAVs in future developments.

REFERENCES

[1] K. Smith, J. Butt, M. von Spakovsky, and D. Moorhouse, "A study of the benefits of using morphing wing technology in fighter aircraft systems," in *39th AIAA Thermophysics Conference*. American Institute of Aeronautics and Astronautics, Jun. 2007. [Online]. Available: http://dx.doi.org/10.2514/6.2007-4616

[2] N. Haider, A. Shahzad, M. N. Mumtaz Qadri, and S. I. Ali Shah, "Recent progress in flapping wings for micro aerial vehicle applications," *Proceedings of the Institution of Mechanical Engineers, Part C: Journal of Mechanical Engineering Science*, vol. 235, no. 2, p. 245–264, Jun. 2020. [Online]. Available: http://dx.doi.org/10.1177/0954406220917426

[3] S. Xiao, K. Hu, B. Huang, H. Deng, and X. Ding, "A review of research on the mechanical design of hoverable flapping wing micro-air vehicles," *Journal of Bionic Engineering*, vol. 18, no. 6, p. 1235–1254, Nov. 2021. [Online]. Available: http://dx.doi.org/10.1007/s42235-021-00118-4

[4] A. Rodriguez, "Morphing aircraft technology survey," in *45th AIAA Aerospace Sciences Meeting and Exhibit*. American Institute of Aeronautics and Astronautics, Jan. 2007. [Online]. Available: https://doi.org/10.2514/6.2007-1258

[5] W. J. Maybury, "The aerodynamics of bird bodies," Ph.D. dissertation, University of Bristol, 2000.

[6] H. Xuan, J. Hu, Y. Yu, and J. Zhang, "Recent progress in aerodynamic modeling methods for flapping flight," *AIP Advances*, vol. 10, no. 2, Feb. 2020. [Online]. Available: http://dx.doi.org/10.1063/1.5130900

[7] M. Platzer and K. Jones, "Flapping-wing micro air vehicles," in *Flow Phenomena in Nature Volume 2*. WIT Press, Nov. 2006, pp. 393–399. [Online]. Available: https://doi.org/10.2495/1-84564-095-0/5b

[8] T. N. Sullivan, M. A. Meyers, and E. Arzt, "Scaling of bird wings and feathers for efficient flight," *Science Advances*, vol. 5, no. 1, Jan. 2019. [Online]. Available: https://doi.org/10.1126/sciadv.aat4269

[9] L. Hedh, C. G. Guglielmo, L. C. Johansson, J. E. Deakin, C. C. Voigt, and A. Hedenström, "Measuring power input, power output and energy conversion efficiency in un-instrumented flying birds," *Journal of Experimental Biology*, Jan. 2020. [Online]. Available: http://dx.doi.org/10.1242/jeb.223545

[10] T. Pornsin-Sirirak, Y.-C. Tai, C.-M. Ho, and M. Keennon, "Microbat: A palm-sized electrically powered ornithopter," *Proceedings of NASA/JPL Workshop on Biomorphic Robotics*, pp. 14 – 17, 2001. [Online]. Available: http://ho.seas.ucla.edu/wp-content/uploads/2011/04/jpl10_2001.pdf

[11] R. Wood, "The first takeoff of a biologically inspired at-scale robotic insect," *IEEE Transactions on Robotics*, vol. 24, no. 2, pp. 341–347, Apr. 2008. [Online]. Available: https://doi.org/10.1109/tro.2008.916997

[12] G. de Croon, K. de Clercq, R. Ruijsink, B. Remes, and C. de Wagter, "Design, aerodynamics, and vision-based control of the DelFly," *International Journal of Micro Air Vehicles*, vol. 1, no. 2, pp. 71–97, Jun. 2009. [Online]. Available: https://doi.org/10.1260/175682909789498288

[13] R. Y. Krashanitsa, D. Silin, S. V. Shkarayev, and G. Abate, "Flight dynamics of a flapping-wing air vehicle," *International Journal of Micro Air Vehicles*, vol. 1, no. 1, pp. 35–49, Mar. 2009. [Online]. Available: https://doi.org/10.1260/1756-8293.1.1.35

[14] M. Keennon, K. Klingebiel, and H. Won, "Development of the nano hummingbird: A tailless flapping wing micro air vehicle," in *50th AIAA Aerospace Sciences Meeting including the New Horizons Forum and Aerospace Exposition*. American Institute of Aeronautics and Astronautics, Jan. 2012. [Online]. Available: https://doi.org/10.2514/6.2012-588

[15] J. W. Gerdes, S. K. Gupta, and S. A. Wilkerson, "A review of bird-inspired flapping wing miniature air vehicle designs," *Journal of Mechanisms and Robotics*, vol. 4, no. 2, Apr. 2012. [Online]. Available: https://doi.org/10.1115/1.4005525

[16] W. Yang, L. Wang, and B. Song, "Dove: A biomimetic flapping-wing micro air vehicle," *International Journal of Micro Air Vehicles*, vol. 10, no. 1, pp. 70–84, Oct. 2017. [Online]. Available: https://doi.org/10.1177/1756829317734837

[17] M. H. Dickinson, F.-O. Lehmann, and S. P. Sane, "Wing rotation and the aerodynamic basis of insect flight," *Science*, vol. 284, no. 5422, pp. 1954–1960, Jun. 1999. [Online]. Available: https://doi.org/10.1126/science.284.5422.1954

[18] K. Isaac, A. Colozza, and J. Rolwes, "Force measurements on a flapping and pitching wing at low reynolds numbers," in *44th AIAA Aerospace Sciences Meeting and Exhibit*. American Institute of Aeronautics and Astronautics, Jan. 2006. [Online]. Available: https://doi.org/10.2514/6.2006-450

[19] T. Y. Hubel and C. Tropea, "Experimental investigation of a flapping wing model," *Experiments in Fluids*, vol. 46, no. 5, pp. 945–961, Dec. 2008. [Online]. Available: https://doi.org/10.1007/s00348-008-0599-9

[20] K. Mazaheri and A. Ebrahimi, "Experimental investigation on aerodynamic performance of a flapping wing vehicle in forward flight," *Journal of Fluids and Structures*, vol. 27, no. 4, pp. 586–595, May 2011. [Online]. Available: https://doi.org/10.1016/j.jfluidstructs.2011.04.001

[21] S. S. Bhat, J. Zhao, J. Sheridan, K. Hourigan, and M. C. Thompson, "Effects of flapping-motion profiles on insect-wing aerodynamics," *Journal of Fluid Mechanics*, vol. 884, Dec. 2019. [Online]. Available: https://doi.org/10.1017/jfm.2019.929

[22] G. Kenneth, M. Ol, and L. Bernal, "Experiments on pitching plates: Force and flowfield measurements at low reynolds numbers," in *49th AIAA Aerospace Sciences Meeting including the New Horizons Forum and Aerospace Exposition*. American Institute of Aeronautics and Astronautics, Jan. 2011. [Online]. Available: https://doi.org/10.2514/6.2011-872

[23] R. B. R. Vandenheede, L. P. Bernal, C. L. Morrison, A. Gogulapati, P. P. Friedmann, C.-K. Kang, and W. Shyy, "Experimental and computational study on flapping wings with bio-inspired hover kinematics," *AIAA Journal*, vol. 52, no. 5, pp. 1047–1058, May 2014. [Online]. Available: https://doi.org/10.2514/1.j052644

[24] D. Cleaver, D. Calderon, Z. Wang, and I. Gursul, "Lift enhancement through flexibility of plunging wings at low reynolds numbers," *Journal of Fluids and Structures*, vol. 64, pp. 27–45, Jul. 2016. [Online]. Available: https://doi.org/10.1016/j.jfluidstructs.2016.04.004

[25] S. Ōtomo, S. Henne, K. Mulleners, K. Ramesh, and I. M. Viola, "Unsteady lift on a high-amplitude pitching aerofoil," *Experiments in Fluids*, vol. 62, no. 1, Dec. 2020. [Online]. Available: https://doi.org/10.1007/s00348-020-03095-2

[26] S. J. Lighthill, *Mathematical Biofluiddynamics*. Society for Industrial and Applied Mathematics, Jan. 1975. [Online]. Available: https://doi.org/10.1137/1.9781611970517

[27] M. J. Benton, "How birds became birds," *Science*, vol. 345, no. 6196, pp. 508–509, Aug. 2014. [Online]. Available: https://doi.org/10.1126/science.1257633

[28] S. L. Brusatte, J. K. O'Connor, and E. D. Jarvis, "The origin and diversification of birds," *Current Biology*, vol. 25, no. 19, pp. R888–R898, Oct. 2015. [Online]. Available: https://doi.org/10.1016/j.cub.2015.08.003

[29] D. D. Chin and D. Lentink, "Flapping wing aerodynamics: from insects to vertebrates," *Journal of Experimental Biology*, vol. 219, no. 7, pp. 920–932, Apr. 2016. [Online]. Available: https://doi.org/10.1242/jeb.042317

[30] J. Toomey and J. D. Eldredge, "Numerical and experimental study of the fluid dynamics of a flapping wing with low order flexibility," *Physics of Fluids*, vol. 20, no. 7, Jul. 2008. [Online]. Available: https://doi.org/10.1063/1.2956372

[31] R. Dvořák, "Aerodynamics of bird flight," *EPJ Web of Conferences*, vol. 114, p. 01001, 2016. [Online]. Available: https://doi.org/10.1051/epjconf/201611401001

[32] D. L. Altshuler, J. W. Bahlman, R. Dakin, A. H. Gaede, B. Goller, D. Lentink, P. S. Segre, and D. A. Skandalis, "The biophysics of bird flight: functional relationships integrate aerodynamics, morphology, kinematics, muscles, and sensors," *Canadian Journal of Zoology*, vol. 93, no. 12, pp. 961–975, Dec. 2015. [Online]. Available: https://doi.org/10.1139/cjz-2015-0103

[33] B. Bruderer and A. Boldt, "Flight characteristics of birds:," *Ibis*, vol. 143, no. 2, pp. 178–204, Apr. 2001. [Online]. Available: https://doi.org/10.1111/j.1474-919x.2001.tb04475.x

[34] B. Bruderer, D. Peter, A. Boldt, and F. Liechti, "Wing-beat characteristics of birds recorded with tracking radar and cine camera," *Ibis*, vol. 152, no. 2, pp. 272–291, Apr. 2010. [Online]. Available: https://doi.org/10.1111/j.1474-919x.2010.01014.x

[35] S. Sunada, K. Kawachi, A. Matsumoto, and A. Sakaguchi, "Unsteady forces on a two-dimensional wing in plunging and pitching motions," *AIAA Journal*, vol. 39, no. 7, pp. 1230–1239, Jul. 2001. [Online]. Available: https://doi.org/10.2514/2.1458

[36] K. Jones, B. Castro, O. Mahmoud, S. Pollard, M. Platzer, M. Neef, K. Gonet, and D. Hummel, "A collaborative numerical and experimental investigation of flapping-wing propulsion," in *40th AIAA Aerospace Sciences Meeting &amp Exhibit*. American Institute of Aeronautics and Astronautics, Jan. 2002. [Online]. Available: https://doi.org/10.2514/6.2002-706

[37] Y. S. Baik, J. Rausch, L. Bernal, and M. Ol, "Experimental investigation of pitching and plunging airfoils at reynolds number between 1x10^4

and 6x10ˆ4," in *39th AIAA Fluid Dynamics Conference*. American Institute of Aeronautics and Astronautics, Jun. 2009. [Online]. Available: https://doi.org/10.2514/6.2009-4030

[38] H. Aono, S. K. Chimakurthi, P. Wu, E. Sallstrom, B. Stanford, C. Cesnik, P. Ifju, L. Ukeiley, and W. Shyy, "A computational and experimental studies of flexible wing aerodynamics," in *48th AIAA Aerospace Sciences Meeting Including the New Horizons Forum and Aerospace Exposition*. American Institute of Aeronautics and Astronautics, Jan. 2010. [Online]. Available: https://doi.org/10.2514/6.2010-554

[39] L. Chen, J. Wu, C. Zhou, S.-J. Hsu, and B. Cheng, "Unsteady aerodynamics of a pitching-flapping-perturbed revolving wing at low reynolds number," *Physics of Fluids*, vol. 30, no. 5, p. 051903, May 2018. [Online]. Available: https://doi.org/10.1063/1.5024925

[40] M. Moriche, G. Sedky, A. R. Jones, O. Flores, and M. García-Villalba, "Characterization of aerodynamic forces on wings in plunge maneuvers," *AIAA Journal*, vol. 59, no. 2, pp. 751–762, Feb. 2021. [Online]. Available: https://doi.org/10.2514/1.j059689

[41] J. H. Wu and M. Sun, "Unsteady aerodynamic forces of a flapping wing," *Journal of Experimental Biology*, vol. 207, no. 7, pp. 1137–1150, Mar. 2004. [Online]. Available: https://doi.org/10.1242/jeb.00868

[42] I. Garrick, "Propulsion of a flapping and oscillating airfoil - nasa technical reports server ntrs) — ntrs.nasa.gov," https://ntrs.nasa.gov/citations/19930091642, 1939, [Accessed 20-10-2023].

[43] B. C. Basu and G. J. Hancock, "The unsteady motion of a two-dimensional aerofoil in incompressible inviscid flow," *Journal of Fluid Mechanics*, vol. 87, no. 1, pp. 159–178, Jul. 1978. [Online]. Available: https://doi.org/10.1017/s0022112078002980

[44] W. J. McCroskey, "Unsteady airfoils," *Annual Review of Fluid Mechanics*, vol. 14, no. 1, pp. 285–311, Jan. 1982. [Online]. Available: https://doi.org/10.1146/annurev.fl.14.010182.001441

[45] I. Tuncer, R. Walz, and M. Platzer, "A computational study on the dynamic stall of a flapping airfoil," in *16th AIAA Applied Aerodynamics Conference*. American Institute of Aeronautics and Astronautics, Jun. 1998. [Online]. Available: http://dx.doi.org/10.2514/6.1998-2519

[46] I. H. Tuncer and M. F. Platzer, “Computational study of flapping airfoil aerodynamics,” *Journal of Aircraft*, vol. 37, no. 3, p. 514–520, May 2000. [Online]. Available: http://dx.doi.org/10.2514/2.2628

[47] R. Ramamurti and W. Sandberg, “Computational study of 3-d flapping foil flows,” in *39th Aerospace Sciences Meeting and Exhibit*. American Institute of Aeronautics and Astronautics, Jan. 2001. [Online]. Available: http://dx.doi.org/10.2514/6.2001-605

[48] T. K. Sengupta, V. Vikas, and A. Johri, “An improved method for calculating flow past flapping and hovering airfoils,” *Theoretical and Computational Fluid Dynamics*, vol. 19, no. 6, p. 417–440, Dec. 2005. [Online]. Available: http://dx.doi.org/10.1007/s00162-005-0003-9

[49] X. Yu and M. Sun, “A computational study of the wing–wing and wing–body interactions of a model insect,” *Acta Mechanica Sinica*, vol. 25, no. 4, p. 421–431, May 2009. [Online]. Available: http://dx.doi.org/10.1007/s10409-009-0266-2

[50] D. Ishihara, T. Horie, and T. Niho, “An experimental and three-dimensional computational study on the aerodynamic contribution to the passive pitching motion of flapping wings in hovering flies,” *Bioinspiration amp; Biomimetics*, vol. 9, no. 4, p. 046009, Nov. 2014. [Online]. Available: http://dx.doi.org/10.1088/1748-3182/9/4/046009

[51] D. Kurtulus, *Unsteady aerodynamics of flapping aerofoils: case studies with experimental, numerical, theoretical and soft computing methods*, 04 2011, pp. 187–217.

[52] D. F. Kurtulus, “Unsteady aerodynamics of a pitching naca 0012 airfoil at low reynolds number,” *International Journal of Micro Air Vehicles*, vol. 11, p. 175682931989060, Jan. 2019.

[53] N. Poudel, L. Wang, M. Yu, and J. T. Hrynuk, “Computational study of flapping wing response to vertical gusts at low reynolds numbers,” in *AIAA Scitech 2020 Forum*. American Institute of Aeronautics and Astronautics, Jan. 2020. [Online]. Available: http://dx.doi.org/10.2514/6.2020-2046

[54] K. M. D. Clercq, R. de Kat, B. Remes, B. W. van Oudheusden, and H. Bijl, “Aerodynamic experiments on DelFly II: Unsteady lift enhancement,” *International Journal of Micro Air Vehicles*, vol. 1, no. 4, pp. 255–262, Dec. 2009. [Online]. Available: https://doi.org/10.1260/175682909790291465

[55] W. Send, M. Fischer, K. Jebens, R. Mugrauer, A. Nagarathinam, and F. Scharstein, "Artificial hinged-wing bird with active torsion and partially linear kinematics," *28th Congress of the International Council of the Aeronautical Sciences 2012, ICAS 2012*, vol. 2, pp. 1148–1157, 2012.

[56] W. Shyy, H. Aono, C. kwon Kang, and H. Liu, *An Introduction to Flapping Wing Aerodynamics*. Cambridge University Press, Jun. 2013. [Online]. Available: https://doi.org/10.1017/cbo9781139583916

[57] R. H. J. BROWN, "The flight of birds," *Biological Reviews*, vol. 38, no. 4, pp. 460–489, 1963. [Online]. Available: https://onlinelibrary.wiley.com/doi/abs/10.1111/j.1469-185X.1963.tb00790.x

[58] M. F. Platzer, K. D. Jones, J. Young, and J. C. S. Lai, "Flapping wing aerodynamics: Progress and challenges," *AIAA Journal*, vol. 46, no. 9, pp. 2136–2149, Sep. 2008. [Online]. Available: https://doi.org/10.2514/1.29263

[59] I. Gursul and D. Cleaver, "Plunging oscillations of airfoils and wings: Progress, opportunities, and challenges," *AIAA Journal*, vol. 57, no. 9, p. 3648–3665, Sep. 2019. [Online]. Available: http://dx.doi.org/10.2514/1.J056655

[60] J. M. Anderson, K. Streilien, D. S. Barrett, and M. S. Traintafyllou, "Oscillating foils of high propulsive efficiency," *Journal of Fluid Mechanics*, vol. 360, p. 41–72, Apr. 1998. [Online]. Available: http://dx.doi.org/10.1017/S0022112097008392

[61] W. Chakroun, I. Al-Mesri, and S. Al-Fahad, "Effect of surface roughness on the aerodynamic characteristics of a symmetrical airfoil," *Wind Engineering*, vol. 28, no. 5, pp. 547–564, Sep. 2004. [Online]. Available: https://doi.org/10.1260/0309524043028136

[62] AGARD Advisory Report 304 and Fluid Dynamics Panel Working Group 15, "Quality Assessment for Wind Tunnel Testing."

[63] J. Young and J. C. S. Lai, "Mechanisms influencing the efficiency of oscillating airfoil propulsion," *AIAA Journal*, vol. 45, no. 7, pp. 1695–1702, Jul. 2007. [Online]. Available: https://doi.org/10.2514/1.27628

[64] G. Ellis, "Introduction to controls," in *Control System Design Guide*. Elsevier, 2012, pp. 3–7.

[65] S. W. Smith, *Digital Signal Processing: A practical guide for engineers and scientists*. Newnes, Elsevier Science, 2003.

[66] D.-H. Kim and J.-W. Chang, “Low-reynolds-number effect on the aerodynamic characteristics of a pitching NACA0012 airfoil,” *Aerospace Science and Technology*, vol. 32, no. 1, pp. 162–168, Jan. 2014. [Online]. Available: https://doi.org/10.1016/j.ast.2013.08.018

[67] C. P. Ellington, C. van den Berg, A. P. Willmott, and A. L. R. Thomas, “Leading-edge vortices in insect flight,” *Nature*, vol. 384, no. 6610, pp. 626–630, Dec. 1996. [Online]. Available: https://doi.org/10.1038/384626a0

[68] C. van den Berg and C. P. Ellington, “The three–dimensional leading–edge vortex of a ‘hovering’ model hawkmoth,” *Philosophical Transactions of the Royal Society of London. Series B: Biological Sciences*, vol. 352, no. 1351, pp. 329–340, Mar. 1997. [Online]. Available: https://doi.org/10.1098/rstb.1997.0024

[69] A. L. R. Thomas, G. K. Taylor, R. B. Srygley, R. L. Nudds, and R. J. Bomphrey, “Dragonfly flight: free-flight and tethered flow visualizations reveal a diverse array of unsteady lift-generating mechanisms, controlled primarilyivia/iangle of attack,” *Journal of Experimental Biology*, vol. 207, no. 24, pp. 4299–4323, Nov. 2004. [Online]. Available: https://doi.org/10.1242/jeb.01262

[70] W. Shyy and H. Liu, “Flapping wings and aerodynamic lift: The role of leading-edge vortices,” *AIAA Journal*, vol. 45, no. 12, pp. 2817–2819, Dec. 2007. [Online]. Available: https://doi.org/10.2514/1.33205

[71] J. M. Birch and M. H. Dickinson, “The influence of wing–wake interactions on the production of aerodynamic forces in flapping flight,” *Journal of Experimental Biology*, vol. 206, no. 13, pp. 2257–2272, Jul. 2003. [Online]. Available: https://doi.org/10.1242/jeb.00381

[72] A. P. Willmott, C. P. Ellington, and A. L. R. Thomas, “Flow visualization and unsteady aerodynamics in the flight of the hawkmoth, imanduca sexta/i,” *Philosophical Transactions of the Royal Society of London. Series B: Biological Sciences*, vol. 352, no. 1351, pp. 303–316, Mar. 1997. [Online]. Available: https://doi.org/10.1098/rstb.1997.0022

[73] L. De Silva, N. Samaraweera, N. Jayaweera, and T. Sugathapala, “A computational study of the aerodynamics of plunging and pitching motions of airfoils,” in *2022 Moratuwa Engineering Research Conference (MERCon)*. IEEE, Jul. 2022. [Online]. Available: http://dx.doi.org/10.1109/MERCon55799.2022.9906181

[74] K. B. Lua, Y. J. Lee, T. T. Lim, and K. S. Yeo, "Wing–wake interaction of three-dimensional flapping wings," *AIAA Journal*, vol. 55, no. 3, pp. 729–739, Mar. 2017. [Online]. Available: https://doi.org/10.2514/1.j055214

[75] ANSYS FLUENT 13 User's Guide, "Ansys Fluent Theory Guide," *ANSYS Inc., USA*, vol. 15317, no. November, pp. 724–746, 2013.

[76] G. Alfonsi, "Reynolds-averaged navier–stokes equations for turbulence modeling," *Applied Mechanics Reviews*, vol. 62, no. 4, Jun. 2009. [Online]. Available: http://dx.doi.org/10.1115/1.3124648

[77] F. R. Menter, R. Langtry, and S. Völker, "Transition modelling for general purpose cfd codes," *Flow, Turbulence and Combustion*, vol. 77, no. 1–4, p. 277–303, Aug. 2006. [Online]. Available: http://dx.doi.org/10.1007/s10494-006-9047-1

[78] F. R. Menter and Y. Egorov, "The scale-adaptive simulation method for unsteady turbulent flow predictions. part 1: Theory and model description," *Flow, Turbulence and Combustion*, vol. 85, no. 1, p. 113–138, Jun. 2010. [Online]. Available: http://dx.doi.org/10.1007/s10494-010-9264-5

[79] P. Malan, K. Suluksna, and E. Juntasaro, "Calibrating the gamma-re-theta transition model for commercial cfd," in *47th AIAA Aerospace Sciences Meeting including The New Horizons Forum and Aerospace Exposition*. American Institute of Aeronautics and Astronautics, Jan. 2009. [Online]. Available: http://dx.doi.org/10.2514/6.2009-1142

[80] S. Rodriguez, *Applied Computational Fluid Dynamics and Turbulence Modeling: Practical Tools, Tips and Techniques*. Springer International Publishing, 2019. [Online]. Available: http://dx.doi.org/10.1007/978-3-030-28691-0

[81] P. Spalart, "Trends in turbulence treatments," in *Fluids 2000 Conference and Exhibit*. American Institute of Aeronautics and Astronautics, Jun. 2000. [Online]. Available: http://dx.doi.org/10.2514/6.2000-2306

[82] P. Bradshaw, "Turbulent secondary flows," *Annual Review of Fluid Mechanics*, vol. 19, no. 1, p. 53–74, Jan. 1987. [Online]. Available: http://dx.doi.org/10.1146/annurev.fl.19.010187.000413

[83] *Proceedings of the Royal Society of London. A. Mathematical and Physical Sciences*, vol. 317, no. 1530, p. 417–433, Jun. 1970. [Online]. Available: http://dx.doi.org/10.1098/rspa.1970.0125

[84] D. C. Wilcox, "Formulation of the k-w turbulence model revisited," *AIAA Journal*, vol. 46, no. 11, p. 2823–2838, Nov. 2008. [Online]. Available: http://dx.doi.org/10.2514/1.36541

[85] D. K. Walters and D. Cokljat, "A three-equation eddy-viscosity model for reynolds-averaged navier–stokes simulations of transitional flow," *Journal of Fluids Engineering*, vol. 130, no. 12, Oct. 2008. [Online]. Available: http://dx.doi.org/10.1115/1.2979230

[86] F. R. Menter, "Two-equation eddy-viscosity turbulence models for engineering applications," *AIAA Journal*, vol. 32, no. 8, p. 1598–1605, Aug. 1994. [Online]. Available: http://dx.doi.org/10.2514/3.12149

[87] R. B. Langtry and F. R. Menter, "Correlation-based transition modeling for unstructured parallelized computational fluid dynamics codes," *AIAA Journal*, vol. 47, no. 12, p. 2894–2906, Dec. 2009. [Online]. Available: http://dx.doi.org/10.2514/1.42362

[88] J. D. Anderson, *Computational Fluid Dynamics*, ser. McGraw-Hill series in mechanical engineering. New York, NY: McGraw-Hill Professional, Feb. 1995.

[89] H. Jasak, "Error analysis and estimation for the finite volume method with applications to fluid flows," *Direct*, vol. M, 01 1996.

[90] A. Inc., "Spatial Discretization," https://www.afs.enea.it/project/neptunius/docs/fluent/html/th/node366.htm.

[91] M. Darwish, I. Sraj, and F. Moukalled, "A coupled finite volume solver for the solution of incompressible flows on unstructured grids," *Journal of Computational Physics*, vol. 228, no. 1, p. 180–201, Jan. 2009. [Online]. Available: http://dx.doi.org/10.1016/j.jcp.2008.08.027

[92] R. Langtry and F. Menter, "Transition modeling for general CFD applications in aeronautics," in *43rd AIAA Aerospace Sciences Meeting and Exhibit*. American Institute of Aeronautics and Astronautics, Jan. 2005. [Online]. Available: https://doi.org/10.2514/6.2005-522

[93] "Fluent – cfd online discussion forums — cfd-online.com," https://www.cfd-online.com/Forums/fluent/, [Accessed 21-10-2023].

[94] A. Katz and V. Sankaran, "Mesh quality effects on the accuracy of cfd solutions on unstructured meshes," *Journal of Computational Physics*, vol. 230, no. 20, p. 7670–7686, Aug. 2011. [Online]. Available: http://dx.doi.org/10.1016/j.jcp.2011.06.023

[95] J. C. S. Lai and M. F. Platzer, “Jet characteristics of a plunging airfoil,” *AIAA Journal*, vol. 37, no. 12, pp. 1529–1537, Dec. 1999. [Online]. Available: https://doi.org/10.2514/2.641

[96] H. Versteeg and W. Malalasekera, *An introduction to computational fluid dynamics*, 2nd ed. Philadelphia, PA: Prentice Hall, Feb. 2007.

[97] J. B. Barlow, A. Pope, J. J. Harper, and W. H. Rae, *Low-speed wind tunnel testing*, 3rd ed. Nashville, TN: John Wiley & Sons, Feb. 1999.

[98] K. Ghorbanian, M. R. Soltani, and M. D. Manshadi, “Experimental investigation on turbulence intensity reduction in subsonic wind tunnels,” *Aerospace Science and Technology*, vol. 15, no. 2, p. 137–147, Mar. 2011. [Online]. Available: http://dx.doi.org/10.1016/j.ast.2010.06.009

[99] J. C. Lerner and U. Boldes, *Wind Tunnels and Experimental Fluid Dynamics Research*. Rijeka: IntechOpen, Jul 2011. [Online]. Available: https://doi.org/10.5772/730

[100] L. J. Freeman, A. G. Ryan, J. L. K. Kensler, R. M. Dickinson, and G. G. Vining, “A tutorial on the planning of experiments,” *Quality Engineering*, vol. 25, no. 4, p. 315–332, Oct. 2013. [Online]. Available: http://dx.doi.org/10.1080/08982112.2013.817013

[101] R. J. Moffat, “Using uncertainty analysis in the planning of an experiment,” *Journal of Fluids Engineering*, vol. 107, no. 2, p. 173–178, Jun. 1985. [Online]. Available: http://dx.doi.org/10.1115/1.3242452

[102] C. F. Jeff Wu and M. S. Hamada, *Experiments*, 3rd ed., ser. Wiley Series in Probability and Statistics. Nashville, TN: John Wiley & Sons, May 2021.

[103] J. G. Bralla, *Design for Manufacturability Handbook*, 2nd ed. New York, NY: McGraw-Hill Professional, Aug. 1998.

[104] E. Mercker and J. Wiedemann, “On the correction of interference effects in open jet wind tunnels,” in *SAE Technical Paper Series*, ser. ANNUAL. SAE International, Feb. 1996. [Online]. Available: http://dx.doi.org/10.4271/960671

[105] E. Maskell, *A Theory of the Blockage Effects on Bluff Bodies and Stalled Wings in a Closed Wind Tunnel*, 1st ed. London: Her Majesty’s Stationary Office, Jan. 1963. [Online]. Available: https://reports.aerade.cranfield.ac.uk/bitstream/handle/1826.2/3982/arc-rm-3400.pdf?sequence=1&isAllowed=y

[106] A. T. Sayers and D. R. Ball, "Blockage corrections for rectangular flat plates mounted in an open jet wind tunnel," *Proceedings of the Institution of Mechanical Engineers, Part C: Journal of Mechanical Engineering Science*, vol. 197, no. 4, p. 259–263, Oct. 1983. [Online]. Available: http://dx.doi.org/10.1243/PIME_PROC_1983_197_107_02

[107] T. B. Owen, "Measured blockage effects on bluff bodies in closed and open wind tunnels." 1978. [Online]. Available: https://api.semanticscholar.org/CorpusID:109293952

[108] A. Hyvarinen, "Investigation of blockage correction methods forfull-scale wind tunnel testing of trucks," 2015. [Online]. Available: https://api.semanticscholar.org/CorpusID:49256753

[109] S. Smith, *Digital signal processing: A practical guide for engineers and scientists*. Elsevier, Oct. 2013.

[110] Y. Shi, *The Application of the Butterworth Low-Pass Digital Filter on Experimental Data Processing*. Springer New York, Nov. 2011, p. 225–230. [Online]. Available: http://dx.doi.org/10.1007/978-1-4419-8849-2_29

[111] J. H. Challis, *Signal Processing*. Springer International Publishing, Dec. 2020, p. 45–68. [Online]. Available: http://dx.doi.org/10.1007/978-3-030-52256-8_4

[112] R. B. Abernethy, R. P. Benedict, and R. B. Dowdell, "Asme measurement uncertainty," *Journal of Fluids Engineering*, vol. 107, no. 2, p. 161–164, Jun. 1985. [Online]. Available: http://dx.doi.org/10.1115/1.3242450

[113] E. P. Rood and D. P. Telionis, "Editorial," *Journal of Fluids Engineering*, vol. 113, no. 3, p. 313–314, Sep. 1991. [Online]. Available: http://dx.doi.org/10.1115/1.2909502

[114] R. A. Earnshaw and N. Wiseman, *An Introductory Guide to Scientific Visualization*. Springer Berlin Heidelberg, 1992. [Online]. Available: http://dx.doi.org/10.1007/978-3-642-58101-4

[115] R. Eymard, T. Gallouët, and R. Herbin, *Finite volume methods*. Elsevier, 2000, p. 713–1018. [Online]. Available: http://dx.doi.org/10.1016/S1570-8659(00)07005-8

[116] M. Bern and P. Plassmann, *Mesh Generation*. Elsevier, 2000, p. 291–332. [Online]. Available: http://dx.doi.org/10.1016/B978-044482537-7/50007-3

[117] W. R. Buell and B. A. Bush, “Mesh generation—a survey,” *Journal of Engineering for Industry*, vol. 95, no. 1, p. 332–338, Feb. 1973. [Online]. Available: http://dx.doi.org/10.1115/1.3438132

[118] B. E. Launder, G. J. Reece, and W. Rodi, “Progress in the development of a reynolds-stress turbulence closure,” *Journal of Fluid Mechanics*, vol. 68, no. 3, p. 537–566, Apr. 1975. [Online]. Available: http://dx.doi.org/10.1017/S0022112075001814

APPENDIX A

FRAMEWORK FOR EXPERIMENTAL INVESTIGATIONS USING LOW-SPEED SMALL/ MEDIUM WIND TUNNELS

A.1 Introduction

Experimental investigations using wind tunnel is an integral part of fluid mechanics. A Well planned and executed experiment is often considered the best method of investigation. Even with the intense increase in computational technologies, Fluid dynamics simulations still remain a close but approximate interpretation of the actual phenomena. Due to assumptions made during the development of the fluid dynamic solvers, mesh generators and result visualization tools, computational investigations remain as best option for occasions where experimental investigations are not viable due to financial or practical reasons [96]. However, due to financial limitations, most universities and research institutes may not have access to large and state of the art wind tunnel facilities. Most of technical universities in developing and under-developed countries only have small or medium scale wind tunnels. Open circuit and close circuit wind tunnels designs with a single test section are usually used in small and medium wind tunnels [97].

In this publication, it is attempted to provide a sufficient amount of information required to perform a successful experimental investigation using a small / medium wind tunnel. The primary motivation of this paper was the difficulties faced in attempting to carry out a research based on experimental investigations of pitching and plunging wings. During the research, it was realized that the information required to carry out a comprehensive experimental investigation in a small or medium scale wind tunnel has not yet been compiled into a single publication. Based on the information collected about the wind tunnel facilities available in other universities in the region, requirement for a such technical paper was established.

An experiment is defined as an operation or procedure carried out under controlled conditions in order to discover an unknown effect or law, to test or establish a hypothesis, or to illustrate a known law. In fluid mechanics, it's imperative to clearly define the objectives of the experiment. All the equipment and the methodologies used in the investigation are depended upon the objectives. Therefore, a detailed planning of the experimental process would ensure efficient management of resources.

A.2 Experimental Process

This compilation of information is primarily centered on wind tunnel tests specifically designed to measure steady-state or transient aerodynamic forces. These investigations represent the most prevalent type of aerodynamic studies, with testing requirements originating from industries such as aerospace, naval, and structural engineering.

A.2.1 Pre-test

A.2.1.1 Facilities and equipment

The most suitable approach for an experimental investigation depends on the available facilities and equipment. The objective is to achieve the most accurate measurements using the available resources. If the equipment is insufficient for the indented experimentation, the solution is to purchase or to design and develop a suitable solution. Because such new development of equipment would take both time and financial resources. The utilization of available facilities and equipment is always encouraged. The type and number of measuring equipment required for a wind tunnel test depend on the objectives of the investigation. Force, flow characteristics, velocity, pressure, temperature, and motion measurements are among the common intentions of a wind tunnel test.

The flow quality of the wind tunnel is paramount for a successful test. Quantification of the flow quality can be done by computing the turbulence intensity in the test section of the wind tunnel. The undesirable effects of turbulence in experimental wind tunnel investigations are documented in detail [98]. Turbulence intensity can be calculated using hot wire anemometer measurements [99]. Maintaining a turbulence intensity of 0.15% in the testing velocity range is expected in high fidelity experimental investigations.

A.2.1.2 Plaining of the experiment

With the knowledge of available resources in terms of facilities, measuring equipment, time and financial assets, the preliminary plan for the experimental investigation should be drafted. The experimental design should adhere to the scientific method and integrate expertise from both fluid mechanics and statistics [100–102]. The specifics of the plan would vary depending on the objectives of the investigation.

A.2.1.3 Design and development of experiment apparatus

In certain investigations, requirement of a new or unique experimental apparatus could become essential. Under such circumstances, design and development of an experimental apparatus would become an integral component of the "pre-test" procedure.

The specific aims and objectives of the investigation would determine the requirements of the apparatus which, in turn, define the complexity of the design. During the design phase, the principles of manufacturing design should be followed with an emphasis on the availability of sensors and actuators [103]. The design process of an apparatus would require knowledge of machine design and control system design. The experimental apparatus development process would be efficient when project management guidelines are followed.

A.2.1.4 Measuring equipment calibration

Prior to the test, all measuring equipment should be calibrated. Due to technical issues, equipment would vary from its initial state, declared in nameplates and user manuals. Calibration would enable to correct any bias error in the measuring equipment while providing a clear idea about the working condition of the instrument. Calibration processes for different measuring instruments would vary therefore, it is recommended to follow the manufacturer's instruction for calibration. In case of a non-measuring instrument used in a wind tunnel test, confirming the correct working condition is important for a seamless test phase of the investigation.

A.2.1.5 Uncertainity survey

Uncertainties are causes for errors in an experimental investigations. Although complete removal of uncertainties in a wind tunnel test is impossible due to technical limitations, steps must be taken to identify all uncertainties and remove the possible ones. The indelible uncertainties could then be quantified to the best extend and illustrated as part of the results. The whole process is named "Uncertainty analysis". The first step of uncertainty analysis is the survey to identify all uncertainties that may occur during the test. For this identification, experience in wind tunnel testing is vital. For novel investigators in wind tunnel testing, AGARD advisory report can be used a reference document [62].

A.2.1.6 Error sources specific to small and medium wind tunnels

Interference effects are a major contributor of errors in a small and medium wind tunnel test [104]. Given in Table A.1 is a list of common error sources in small and medium wind tunnels with methods of mitigation or corrections.

A.2.1.7 Development of models

In the case of small and medium wind tunnels, an experimental investigation would usually use a scaled model of an object. Due to space restrictions, the actual object under investigation is rarely used. When creating a scaled model, it is important to

TABLE A.1: Error sources in small/ medium wind tunnel tests and their mitigation/ correction methods

Error source	Description	Methods of mitigation/ correction
Solid blockage	The resultant effect from the increase in free stream velocity around the model due to the constriction of flow between the model and wind tunnel walls	Can be mitigated by keeping the blockage ratio under a certain value [105, 106], Correction method based on the model are available [97, 104, 107]
Wake blockage	Effect caused by viscous wake generated behind the model which constricts the effective tunnel cross section and leads to additional flow acceleration	Correction method based on the model are available [97, 108]
Streamline curvature	The effect caused as the tunnel walls straighten the normal curvature of the free air-flow around a model, Consequently, an airfoil in the tunnel exhibits increased lift and moment about its quarter chord at a given angle of attack	Corrrection for the angle of attack can be calculated [97]
Buoyancy	The variation in static pressure is attributed to the thickening of boundary layers along the wind tunnel walls	Correction for drag measurements can be calculated [97, 104]

achieve accuracy in dimensions and surface finish. When scaling an object, the standard method is to maintain the same Rein the scaled model investigation as the actual scenario. Therefore, it is crucial to achieve dimensional accuracy when replicating a specific instance in a wind tunnel test.

Rapid prototyping techniques such as 3D printing and routing are favored in scaled model development. These manufacturing methods provide good dimensional accuracy with minimal lead time and material wastage. The accuracy of the dimensions should be confirmed before testing and uncertainty of the measurements should be included in the uncertainty analysis.

Surface roughness of a model should be regulated due to its significant impact on aerodynamic performance [61]. In the absence of a specific requirement for increased surface roughness, the standard for wind tunnel test model as stated in AGARD advisory report should be followed [62].

A.2.1.8 Scheduling of the tests

Results of a single experimental investigation can be affected by bias and random error sources even after taking all the precautionary measurements mentioned in "pre-test" section. Therefore, it is not recommended to depend on a single measurement for the final results. Average of multiple measurements would mitigate bias errors from propagating into the final results while providing standard deviation values for further analysis. Multiple measurements are also usefull in uncertainty analysis which would determine the confidence of the results which are essential in a experimental investigation. Scheduling of these multiple tests in an effective order could resources including time and manpower.

A.2.2 Test

"The "test" stage of an investigation encompasses all tasks that should be completed during the time period of testing. The preparation of the "pre-test" phase should be effectively adopted in the "test" phase.

A.2.2.1 Model and instrument positioning

The calibration of the instrument and the development of the model are capitalized only if they are positioned and handled properly using the test phase. Measuring instruments should be stably mounted in designated locations with minimal interference to the air flow. Both in static and dynamic model wind tunnel test, the positioning and securing of the model is of critical importance. The model which is scaled to minimize solid and wake blockage should be positioned accordingly. The flow induced vibration can cause undesirable effected on measurements obtained using an unstable model, therefore the mechanical connection between the model and force sensors or other measuring instrument should be carefully analyzed.

A.2.2.2 Test execution

Following the test schedule during the test is important in this most critical step of the investigation. Decisive measurements such as the wind velocity and angle of attack of the model should be double checked in every iteration of the test. The vibration level of the model and the model fixture or apparatus must be monitored.

A.2.2.3 Measuring modeling environmental data

In addition to the primary measurements of an investigation like force, moment measurements, or flow visualization images, measurements of the test environment should be taken. Such data provide an essential background for the investigation and are vital in ensuring the validity of the test. The measurements should include vibration level of the model, air temperature, air humidity, test elevation and atmospheric pressure.

A.2.2.4 Measurement documentation

Proper documentation of the measurements is the most critical step of the investigation. Measurement files for each iteration of the test should be named following a structure which will help to identify files later. Backup files should be made and stored in a secure data storage for emergency use.

A.2.3 Post-test

The post-test phase of the investigation would convert the measurements taken into usable results which could be analyzed.

A.2.3.1 Measurement processing and data reduction

The measurements taken using force or moment sensors or anemometers contain perturbations caused by vibration of the model and sensor, electronic distortion of the circuits and wires. Sensors and gauges for temperature and pressure measurements also register fluctuations in their readings. They are common in steady state and transient measurements taken for a time duration. The ramifications of these perturbations could hide the true trends in the results and could bring unnecessary complications to the results calculation process. The common solution for this issue is filtering the measurements using numerical methods. Popular among the previous wind tunnel investigations are three filters named moving average, Butterworth, and Chebyshev filters.

Despite it's simplicity, the moving average filter is used to reduce random noise while retaining a sharp step response. The number of elements used for averaging is optimized through comparative analysis of multiple results [109]

The low-pass Butterworth filter is used to attenuate the data with a frequency higher than the cutoff frequency value [110]. The cutoff frequency is defined through the Normalized frequency equation as given in Eq 1. [111]

$$f_n = \frac{f_C}{0.5 * SR} \tag{A.1}$$

The low-pass Chebyshev filter is used for further improvement of the smoothness of the data variation. The four parameters needed to fully define the Chebyshev filter are low pass response, the cutoff frequency, the percent ripple in the passband, and the number of poles [109]. Refinement of filter parameters is important to retain the characteristics of the results while reducing noise.

A.2.3.2 Uncertainty analysis

Due to technical limitations uncertainties in a wind tunnel investigation can not be completely removed, therefore an uncertainty analysis should be carried out to calculate the confidence range of the final results. Each and every uncertainty contributor to the final calculated result should be considered, and their fractional uncertainty should be propagated through the data reduction equations to the final percentile uncertainty value. The 95% confidence large sample uncertainty assessment approach is commonly followed in wind tunnel investigations as recommended by ASME [112, 113]. The standard methodology is defined by AGARD advisory committee [62].

A.2.3.3 Results visualization and presentation

All steps of the investigation lead up to obtaining accurate and detailed results. However, the effort of the investigation would only materialize when the results obtained are presented in a clear and comprehensive manner. Data visualization techniques for scientific publications have been optimized for different data types [114].

A.2.3.4 Sustainability of the experiment

In the case of an experimental aerodynamic investigation, the ability to recreate the investigation and to iterate the investigation with different parameters is important. Specific steps of the investigation, challengers faced and their solutions should be documented in detail. For custom-developed experimental apparatus, creating a comprehensive user manual with instructions for maintenance and upgrades is essential to facilitate seamless knowledge transfer.

The framework for experimental aerodynamic investigations using small/ medium low-speed wind tunnels is summarized in Fig. A.1.

Fig. A.1: Summarized Visualization of the Framework

APPENDIX B

GUIDELINES FOR COMPUTATIONAL FLUID DYNAMICS INVESTIGATIONS OF MOVING OBJECTS USING ANSYS FLUENT

B.1 Introduction

Computational Fluid Dynamic (CFD) simulations of aerodynamics of moving objects are inherently complex and challenging due to being transient with changing boundary conditions. Although a commercial CFD tool like Ansys Fluent provide user friendly interfaces and user guides to reduce the complexities of the simulation procedure. Features such as User Defined Functions (UDF) and dynamic mesh generation require specialized knowledge, which may pose challenges for new users unfamiliar with these concepts. This discussion emphasizes CFD simulations utilizing the Finite Volume Method (FVM) and Reynolds-Averaged Navier-Stokes (RANS) solvers. The Finite Volume Method (FVM) is a discretization technique well-suited for various numerical simulation approaches, particularly in Computational Fluid Dynamics (CFD), owing to its applicability to the Eulerian approach in fluid mechanics [115]. For engineering applications, CFD users generally seek information about time-averaged flow properties, such as mean velocities, pressures, and stresses. Hence, turbulent flow computations primarily rely on procedures based on the Reynolds-averaged Navier-Stokes (RANS) equations [76]. This document serves as a comprehensive guide for novice researchers interested in computational investigations involving aerodynamics of moving objects Additionally, a step-by-step guide is included to assist investigators in generating simulation results suitable for publication, which encompasses more steps than a typical simulation procedure for industrial applications.

B.2 Investigation methodology

B.2.1 Geometry selection and defining the domain

Geometry development should be undertaken following a meticulous analysis of the investigation's objectives, alongside a comprehensive understanding of the limitations associated with mesh generation. Here, "geometry" refers to the models of the objects under investigation in the CFD analysis. Simplification of the geometry should be entertained with caution to improve the computational efficiency of the simulation without compromising the accuracy. The Ansys software package enables users to import geometry created using third-party Computer-Aided Design (CAD) tools, as well as create geometry using CAD tools available within the software suite. Dimensional accuracy of the geometry is paramount, for both scaled or non-scaled geometries, as even minor discrepancies can greatly influence simulation results. Thus, meticulous attention to detail during geometry creation is essential to ensure accuracy and reliability in the analysis.

Domain in CFD simulations is defined the volume of fluid simulated to understand the fluid mechanics of model geometry. Typically, this involves creating a cuboid-shaped domain that encompasses the model, providing sufficient space for the development of wake and pressure variations without any obstructions.

B.2.2 Kinematic calculation

In the case of simulation with motion of a model or a boundary, the velocity profile of the moving part should be calculated. In case of a series of simulations with varying kinamtics, use of a code for calculating the kinematic parameters is advised to keep the accuracy consistent. The kinamtic parameters required for different type of simulations are usually defined by the UDF used.

B.2.3 Mesh generation

Mesh generation is the discretization of the fluid domain into section to carry out finite volume method calculations. The most common shapes are triangles and quadrilaterals in two-dimension and tetrahedra and hexahedra in three-dimension [116]. A user can develop various different meshes using the tools available in “Ansys Mesh” application. However, characteristics of the mesh should be defined by the objective of the investigation and the dimensions of the domain for a successful simulation [117].

B.2.4 Turbulence model selection

Selection of the suitable turbulence model for the particular simulation is a critical step in the investigation. For this understanding about the theoretical development of turbulent models are essential [96]. The interpretation of turbulence in RANS solvers allows for different turbulence models

B.2.5 User Defined Functions

User Defined Functions (UDFs) control specific parameters in the simulation based on functions defined by the user. Through this main functionally, UDF are used in various scenarios including rigid body motion in dynamic mesh modelling which is the focus of this discussion [75]. The CFD simulation process in Ansys Fluent is depicted in Figure B.1, highlighting the involvement of UDFs to assist investigators to understand the point of interference of different UDF types.

TABLE B.1: Turbulence model available for RANS solvers in Ansys fluent

Turbulence model	Description	Suitable applications
Spalart-Allmaras	one-equation turbulence model for kinematic eddy turbulent viscosity	Offers robustness and efficiency in simulating attached and moderately separated flows, Initially developed low Reflow and suits aerodynamic applications, Not suitable for general industrial flows. [81]
k-ϵ	one of the simplest and most widely used RANS turbulence models. It assumes isotropic turbulence and employs two transport equations: one for turbulent kinetic energy (k) and the other for its dissipation rate (ϵ)	Developed specifically for planar shear layers and recirculating flow, performs well for a wide range of turbulent flows but may struggle in complex flow situations. [82]
k-ω	Offers corrections for low Reynolds number and shear flows, accounts for viscous heating, and requires minimal memory resources. Use two partially differential equations to solve for turbulence kinetic energy (k) and specific rate of dissipation (ω)	Accurate for attached boundary layers, backward-facing steps, and mildly separated incompressible flows. [83, 84]
Transition k-kl-ω	Modified k-ω turbulent model with addition of another equation solving for kL, where L is an integral length scale of turbulence and k is the turbulent kinetic energy	Provides qualitatively correct transition behavior for a wide range of flow conditions including freestream turbulence, pressure gradient, and surface curvature on the turbulence development.[78, 85]
Transition Shear Stress Transport (SST)	Combines the benefits of the k-ω and k-ϵ models. It uses the k-ω model near the wall to resolve the boundary layer accurately and the k-ϵ model away from the wall to handle adverse pressure gradient flows	Provide significant improvement for all flows involving adverse pressure gradients and suitable for wide range of aerodynamic applications, Accurately predict pressure-induced separation and the resulting viscous-inviscid interaction. [77, 86, 87]

Reynolds Stress Transport (RST)	A higher-order RANS turbulence model that solves additional transport equations for the Reynolds stresses and considered to be the most complete classical turbulence model	Offers better accuracy in capturing anisotropic turbulence effects but at a significantly higher computational cost. [118]
Detached Eddy Simulation (DES)	A hybrid modeling approach that combines RANS and LES methods. It applies the RANS model in regions where the flow is predominantly attached to surfaces and switches to LES in separated or unsteady regions, Offers a good compromise between computational cost and accuracy	Specifically designed to address high Reynolds number wall bounded flows but suitable for majority of flow scenarios

B.2.6 Pilot simulation

The objective of the pilot simulation is to establish a base for the forthcoming investigation. The most complex scenario within a predefined range of investigation should be chosen as the pilot simulation. This can be advantageous when applying the optimized approach to other scenarios. In an investigation exploring the fluid mechanics of a moving object, it is advisable to choose a scenario with the most intricate and complex kinematic parameters. The pilot simulation should be developed to a stage where it is free of errors. Please refer to the "Common Errors and Solutions" section for guidance on resolving any issues.

B.2.7 Mesh and time step convergence analysis

Although the mesh developed in the pilot simulation is sufficient to complete the simulation without any errors, it is not yet optimized for accuracy or computational efficiency. The same can be said for time step values in transient simulations. The mesh and time step convergence analysis is the widely used method for optimization. Two mesh arrangements should be created, using the successful mesh from the pilot simulation as a baseline. One mesh should be less refined, while the other should be more refined in terms of mesh resolution. The results and computational cost in terms of processor hours should be taken into account when selecting the optimal choice from the three. If the selected mesh is newly developed, the process should be iterated with another mesh further along the same trend until a satisfactory mesh arrangement is achieved. The same method should be applied for the time step optimization.

B.2.8 Validation

Validation is an essential step in CFD investigations, particularly in academic research. In a computational investigation, the validity of all steps, including mesh and time step optimization and turbulence model selection, is ensured through comparative validation of the simulation results. When feasible, comparison with experimental measurements of the same or similar scenario is preferred over comparing with other computational results.

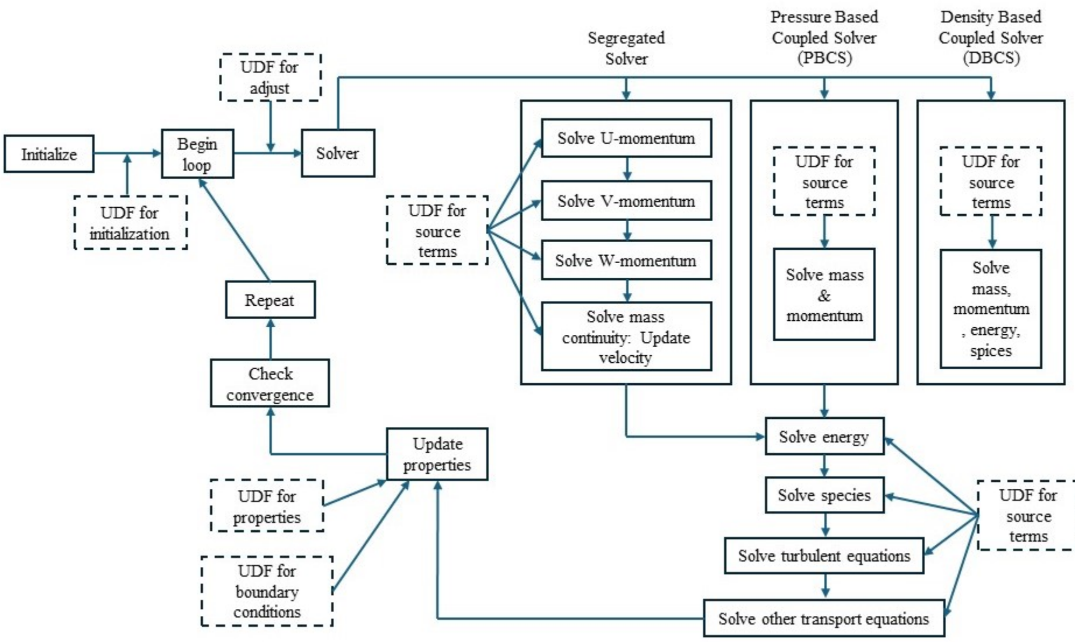

Fig. B.1: Process of a CFD simulation in Ansys fluent with UDF interference indicated

B.2.9 Investigative simulations

After developing, optimizing, and validating the simulation setup, a series of simulations can be conducted to achieve results that fulfill the original objectives of the investigation. During simulations, it's essential to save result files at regular intervals. Numerical results such as force, velocity, or pressure should be updated and written into files at each time step of a transient simulation. Data exports for generating vector plots or contour developments should be conducted only at regular intervals of several time steps, as they can consume a significant amount of drive space for storage.

B.2.10 Data analysis

The numerical results, such as drag, lift force variation, and pressure and velocity values at probe points, are typically further analyzed to generate the final results of an investigation. Steady state result values are usually subjected to data reduction equations to calculate non-dimentional coefficient for comparison purposes. However, transient force, pressure, velocity time-history variations usually demand filtering for noise reduction and smoothing before being subjected to data reduction equations. Commonly used large sample data filters for this purpose are moving average and 2^{nd} order Butterworth filter filters. Although simple in design, the moving average filter effectively diminishes random noise while preserving a clear step response. The optimal number of elements for averaging is determined through comparative analysis of multiple outcomes [109]. The low-pass Butterworth filter is used to attenuate the data with a frequency higher than the cutoff frequency value [110, 111].

B.2.11 Image and animation rendering

The exports from the simulation enable the creation of images and animations of vector and contour plots. Ansys result visualization tool is well equipped to develop render vector and contour plots visualizing various different results parameters including the most commonly used velocity, pressure, vorticity, turbulence intensity [75]. When generating animations from rendered images, it's crucial to carefully consider the frame rate of the video. Mismatched frame rates can create the perception that the flow or objects in the video are moving at different speeds. To avoid this, the simulation time of the time steps should be synchronized with real time using a third-party video editing tool. Moreover, consistency in contour rendering with the scaleplot across multiple images can be achieved by manually defining the maximum and minimum values of the scaleplot. This can be beneficial for comparative analysis of contour rendering in various scenarios.

B.3 Common errors and solutions

B.3.1 Divergency errors

TABLE B.2: Causes and solutions of divergence errors in Ansys fluent

Reason	Description	Solution
Poor mesh quality	Low-quality meshes with skewed or distorted elements can lead to convergence issues and divergence errors	Improve mesh quality by identifying the low quality zones of the mesh using Ansys mesh analytics tool.
Incorrect boundary conditions	Inaccurate or improperly specified boundary conditions can disrupt the flow physics and cause divergence	Careful consideration of boundary conditions and re-checks of the setting and numerical inputs prior to calculation
Inadequate numerical settings	Improper selection of numerical schemes, solution methods, or convergence criteria can hinder convergence and lead to divergence	When selecting numerical method settings, thorough understanding is essential as each setting, though simplified for user-friendliness, significantly impacts the solver. Conduct research on each option to ensure its suitability for the simulation.
Complex flow physics	Highly turbulent or multiphase flows, combustion, or other complex phenomena	Require specialized modeling techniques and careful setup to avoid divergence, Optmized pilot simulation is an essential component in such situations
Unsteady flows	Transient simulations with rapidly changing flow conditions	require smaller time steps or additional stabilization techniques to maintain convergence. When periodic motion is present using a fraction of the periodic time would assist in the optimization. Purpose build mesh is essential.
Mesh motion or deformation	Simulations involving moving or deforming meshes	Require careful consideration of mesh quality and stability to prevent divergence

B.3.2 Mesh stiffness errors

Mesh stiffness error is a common occurrence when "Dynamic Mesh" option is used in Ansys fluent. Dynamic mesh facilitates fluid domain changes due to model or boundary motion. The software rearranges the mesh geometry at each time step to accommodate these domain geometry changes during simulation. However, due to limitations, a specific mesh arrangement has an upper limit on how much a geometric feature can change within a time step. When this limit is exceeded, mesh stiffness errors occur. It's worth noting that structured mesh arrangements may not adapt well to such geometric rearrangements. An unstructured mesh, which gradually reduces refinement level when moving outward from the target geometry, is often recommended as the most suitable option. To resolve this error, optimization of both the time step and mesh arrangement is necessary. One solution is to reduce the maximum size of mesh elements closest to the moving geometry to be smaller than the distance the geometry moves in a single time step.

B.3.3 UDF compilation error

UDF compilation error is encountered when attempting to compile and imported UDF file with ".c" extension. The underlining cause to this error in most cases is technical or licensing issues related to the Ansys software license. When faced with such issue, the following solution can be recommended as a solution. The following code with changes to the "Microsoft Visual Studio" version and saved as a "Windoes Batch File" should be placed in the administrative folder of the computer and should be opened to create the fluent file of the simulation. Via the link created between "Microsoft Visual Studio" and "Ansys fluent" by the code, the issue would be resolved allowing for the compilation of the UDF file.

```
\2022\Community\VC\Auxiliary\Build\
set vs=vcvars64.bat

cd %workingDir%
call %vs%

:: input file location of "fluent.exe" here
call "C:\Program Files\ANSYS Inc\v181\fluent\ntbin\win64
\fluent.exe"
```

APPENDIX C

USER MANUAL FOR THE EXPERIMENTAL APPARATUS

C.1 Introduction

The primary objective of the design and development of the experimental apparatus is to measure the aerodynamic forces of a pitching and plunging airfoil. However, the capabilities of the apparatus is not limited to the primary objective. One of the aims of the development is to provide a well-built experimental setup for future aerodynamics investigations at the university, which can take various forms. This user manual document is written to ensure continuous use and maintenance of the apparatus and to enable future upgrades and development.

The user manual consists of four sub-sections. In the system description sub-section, all major components are discussed in detail. Three-dimensional models of the components are stored in cloud storage for future use. In the user instruction sub-section, a step-by-step guide is provided to perform major tasks concerning the apparatus and experimental investigations. Instructions for maintenance of the apparatus including all electronic components are provided in the maintenance instruction sub-section. In the final sub-section, suggestions for future designs for upgrades and alterations that would increase the uses of the apparatus even further are given.

C.2 System description

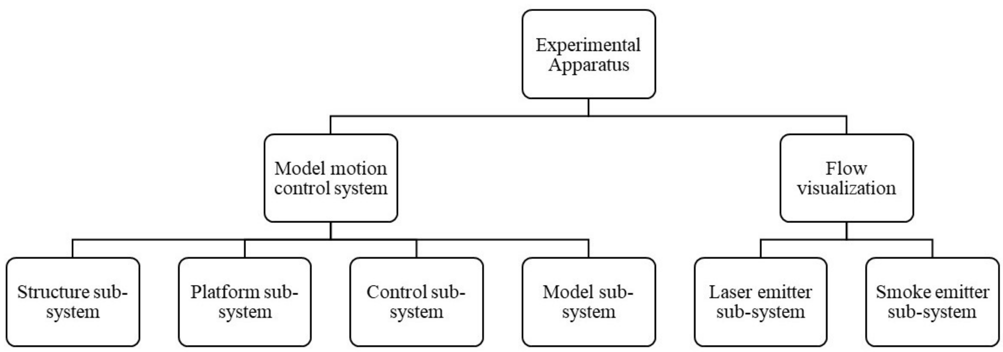

Fig. C.1: Sub-systems of the experimental apparatus

The experimental apparatus is designed and developed in sub-assemblies which are described in this section as sub-systems to provide a novel user with some familiarization of the apparatus.

C.2.1 Support structure sub-system

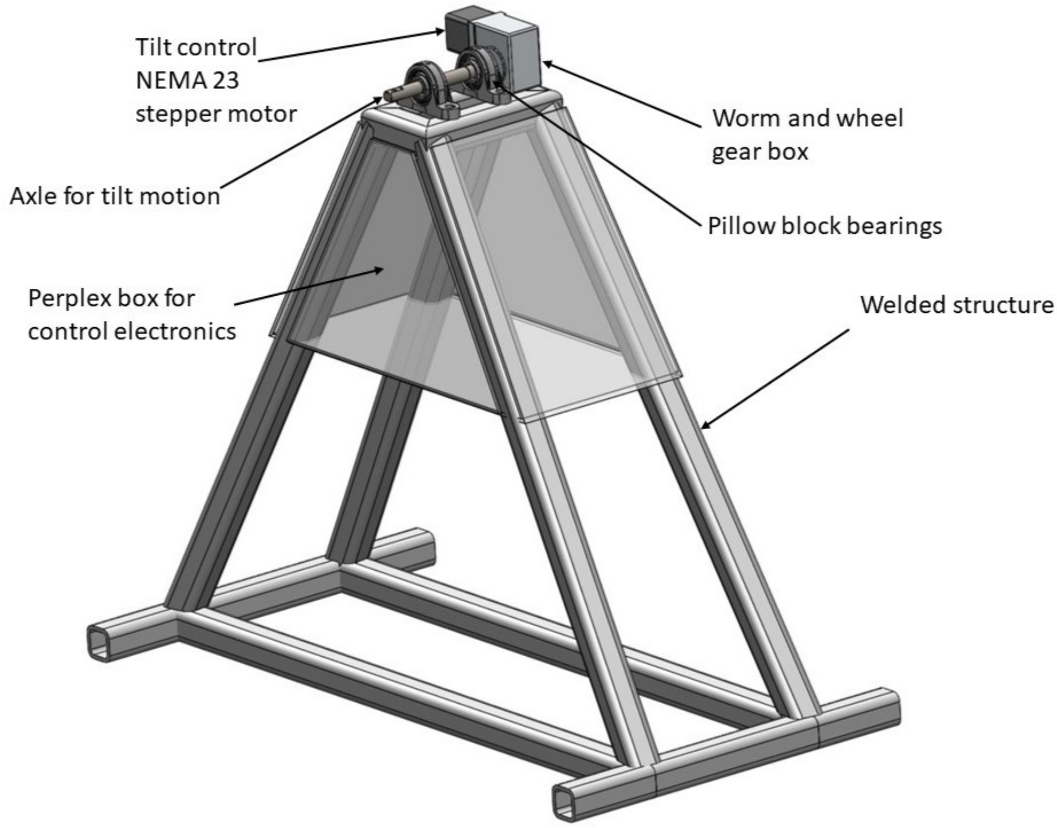

Fig. C.2: 3D model of the support structure sub-system

The primary function of the support structure is to provide stability for all other components. Its wide base design ensures stable allocation of the cantilevered platform structure, with the center of gravity within the base dimensions to reduce the risk of toppling. Six adjustable leveling legs allow to maintain a perfect horizontal wing in any given floor. As shown in Fig. C.2, the stepper motor and the gear mechanism used for tilting are considered as components of this sub-system. Two pillow block bearings hold the tilt axle in place while enabling tilting of the platform sub-systme with the assistance of the stepper motor driven gear mechanism. The tilting allow for change the plunge axis angle proving an addition degree of freedom the the motion control system. Additionally, the acrylic plastic box serves to create a dust-free environment for the control electronics.

C.2.2 Platform sub-system

The main objective of the platform sub-system is to facilitate the motion of the wing. The structural components of the platform are 20x20 aluminum extruded bars and 5mm aluminum panels. The pitching motion of the wing is facilitated by a single NEMA

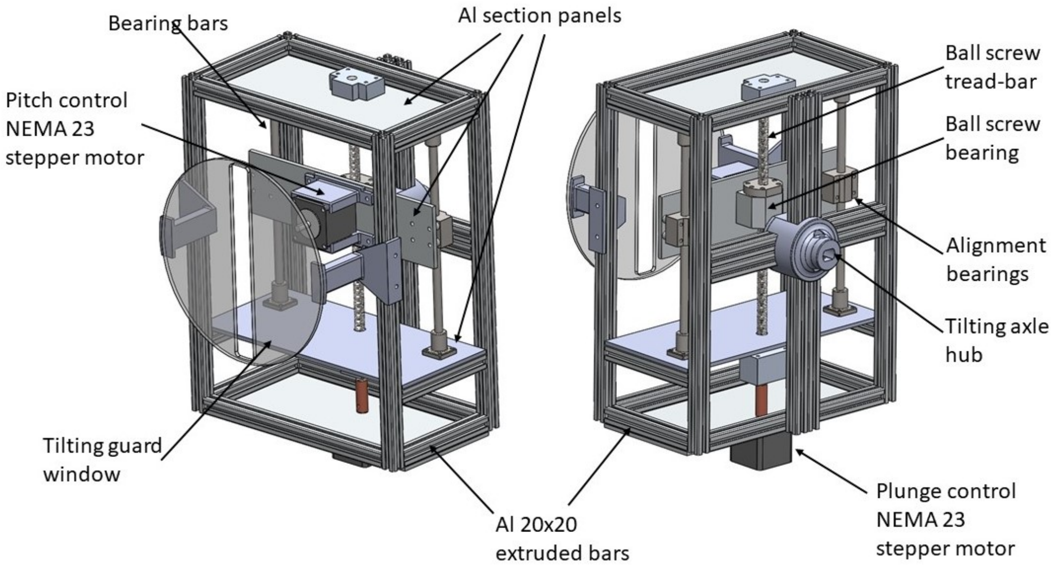

Fig. C.3: 3D model of the platform structure sub-system

23 stepper motor connected to a vertical aluminum plate. This plate is supported by a ball screw bearing, enabling vertical movement of the plate and the connected motor. The motion is controlled by the NEMA 23 motor located at the bottom of the structure. The rotational motion of the motor is converted into translational motion of the plate by the ball screw and its bearing. Two bearing bars equipped with linear bearings offer additional alignment support for the plunging structure, effectively eliminating any torsion. Additionally, the tilt guard window is specifically designed to contain the wind tunnel flow within its intended boundaries, serving as a wall boundary while allowing the platform to tilt. The hub is connected to bracing 40x20 aluminum extruded bars. Using the hub as the connector the whole platform sub-system is suspended in cantilever fashion by the tilt axle of the structure.

Efforts were made to enhance the structural rigidity and minimize vibrations in the platform. Structural rigidity is critical for minimizing distortion in the platform structure when forces are transmitted through it. Any distortion could compromise the accuracy of wing motion. Minimizing vibration in the platform structure, induced by wing motion, is crucial for maintaining minimal random errors in load cell measurements. To achieve this, all mechanical fasteners were securely fixed using resin-based glue.

C.2.3 Control sub-system

The control sub-system manages the power and information for all the actuators and sensors in the experimental set-up including the laser emitter. Only the smoke generator is powered separately. The main control unit is a “Raspberry Pi 3 Model B+”

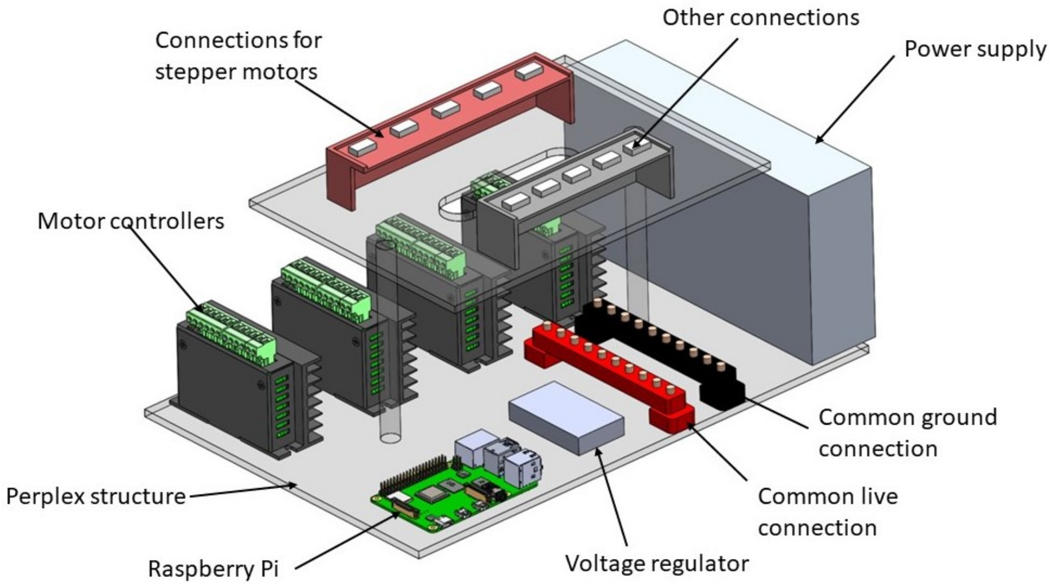

Fig. C.4: 3D model of the control sub-system design

computer which can be wirelessly connected to a laptop to manage input and output data in real time. Four TB6600 motor controllers are available to control the 3 motors, the additional one can be used in case of a emergency of in any future improvements. 24V power supply provide regulated voltage to the sub-system, the voltage regular is used to step down voltage to 5V for any required electronics. The whole sub-system is designed to be modular and repair-friendly. If any component becomes faulty, it can be replaced by only disconnecting two points in the circuit. The dedicated panels to the connections allow the entire control sub-system to be removed form the plexiglass enclosure in case of a modification or maintenance issue.

For the wireless connection between the Raspberry Pi and the laptop, PuTTY and VNC viewer software are used. To establish the WiFi connection between the two computers a WiFi hotspot is created by a separate device. A computer, a mobile phone or a WiFi router can be used for the task.

C.2.4 Flow visualization system

The flow visualization system comprises laser and smoke emitter sub-systems. The smoke emitter rake is positioned inside the wind tunnel before the test section, with its accompanying equipment connected while remaining outside the wind tunnel. The laser emitter sub-system should be positioned near the outlet of the wind tunnel with the laser plane aligned to the verticle plane of the smoke emitter rake. The laser interacts with the smoke particles to visualize the flow behavior under investigation without impeding the flow mechanics. The best visualization is achieved when using a laser

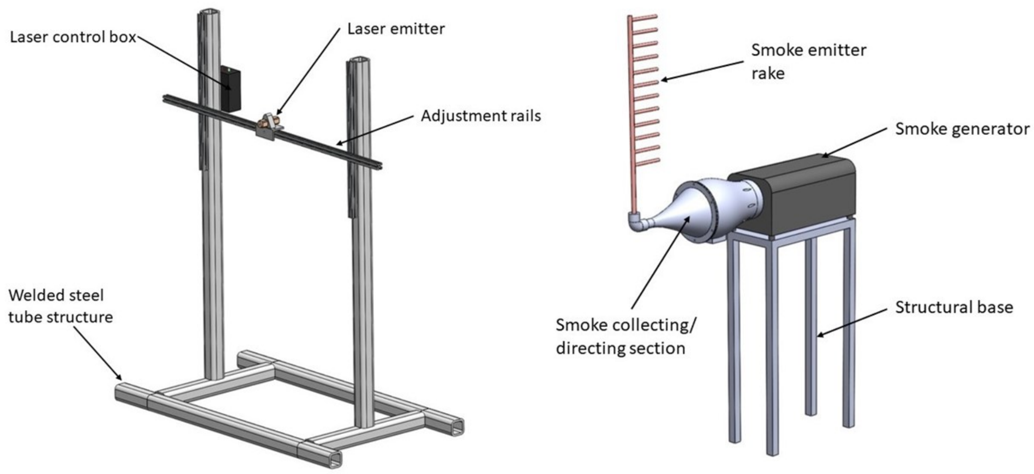

Fig. C.5: 3D model of flow visualization system

emitter with 532nm wavelength (green laser). The laser is positioned on rails that are adjustable in vertical and horizontal directions.

C.3 User instructions

C.3.0.1 Preparation of the set-up for an experiment

- The model motion control system needs to be positioned correctly as the first step of the preparation. The position of the model inside the wind tunnel relative to the two walls should be determined by the objectives of the investigation.

- The power supplying electrical connections for the "Raspberry-Pi", force sensor amplifier, stepper motors and the auxiliary power supply should be securely connected.

- Then the wifi connection between the user's personal computer and the "Raspberry-Pi" should be established. For this, a personal wifi network should be established using a wifi router or a similar device (mobile phone) with both the "Raspberry-Pi" and the personal computer configured to be connected that wifi network.

- With the wifi connection established, "PuTTY" configuration software tool should be used to establish the link between the personal computer and "Raspberry-Pi" by entering the IP address of the personal wifi network.

- Using "VNC Viewer" software tool or a simular tool, "Raspberry-Pi" can be controlled as the user. New codes can be developed and tested to operate all the actuators and sensors connected to the model motion control system using "Python" programming language.

C.3.1 Motion control of the model

- With the controlling connection established between the user's personal computer and the "Raspberry-Pi" of the apparatus, the motion of the model can be controlled via custom-developed "Python" codes.
- For the ease of repetition of a motion profile of the model. the motors should be brought to "home" position as selected by the user to suit the specific testing scenario.
- an example code for the "Raspberry-Pi" that was used to control a single selected motor is attached below for reference.

```python
from time import sleep
import RPi.GPIO as GPIO

#GPIO pins for the motors
M1_SP = 21
M1_DP = 20
M2_SP = 26
M2_DP = 16
M3_SP = 19
M3_DP = 13
M4_SP = 12
M4_DP = 6

AC = 16.3 #Angle Change needed
D = 1 #Direction of the rotation CW=0 or CWW=1
SP = M3_SP  #Stepper pin of the intended motor
DP = M3_DP  #Direction pin of the intended motor

GPIO.setmode(GPIO.BCM)
GPIO.setup(SP, GPIO.OUT)
GPIO.setup(DP, GPIO.OUT)

c2 = int((AC/360)*200*32)
delay = 0.005

for n in range(c2):
    GPIO.output(DP,D)
    GPIO.output(SP, GPIO.HIGH)
    sleep(delay)
    GPIO.output(SP, GPIO.LOW)
    sleep(delay)
```

C.3.2 Measurement file management

- The raw output measurements of the force sensor is a voltage value in millivolts which can be converted to Newton using a conversion equation developed via calibration.
- The voltage values can be read and saved into a file type of choice using the following code.
- The frequency of measurement taking and the time period of measuring or number of measurements can also be varied by the user.
- The saved files can then be subjected to post processing to calculate the required results.

```
from multiprocessing import Process
from threading import Thread
import time
from time import sleep
import RPi.GPIO as GPIO
import numpy as np
import math
import sys
import pandas as pd
import smbus
import sys
import trace
import threading


address = 0x48 #address of the i2c bus
A0 = 0x40 #address of the first analog input pin
bus = smbus.SMBus(1)


#Modifying Tread function to enable returning values
class CustomThread(Thread):
    def __init__(self, group=None, target=None, name=None,
                 args=(), kwargs={}, Verbose=None):
        Thread.__init__(self, group, target, name, args, kwargs)
        self._return = None

```

```
    def run(self):
        if self._target is not None:
            self._return = self._target(*self._args, **self._kwargs

    def join(self, *args):
        Thread.join(self, *args)
        return self._return

def count():
    c = 50;
    for n in range(c):
        sleep(2)
        n=n+1
        if n ==c:
            break


def loopMeasure():
    ValSeq = []
    while(p1.is_alive()):
        bus.write_byte(address,A0)
        value=bus.read_byte(address)
        print(value)
        ValSeq.append(value)
        time.sleep(0.001)
    return ValSeq

p1 = CustomThread(target = count,)
p2 = CustomThread(target = loopMeasure,)

p1.start()
p2.start()

Results=p2.join()

#Write the value array into a CSV file
df = pd.DataFrame(Results)
df.to_csv('File_name', index=False)
print(Results)
print('End of measurements')
```

C.4 Maintanance instructions

C.4.1 Day to day maintenance

- The apparatus should be kept clean of dust, cobwebs and other similar foreign material. If unable to keep the apparatus in a clean environment, it should be covered when unused for long periods of time. Prior to use the apparatus should be checked for cleanliness.

- The ball screw and other bearing of the apparatus should be oiled (No grease should be applied) regularly to keep them in good working order.

- The force sensor arrangement should be separated from the pitch control motor when storing for long periods of time. The force sensor should be kept stored in a separate clean storage.

- The power supplying electrical connections should be detached and stored securely after each use.

C.4.2 Major component refurbishment or replacement

- In case of a major component refurbishment, replacement or alterations, the 3D models of the existing components can be accessed via the supplied Link using a University of Moratuwa institute email.

- The drive folder also contains a set of documents with further details on the apparatus and a library of "Python" codes to be used in various situations.

- Disassembly of any components should be done after securely disassembling the relevant sub-assembly as mentioned above the system description section.

- For additional assistance, the original developer of the apparatus can be contacted via "lakshitha.official@gmail.com" email address.

Fig. C.6: QR code of the drive folder containing additional information about the experimental apparatus design

C.5 Suggestions for future development

- The flow visualization system requires further improvement. While all major components for development are currently available, the system development remains incomplete. Attention should be devoted to advancing the flow visualization system to a stage where it can be regularly utilized in graduate and undergraduate research, as well as demonstration work.

- The pitch control stepper motor can be replaced with an assembly of two stepper motors capable of controlling both pitch and heave motion of a model. While an assembly with similar performance was developed, the gear mechanism connecting the two motors and the model was found unsuitable due to an unacceptable level of backlash between gears. A new gear mechanism should be developed to enable the use of heave motion control.